Dissertation zur Erlangung des Doktorgrades
der Fakultät für Chemie und Pharmazie
der Ludwig-Maximilians-Universität München

A Larval Zebrafish Xenograft Model: Evaluation of Leukemia-Niche Interactions and Its Potential to Predict Relapsing Leukemia

Anja Arner

aus Memmingen, Deutschland

2021

Erklärung

Diese Dissertation wurde im Sinne von §7 der Promotionsordnung vom 28. November 2011 von Frau Prof. Dr. Angelika M. Vollmar betreut.

Eidesstattliche Versicherung

Diese Dissertation wurde eigenhändig und ohne unerlaubte Hilfe erarbeitet.

München, den 24.11.2021

(Anja Arner)

Dissertation eingereicht am:	13.09.2021
1. Gutachterin:	Prof. Dr. Angelika M. Vollmar
2. Gutachterin:	Prof. Dr. Irmela Jeremias
Mündliche Prüfung am:	25.10.2021

Meinen Eltern

CONTENTS

ABSTRACT

Acute lymphoblastic leukemia (ALL) is the most common malignancy during childhood. Even though the prognosis after initial diagnosis is good, patients suffering from relapse have a poor outcome. To date, most studies investigate leukemia cells (LCs) independent from their surrounding tissue. Model systems that consider the microenvironment are rare and little is known about niche-mediated mechanisms that are involved in relapse development. The tumor microenvironment is more and more recognized as an important component during the emergence of relapse. In the present work, an innovative larval zebrafish xenotransplantation model was established that allowed the analysis of LCs within an orthotopic niche. This model was applied to identify characteristics of LCs with high relapse potential in their specific niche interaction.

In a first step, the xenotransplantation process of human LCs was robustly established. As demonstrated using microscopic and flow cytometric approaches, LCs homed, engrafted and proliferated within the expected niche site, the caudal hematopoietic tissue (CHT). In a second step, the interplay of LCs with niche macrophages and endothelial cells was characterized. Here, close and persisting interactions of LCs with macrophages were monitored, while only few phagocytosis events and low macrophage infiltration rates were detected. In addition, a specific dissemination pattern of LCs within the CHT was observed, as LCs extravasated and formed clusters, in close contact to endothelial cells. In conclusion, a novel zebrafish model was generated that enabled the analysis of LCs in a functional and complex microenvironment.

I hypothesized that LCs that caused an early relapse, exploit the niche more efficiently than other LCs. To test this hypothesis, the novel xenograft model was used to analyze the migration behavior of different LCs *in vivo*. Cells of eleven primary pediatric B-cell precursor ALL samples were transplanted and analyzed subsequently, five patients with early (ER) and six with no relapse (NR). Importantly, treatment naive cells originated from the initial diagnosis. Thus, cellular features that were already present at time of diagnosis could be identified. Applying time lapse confocal microscopy, migration parameters of the LCs were examined as a measurement for niche utilization, as more locally residing or anchored cells were considered to interact more efficient with surrounding niche cells. A robust, sensitive, semi-automated and unbiased workflow to track LCs was established. For comparative analysis of ER- and NR-samples, different migration parameters were analyzed. It became apparent that within the niche, ER-cells migrated slower, resided in a reduced area and were more anchored, indicating more interaction with certain niche cells. A score was established, which ranked the behavior for all eleven individual patients. Interestingly, four out of five ER-patients received a very high anchoring score. This pilot study suggests the relapse-prognostic potential of this short-term assay in a clinically applicable timely manner of only two days.

Ultimately, cells with considerable differences in motility were transcriptionally analyzed and gave new insights into the biology of these cells that later developed a relapse, as they showed a distinct expression profile of certain genes involved in adhesive processes. Possibly, the stronger adhesion of ER LCs led to increased interaction with surrounding niche cells, enabling niche reprogramming which ultimately protected LCs from chemotherapy and facilitated relapse development.

Taken together, the present work established a clinically relevant xenotransplantation model of larval zebrafish to study characteristics of LCs that were involved in relapse development. This model revealed interesting adhesive properties of LCs with high relapse potential, implied to complement current risk stratification and might also help to develop novel therapies.

ZUSAMMENFASSUNG

Die akute lymphoblastische Leukämie (ALL) ist die häufigste maligne Erkrankung im Kindesalter. Obwohl die Prognose nach der Erstdiagnosestellung gut ist, haben Kinder die ein Rezidiv erleiden, immer noch ein schlechtes Behandlungsergebnis. Derzeit werden Leukämiezellen (LZ) meist unabhängig von ihrem umgebenden Gewebe betrachtet, da es nur wenige Modellsystemen gibt, welche die Mikroumgebung berücksichtigen. Dadurch ist nur wenig über die Nischen-vermittelten Mechanismen der Rezidiventstehung bekannt. Dabei wird die Mikroumgebung des Tumors als immer wichtigere Komponente angesehen. In der vorliegenden Arbeit wurde ein innovatives Xenotransplantationsmodell von Zebrafischlarven entwickelt, das die Analyse von LZ in einer orthotopen Umgebung erlaubt. Dieses Modell wurde angewendet, um Charakteristika von LZ mit hohem Risikopotential in der Interaktion mit der Nische zu identifizieren.

Zunächst wurde ein robuster Xenotransplantationsprozess humaner LZ etabliert. Mittels mikroskopischer und durchflusszytometrischer Analysen konnte gezeigt werden, dass LZ die Nische erreichen, dort anwachsen und proliferieren. Darauf aufbauend wurde das Zusammenspiel zwischen LZ und Makrophagen sowie Endothelzellen charakterisiert. Dabei wurden enge und anhaltende Interaktionen von LZ mit Makrophagen, nur wenige Phagozytose-Ereignisse sowie eine geringe Infiltrationsrate mit Makrophagen beobachtet. Außerdem wurde ein spezifisches Verteilungsmuster der LZ innerhalb der Nische detektiert. Im zeitlichen Verlauf extravasierten LZ und lagerten sich zu Clustern zusammen, die in engem Kontakt mit Endothelzellen standen. Zusammenfassend konnte ein neuartiges Zebrafischmodell entwickelt werden, das die Analyse von LZ in einer funktionellen und komplexen Mikroumgebung ermöglicht.

Meine Hypothese ist, dass Leukämiezellen, die zu einem frühen Rezidiv führten, die Nische effizienter nutzten, als andere LZ. Um diese Hypothese zu prüfen, wurde mit Hilfe des neuen Xenograftmodells das Migrationsverhalten von unterschiedlichen LZ *in vivo* analysiert. Zellen von elf primären pädiatrischen B-Vorläuferleukämien wurden transplantiert und im Anschluss analysiert, fünf Patienten die ein frühes Rezidiv (early relapse = ER) und sechs, die kein Rezidiv (no relapse = NR) entwickelten. Die behandlungsnaiven Zellen stammten von der Erstdiagnosestellung. Somit konnten Unterschiede, die bereits zu diesem Zeitpunkt vorhanden waren, identifiziert werden. Mittels konfokaler Mikroskopie wurden Zeitrafferaufnahmen generiert und Parameter der Zellmigration als Messwert für die Nutzung der Nische ermittelt. Dabei wurde angenommen, dass LZ, die sich verstärkt an einer Stelle aufhalten, effizienter mit umgebendem Gewebe interagieren. Ein robuster, sensitiver, halbautomatisierter und unvoreingenommener Analyseprozess für die Nachverfolgung der LZ wurde entwickelt.

Vergleichende Analysen der ER- und NR-Patienten ergaben fünf Parameter, die ein unterschiedliches Migrationsverhalten zeigten. In der Nische migrierten ER-Zellen langsamer, hielten sich auf einer geringeren Fläche auf und waren stärker verankert, was eine stärkere Interaktion mit Nischen Zellen vermuten lässt. Ein Bewertungsschema, das die Verankerung für alle elf Patienten individuell bewertet, zeigte, dass vier der fünf ER-Patienten die höchsten Bewertungen erhielten. Diese Pilotstudie legt das Rezidiv-prognostizierende Potential des Kurzzeitassays, in einem klinisch anwendbaren Zeitrahmen von nur zwei Tagen, nahe.

Schließlich wurden Genexpressionsanalysen von Zellen, die ein klar unterschiedliches Migrationsverhalten zeigten, durchgeführt und gaben neue Einblicke in die Biologie von Zellen, die später ein Rezidiv entwickelten. ER-LZ zeigten ein spezifisches Expressionsprofil von Genen, die in adhäsiven Prozessen beteiligt sind. Möglicherweise führte die verstärkte Adhäsion der ER-LZ zu einer verstärkten Interaktion mit umgebenden Nischenzellen, was eine Umprogrammierung der Nische ermöglichte, welche die LZ vor Chemotherapie schützte und so die Rezidiventstehung erleichterte.

Zusammengefasst wurde in der vorliegenden Arbeit, ein klinisch relevantes Xenograft-Zebrafischmodell entwickelt, um Charakteristika von LZ, die zu einem Rezidiv führten, zu identifizieren. Das Modell ergab interessante adhäsive Eigenschaften von LZ mit hohem Rezidivpotential, deutete darauf hin die derzeitige Risikostratifizierung zu ergänzen und könnte bei der Entwicklung neuer Therapien helfen.

1 INTRODUCTION

1.1 Pediatric acute lymphoblastic leukemia

Leukemias are diseases of the bone marrow (BM) and represent the most common malignancy during childhood [1]. Normally, healthy hematopoietic stem cells (HSCs) differentiate and expand in numbers within the BM, to build versatile functional blood cells (Figure 1). Clinically and pathologically, different types of leukemia are defined. There are acute and chronic types, which are further subdivided into forms that affect cells of the lymphoblastic or myeloid lineage during differentiation of HSCs (Figure 1). Chronic leukemias are characterized by a relatively slow development of the malignancy by rather mature cells and are most frequent in the elderly. For acute leukemias, numbers of immature cells increase rapidly. While acute myeloid leukemia (AML) becomes more frequent with higher age, acute lymphoblastic leukemia (ALL) is most frequent in children. Symptoms of ALL are usually unspecific, such as pallor, fatigue, bleeding, infections and fever [2, 3].

Pediatric leukemias have a relative frequency of 30% among all pediatric cancers in Germany. 74% of all leukemias are B-cell precursor (BCP)-ALL, thus being the most frequent type of pediatric leukemia. Cases peak at an age of 2-4 years [1]. During BCP-ALL development, precursor cells of the lymphatic B-lineage (i) stop to differentiate and (ii) start to proliferate uncontrolled (Figure 1) [4]. Within weeks, these cells can make up to more than 90% of the BM while being completely non-functional. Leukemic infiltration of the liver, spleen, lymph nodes, mediastinum and the central nervous system is commonly observed at diagnosis [2]. There are some genetic predisposing factors known that are associated with higher risk of ALL, such as the Down Syndrome. However, for most children no inherited predisposition is recognized. Environmental factors, such as the exposure to radiation and certain chemicals are documented to increase the risk to develop ALL [2, 4].

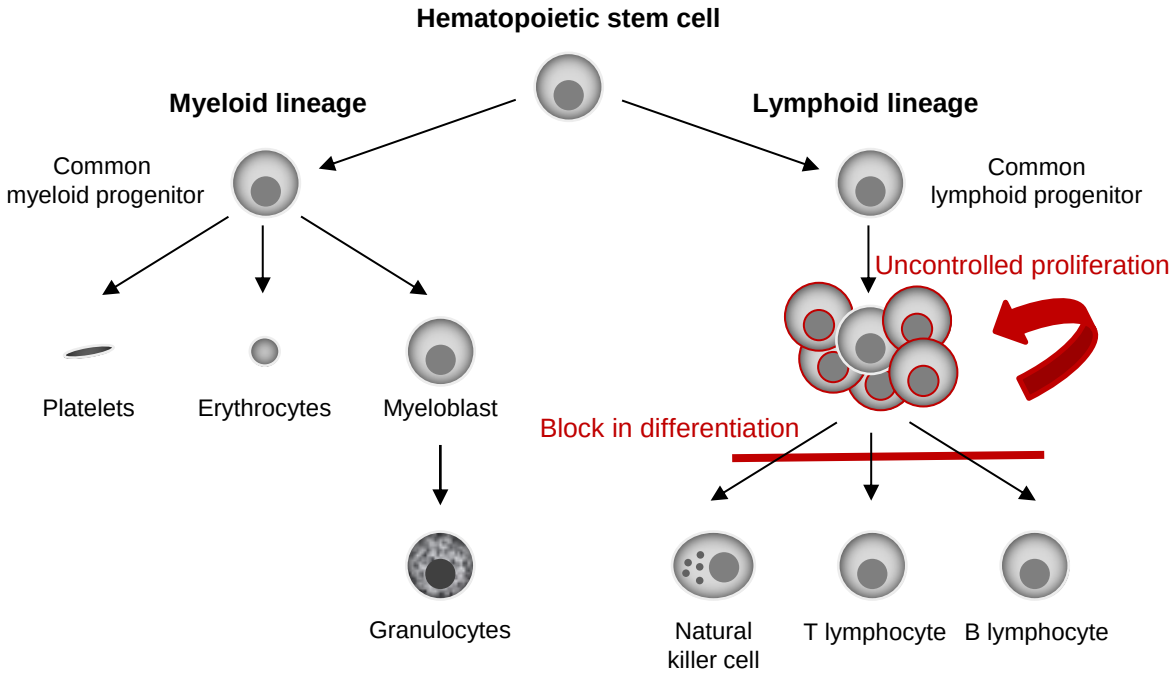

Figure 1 Hematopoietic differentiation and development of ALL.
HSCs differentiate towards a myeloid or lymphoid lineage. These progenitors physiologically give rise to platelets, erythrocytes, granulocytes, natural killer cells, T-Lymphocytes or B-Lymphocytes. For ALL development, a block in differentiation of progenitor cells and their uncontrolled proliferation leads to the massive production of non-functional ALL-cells.

1.1.1 Risk-directed treatment

Despite different risk stratification and treatment protocols are existing worldwide, there is a general consensus regarding our current understanding of the factors that put children with BCP-ALL at risk for inferior outcomes [5]. In Germany, virtually all patient are treated according to the two applicable study groups, the Berlin-Frankfurt-Münster (BFM) and Cooperative-ALL-study-group (CoALL) [6]. Relevant stratification factors include leukocyte count, age and cytogenetics at diagnosis, as well as response to therapy and end-induction minimal residual disease (MRD) after initial therapy [5, 7]. Risk-adapted therapy protocols are selected to optimally treat the disease. This approach ensures that on the one hand, side effects due to treatment toxicity are reduced for patients with low risk of relapse and on the other hand tries to guarantee the administration of more specific and aggressive drugs to patients with higher risk of relapse [6]. The detailed risk factors that are implemented in the German guidelines are summarized in Table 1 [8].

The genomic alterations and chromosomal abnormalities that characterize ALL are important for risk stratification. For instance, the gain of at least five chromosomes (high hyper-diploidy) is present in about one quarter of the diseased children and has a favorable prognosis. Leukemias with less than 44 chromosomes (hypo-diploidy) are far less frequent, however, these leukemias have a poor prognosis. Some leukemias show chromosomal translocations,

which lead to abnormal fusion proteins. MLL-rearranged leukemias have a very poor prognosis, as well as leukemia with the translocation t(9;22)(q34;q11), which leads to the generation of the fusion protein BCR–ABL (Philadelphia chromosome). In contrast, leukemias expressing the fusion protein ETV6–RUNX1 or TCF3–PBX1, translocations t(12;21)(q13;q22) or t(1;19)(q23;p13), respectively, have a favorable prognosis. In addition, there are a high number of other subgroups that were identified, having distinct gene expression profiles but cryptic cytogenetics [4].

Table 1 Risk factors for ALL [8].

Factor	Favorable prognosis	Unfavorable prognosis
Leukocyte count	< 20,000 blasts/µL	> 100,000 blasts/µL
Age	1-5 years	< 1 year, ≥ 10 years
Response after 7 days of Prednison induction therapy (plus MTX)	< 1,000 blasts/µL	≥ 1,000 blasts/µL
Response to initial induction therapy (duration 4-5 weeks)	M1-marrow*	M2-, M3-marrow* (e.g. NR Day 33)
Verification of MRD	Negative after 5 weeks	Positive ($\geq 10^{-3}$) after 12 weeks
Number of chromosomes	> 50	< 45
Translocations/Fusion genes	t(12;21)/ETV6–RUNX1	t(9;22)/BCR-ABL; t(4;11)/MLL-AF4
Probability of EFS after 5 years	0.90	0.1-0.6

* M1 -marrow: < 5% blasts; M2-marrow: 5-25% blasts; M3-marrow: > 25% blasts in bone marrow.

First-line therapy consists of multiple steps: induction, consolidation, intensification and long-term maintenance therapy. High doses of different chemotherapeutics are administered in order to eliminate malignant cells. In rare specific cases, allogeneic hematopoietic stem cell transplantation (allo-HSCT) is realized. During the past few decades, the event-free survival (EFS) rates in first complete remission (CR) increased and reach now 70-80% [4]. However, about 15-20% of all patients suffer a relapse [9, 10]. On average, only about 40% of the relapsed children can be salvaged [11].

In summary, risk-directed treatment strategies of BCP-ALL were developed and led to increased EFS rates. Still, the prognosis of patients that relapse remains poor.

1.1.2 Relapsed ALL

Risk-directed strategies are also applied for the treatment of ALL relapses. Here, the strongest prognostic factors currently known are the duration of remission after initial diagnosis and the site of the relapse [12]. Most relapses occur within the first three years after diagnosis [13]. According to the BFM group, early relapses are those that occurred ≤ 6 months after end of primary therapy, which normally ends after 24 months, while very early relapses occurred within 18 months after initial diagnosis [14]. These early relapses have a probability of overall survival (OS) of only 20% while a relapse at a later time point has a higher probability of 52% OS. Consequently, there is a significant relationship between the duration of remission after initial diagnosis and the outcome of patients. Among all patients that suffered an early relapse 20% did not respond to therapy, while only 1% of patients with later relapse did not respond. 88% of all patients that suffer a second relapse subsequently died. With regards to the site of relapse manifestation, isolated medullary relapses have the worst prognosis with an OS rate of only 26%. Isolated extramedullary relapses and medullary relapses with involvement of extramedullary sites have OS rates of 31% and 41%, respectively. Notably, these statistics include approximately 10% ALLs of the T-lineage [11].

Treatment strategies of ALL-relapses, include multi- and high-dose chemotherapy regiments. During second remission, high-risk relapses are followed by allo-HSCT. Again, the MRD-level after induction therapy is a decisive factor for further therapy decisions. Innovative therapies, for instance the bispecific monoclonal antibody Blinatumomab and immunotherapy with chimeric antigen receptor (CAR) T-cells, are applied [4, 12].

Taken together, ALL is a very frequent pediatric malignant disease of the BM. Despite improved treatment strategies, ALL represents the second leading cause of death in childhood malignancies [15]. Consequently, it is of major importance to identify patients with high-risk of relapse at the time of initial diagnosis to prevent its development. Current classification protocols mostly consider cell intrinsic features, however, considering features of the surrounding cells might help to improve risk stratification and prevent relapse development.

1.1.3 The leukemic niche

In the field of stem cell research, the term ‘niche’ describes the place of residence of stem cells where they can fulfill their desired function. Hence, the niche is (i) the anatomic region where stem cells reside and (ii) the distinct localization, where specific signals are available to enable stem cell functions, such as self-renewal and differentiation. These specific signals can be provided by the extracellular matrix, cellular components and secreted molecules, and make up the microenvironment of stem cells. Accordingly, it is the niche that triggers stem cell

fate [16]. With the development of the cancer stem cell concept of leukemia, which describes a distinct subpopulation of leukemia cells (LCs), possessing features of stem cells, such as self-renewal [17, 18], the question arose if specialized niches are equally important to maintain the leukemia, as they are for healthy tissue. In case, the niche is decisive for leukemia development or maintenance, its components are very attractive therapeutic targets to eliminate malignant cells [16]. There is growing evidence that in addition to cell-intrinsic changes, the surrounding tissue - the niche - plays a pivotal role in leukemogenesis, leukemia maintenance and ultimately in relapse development [19].

Although LCs are thought to be less anchored within their surrounding tissue than solid tumor cells, LCs reside and grow within the BM niche surrounded by a complex network of cells [20]. The BM niche of HSCs is built out of endothelial cells, mesenchymal cells, immune cells, osteocytes and adipocytes. Via cell surface and secreted molecules, such as cytokines, chemokines and growth-factors, these niche cells can get into contact with HSCs but also LCs and vice versa, in order to trigger cell fate [21]. However, little is known about the signals that drive the interplay of LCs and the microenvironment and the functions that are involved in sustaining and promoting the tumor [20].

In order to make interactions and supportive signaling of LCs and the microenvironment possible, cells need to adhere, to not get pulled apart by other forces within the tissue, for instance the blood flow. Hence, cells attach to surrounding tissue. This occurs through surface cell adhesion molecules (CAMs) via direct cell-to-cell binding or mediated via extracellular matrix (cell-to-matrix), which is a complex network of proteins and polysaccharides, secreted by the tissue cells [22]. These bonds can be formed in different constellations, depending on the CAM. Some CAMs rather form homophilic interactions, while others tend to form heterotypic bindings. In addition to the cohesive function of CAMs, they also trigger intracellular signal transduction to initiate processes, such as differentiation, proliferation or apoptosis. Generally, four types of CAMs can be distinguished based on protein sequence and structure: the (i) cadherin superfamiliy, (ii) the immunoglobulin superfamily CAM (IgCAM), (iii) selectins and (iv) integrins. For all types of CAMs, important interactions of HSCs and LCs within the niche were observed [23].

For instance, for cadherins it has been reported that N-cadherin positive LCs were able to escape from chemotherapy and had a high capacity to self-renew [24, 25]. For HSC, N-cadherin mediated interactions between HSCs and osteoclasts were detected and this process was associated with a quiescent phenotype [26]. This dormancy was equally observed for N-cadherin positive LCs as they were more likely to be arrested in G_0-G_1 phase [25]. This demonstrates that LCs are hijacking the niche of HSCs and are utilizing it for their own benefit. In addition, VLA-4 of LCs and HSCs was shown to bind to stroma cells via VCAM-1. For LCs,

this interaction led to their protection against chemotherapy [27, 28]. Furthermore, soluble molecules are important niche components, such as the chemokine CXCL12 (= SDF-1), which does not only retain healthy early B-cells within the niche, but also attracted LCs in a transmigration assay [29] and attracted LCs to the BM of xenografted mice via CXCR4 [30].

In addition to hijacking existing niche components of HSCs, there is an evidence that LCs are able to actively remodel the niche for their own benefit. The BM of leukemia patients showed an increased neovascularization, which is a well-known and important feature of solid tumors but also applies to the niche of LCs [31]. One *in vitro* study demonstrated that endothelial cells protected LCs from chemotherapy by overexpression of the anti-apoptotic protein Bcl-2 [32]. A number of studies reported that LCs are able to evade the recognition of the immune system. For instance, regulatory T-cells of patients with ALL expressed higher levels of the immune-suppressive interleukin IL-10 [33]. Tumor-associated macrophages (TAMs) were described to have both polarization capacities, immune-stimulating (M1-like) and –suppressive (M2-like) [34]. However, for a number of leukemias an increased number of M2-macrophages was found and could be associated with poor prognosis [35-37].

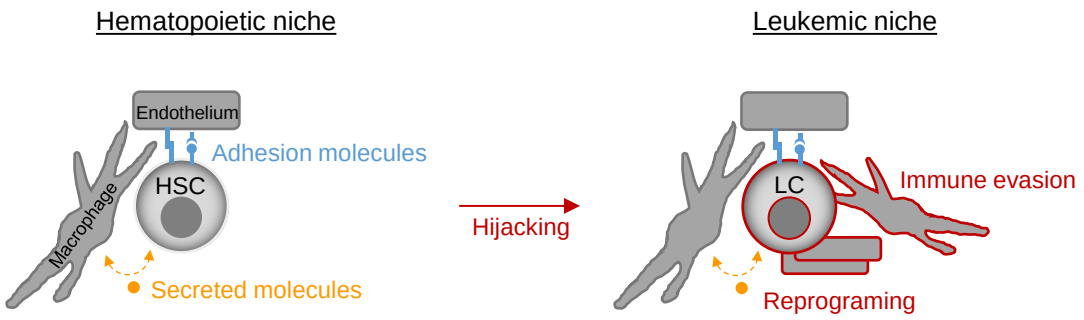

Figure 2 The leukemic niche.
HSCs reside within distinct niches. LCs are able to hijack these niches and exploit them for their own benefit. In addition, reprogramming is possible.

Taken together, LCs are in close contact with different niche components via adhesion molecules and secreted molecules. LCs are able to hijack the niche of healthy HSCs, to reprogram and thereby modify the niche for their own protection, with regards to cellular composition and gene expression. This remodeling leads to their protection against chemotherapy, the endogenous immune system and cell intrinsic apoptosis, which is ultimately advantageous for the leukemia (Figure 2). Still, too little is known about the leukemic niche of BCP-ALL and further detailed studies are needed to comprehensively understand its functions. The discovery of novel interactions of LCs and niche components and the identification of their respective leukemia supporting functions will help to develop novel strategies to fight BCP-ALL. However, models to study the complex interplay of several cell types within a functional surrounding are scarce.

1.2 The larval zebrafish as a model organism to study human leukemia

In 1981, the zebrafish (*Danio rerio*) was introduced as a novel vertebrate model organism [38]. Since then, it has become one of the main animal models in various research fields of basic and applied science. The fact that zebrafish exhibit orthologues for > 82% of human disease related genes makes it particularly suitable to investigate human diseases [39]. The zebrafish is a freshwater fish natively living in South Asia, which offers several advantages compared to conventional rodent models. Zebrafish maintenance is easy and causes low costs. A paired mating can give hundreds of fertilized eggs that develop rapidly outside the mother [40]. The availability of zebrafish embryos at the one cell stage eases genetic modification and facilitates gain- and loss-of function studies and allows the generation of fluorescent reporter fish lines [41]. A generation time of only three months simplifies working with those mutants. Already at 28 hours post fertilization (hpf), embryos have a heartbeat and at two days post fertilization (dpf), all major organs appear and can be studied [40]. One of the main advantages of the larval zebrafish model is the opportunity to monitor fluorescently labeled cells in the living organism, in real-time, using confocal *in vivo* microscopy, due to embryos' optical transparency. The establishment of completely transparent mutants, so called 'Casper' fish, facilitates imaging even at later time points [42].

1.2.1 Zebrafish hematopoiesis

Differentiated cell lineages that are generated from HSCs, as well as genes and molecular signaling pathways that are involved in hematopoiesis, are highly conserved between zebrafish and mammals. As for all vertebrates, in zebrafish, sites of hematopoiesis change over time and occur in two waves during development [43, 44]. Thus, the zebrafish is an attractive and powerful model organism to study physiological hematopoiesis and diseases of the hematopoietic system, which allows the translation of new findings to humans.

In zebrafish, at roughly 12 hpf, the "primitive" wave of hematopoiesis takes place in the intermediate cell mass (ICM) and the rostral blood island (RBI). Erythrocytes, as well as some primitive macrophages are produced. In humans, this wave takes place in the extraembryonic yolk sac [45]. During the "definitive" wave of human hematopoiesis, HSC, which can differentiate into all blood lineages emerge in the aorta-gonad-mesonephros, then move to the fetal liver and ultimately colonize the BM [43]. A comparable transition can be observed in zebrafish. First, at around 26 hpf, HSCs emerge via endothelial-to-hematopoietic transition between the dorsal aorta and the posterior cardinal vein, the ventral dorsal aorta. Next, starting at 48 hpf, HSCs move to the caudal hematopoietic tissue (CHT), the intermediate site of hematopoiesis, equivalent to the human fetal liver. Finally, starting at around 96 hpf, HSCs

colonize the kidney marrow, which is the equivalent to the human bone marrow and the site of definitive adult hematopoiesis [46] (Figure 3).

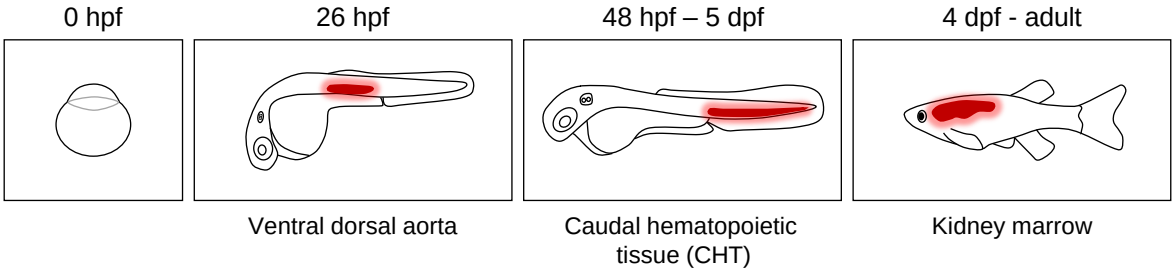

Figure 3 Sites of definitive hematopoiesis in zebrafish.
Sites of definitive hematopoiesis at the depicted developmental stages of zebrafish are highlighted in red. During definitive hematopoiesis, HSCs can differentiate into all blood cells.

Studying physiological hematopoiesis in the CHT of larval zebrafish led to a number of new discoveries. Researchers took advantage of the easy accessibility of the CHT via microscopy, which allowed studying this multicellular tissue with single cell resolution *in vivo* in real-time. The CHT is a vascular plexus in the ventral region of the tail between the caudal artery (CA) and cardinal vein (CV). Vascular endothelial cells line the inside of the vessels of the blood circulation system. In the CHT, fenestrated endothelial cells are loosely connected and allow HSCs to extravasate. A number of cytokines are produced by endothelial cells to attract and retain HSCs [46]. After HSCs extravasate, endothelial cells remodel around the HSC. This so called “endothelial cuddling” leads to cell division of HSCs. Endothelial cells are closely associated with mesenchymal stroma cells that express the chemokine CXCL12. During endothelial cuddling, these stroma cells appear to be important for cell retention and division [47]. In stroma cell deficient zebrafish HSCs are able to find the CHT but cannot be retained or expanded [48]. Furthermore, cells of the innate immune system can also be found in the CHT and are reported to closely interact with HSC. VCAM-1 positive macrophage-like cells patrol in the CHT and interact with directing HSC retention [49]. In macrophage deficient zebrafish the number of HSCs in the CHT is decreased, underlining the importance of macrophages in healthy hematopoiesis [50].

These key findings of vertebrate hematopoiesis within the CHT demonstrate the exceptional advantages of the zebrafish model. The microscopic accessibility of the CHT together with the high conservation of the hematopoietic system between humans and the zebrafish enables the detailed observation of cellular processes within the hematopoietic niche, like no other animal model.

1.2.2 Zebrafish cancer models

Since its discovery as an attractive animal model forty years ago, it became apparent that zebrafish are highly suitable to study cancer. Fish can develop cancer in a number of ways. Tumors can occur naturally or develop via exposure to carcinogens [51] or mutagens [52]. In addition, transgene expression of the murine oncogene c-myc under the zebrafish rag2 promotor led to T-cell leukemia development. This model developed by Langenau et al. represented the first leukemia zebrafish model [53]. Furthermore, mutations of the tumor suppressor p53 resulted into the development of malignant tumors [54]. Despite major successes, these methodologies have certain limitations. Not all genes, mutations and other features of human malignancies can be easily modeled using genetic approaches. Thus, xenotransplantation models were developed.

1.2.3 Xenotransplantation models

To better recapitulate features of human malignant cells, their xenotransplantation is necessary. Xenotransplantation is the process by which cells of one species are transplanted into another. This method is commonly performed for preclinical research to study malignant diseases of human cells in an animal model. The cornerstone of recipient animals are immunocompromised mice, which allow the reliable transplantation of human material without rejection of the host [55], however, other species are conceivable.

The first xenotransplantation of human cancer cells into zebrafish was performed in 2005. Lee et al. showed survival, proliferation and motility of melanoma cells when injected into the blastula stage of zebrafish embryos [56]. Subsequently, numerous further studies of different tumor entities followed and the process of xenotransplantation was optimized [57, 58]. For almost all studies, human cells were fluorescently labeled to be retrieved after transplantation using various dyes. The difference of human and zebrafish body temperature of 37°C and 28°C, respectively, was taken into consideration and experiments showed that zebrafish could be kept at 35°C after transplantation [57]. A more recent study showed that zebrafish larvae tolerate up to 36°C without developmental defects [59]. Transplantations at 48 hpf turned out to be ideal as at this time point, major organs are developed while the adaptive immune system is not fully established until 4-6 weeks post fertilization [60]. Therefore, embryos are excellent recipients for xenogeneic cells and require no additional immune suppression. Nevertheless, functions of the innate immune system, such as the interplay with macrophages, can be investigated, since they are already present by 24 hpf [61]. This routine transplantation workflow was successfully applied by many labs and allows the efficient injection of several hundred embryos within only a few hours (h). In 2011, the first LCs were successfully transplanted, including the cell lines NB4 (acute promyelocytic leukemia), K562 (chronic

myelogenous leukemia) [62, 63], Jurkat (acute T-cell leukemia) and primary AML cells [62]. To date, larval xenografts are an appreciated model and were successfully used to study diverse processes, such as tumor metastasis [64, 65] and angiogenesis [57, 58, 66]. Furthermore, numerous studies emphasize the potential of the larval zebrafish as a preclinical model to test drugs [62, 63, 67-69].

Efforts were made to perform xenotransplantation even into adult fish to complement mice with regards to pre-clinical studies. In 2019, Yan et al. introduced a zebrafish strain that is deficient for T-, B-, and NK-cells, which allows the robust engraftment of numerous human cancer entities in adult fish and leads to growth kinetics and histopathology that are comparable to those seen in immune-deficient mice [70].

Taken together, a new era of xenotransplantation has just started using zebrafish. The major tools are established and its great potential to answer questions of basic and applied science was shown.

1.2.4 Patient-derived xenografts

Meanwhile, xenografts of human cell lines are routinely used, and researcher endeavored to transplant primary patient-derived cells to establish zebrafish patient-derived xenografts (PDX). Primary cells possess several advantages compared to conventional cell line models, which are genetically manipulated, oftentimes acquired unphysiological mutations during passaging and lack the heterogeneity of the original tumor [71]. Furthermore, limited clinical information is available regarding the clinical course, which can be important for some studies.

In 2009, Marques et al. analyzed the metastatic behavior of primary human pancreas, colon and stomach cancers compared to matching healthy tissue in the zebrafish model. Real-time *in vivo* imaging of the larvae allowed discrimination of invasive and non-invasive tumors within only three days. Metastasis could be found at various sites of the transplanted animals [72]. Similar results were observed by other groups [73]. Especially in the field of personalized medicine, expectations on zebrafish-avatars are high in order to identify appropriate therapeutics for individual patients in a time and cost effective setting. Zebrafish PDX of a child with T-ALL responded to treatment with γ-secretase, which led to the identification of a gain-of-function NOTCH1 mutation of this patient [67]. Drug treatment of larvae transplanted with $CD138^+$ plasma cells derived from patients with multiple myeloma showed comparable response to drugs when compared to the patients clinical data [74]. In addition, adult immunodeficient zebrafish PDX models demonstrated their potential to perform drug screens to assess treatment response of individual patient or to perform preclinical studies [70].

In summary, for both, larval and adult zebrafish, primary patient cells were transplanted and patients-avatars were established. Despite the fact that zebrafish PDX models are in their infancy, these studies proved their potential in helping to estimate disease progression and to develop patient-tailored therapy strategies in feasible time frame for the clinic.

1.3 Studying cell migration and interaction in the hematopoietic niche *in vivo*

In order to study processes of cellular interactions, localization, movement and adhesion *in vivo,* microscopy based assays were developed to directly monitor the cells. As the hematopoietic niche of mammals is located in the bone, the analysis of intravital dynamic processes, of therein located cells, is very challenging and requires immense technical efforts, such as two photon imaging and calvarial windows [75-77]. It is limited to a very low number of mice that can be analyzed and even more important, the ethic ambivalence of such highly invasive experiments are questionable. In larval zebrafish, the niche is readily accessible for conventional confocal microscopy enabling the analysis of cellular dynamics of fluorescently labeled cells in the living organism much easier.

For *in vivo* imaging, optical transparent larvae merely need to be anesthetized and embedded into agarose, no further preparations are necessary to access the hematopoietic niche with single cell resolution. Time lapse movies of confocal microscopy visualized dynamic interactions of endothelial cells and HSCs in the CHT [47]. Furthermore, larvae were widely used to study dynamics of immune cells, such as macrophages and neutrophils in basic research [78, 79] but also in the presence of malignant cells, where Tulotta et al. was observed that CXCR4 expression of neutrophils was involved in developing tumor metastases of breast cancer [80]. In addition, light sheet microscopy was used to assess dissemination of tumor cells within the whole larva after xenotransplantation [81]. To quantitatively analyze migration of the cells, different tools were applied to track the cells of interest either manually using the open source platform ImageJ with the help of plugins [78-80] or automated using the commercial software Imaris [78].

In summary, analyzing the movement of LCs within the hematopoietic niche is far easier in zebrafish larvae than in murine models. Little effort is needed to access the niche area and analyze cellular characteristics with single cell resolution in real-time. Currently, a number of approaches analyzed the migration of different cells in the zebrafish and provide interesting results on the dynamics of cells in a living organism.

1.4 Larval zebrafish xenografts as a tool to study tumor-microenvironment interactions

Studying the microenvironment of malignant diseases is important to identify interactions between the malignant cells and healthy neighboring cells that could be involved in tumor development and progression, therapy resistance and relapse development.

Larval zebrafish xenografts are very suitable to study the tumor microenvironment in single cell resolution using *in vivo* imaging. There are numerous reporter fish lines available with fluorescently labeled cells of interest. Tg(kdrl:eGFP) zebrafish express eGFP under the control of the endothelial specific promoter kdrl, leading to a specific labeling of endothelial cells. High resolution imaging dynamically visualized the process of angiogenesis on single-cell level and allowed quantitative analysis [66]. Transplanting human cell lines with known pro-angiogenic effects resulted in neo-vascularization of the tumor, while this was not the case for other cell lines [58]. Whole mount immunostainings followed by histologic analysis showed the interaction of melanoma cells with zebrafish endothelial cells and activated endothelial cells were detected [57]. This data provides evidence that human growth factors are functional in the zebrafish.

As mentioned before, larval zebrafish lack adaptive immunity while cells of the innate immune system are present and can be studied. Performing high resolution imaging showed how physiologically migrating zebrafish neutrophils control tumor invasion by changing the collagen matrix leading to suitable metastatic niches of breast cancer [65]. Using a Cre/LoxP strategy, it was observed that macrophages and human melanoma cells are able to communicate via cytoplasmic transfer. This interaction led to an increased tumor cell motility and dissemination [82]. Sacco et al. transplanted multiple myeloma cells into the circulation of embryos. In their study they were able to show that human cancers that tend to build BM metastasis engraft in the CHT, whereas others do not [83]. This result underlines that studying the CHT is a powerful tool to study disease of the BM.

Disease related genes are highly conserved between humans and zebrafish [39]. When analyzing interactions of LCs and niche cells, soluble factors like cytokines and growth factors are interesting. In several studies, the extent of conservation of such molecules was analyzed. Despite zebrafish having two variants of the cytokine CXCL12 and humans only one, 74% of the protein sequence are identical [84]. Moreover, adhesion molecules are conserved, as for instance, the integrin ITGB1 and the protocadherin FAT1, show 76% and 64%, respectively, identical sequences to humans [85, 86]. For E-selectin, five functional important domains are highly conserved [87]. Despite a large overlap of human and zebrafish molecules, there are some that have no cross-reactivity or orthologue, such as zebrafish lack both the ligands and

receptors for the IL-3 subfamily, which includes IL-5, GM-CSF, and IL-3 [88]. To overcome such limitations, humanized animal models were developed. In 2020, Rajan et al. established the first humanized zebrafish line of hematopoietic-specific cytokines (GM-CSF, SCF, and SDF1α) [89]. These so called GSS-fish led to an increased homing to the CHT and proliferation of primary human LCs [89].

In conclusion, there is evidence that larval zebrafish xenografts are highly suitable to study human cancers and their microenvironment in real-time. Numerous studies demonstrated the direct interaction and communication of human and zebrafish cells that nicely resembled clinical features of the patients. In the future, humanized zebrafish models might even improve the analysis of the complex interplay of cancer cells within their niches. However, to date, no publication describes a model to study leukemia-niche interactions in larval zebrafish.

1.5 Aim of the project

Children with ALL that suffer from relapse have a poor prognosis. The tumor microenvironment is recognized as an important component and suggested to play a decisive role during relapse development. However, little is known about niche-mediated mechanisms that are involved in relapse development and model systems that consider the microenvironment are rare.

The present work aimed at establishing an innovative larval zebrafish xenotransplantation model to study leukemia within an orthotopic niche in order to identify characteristic interactions of LCs that later developed relapse, with their microenvironment. Towards this aim, a robust workflow for the xenotransplantation of pediatric BCP-ALL was generated and the interplay with certain niche cells was characterized, to evaluate its suitability to study LCs in a functional and complex microenvironment. Next, the model was used to identify differential migration behavior, as a measurement for niche interaction, of primary LCs with different relapse potential. The prognostic impact of the identified migration patterns on relapse development was assessed. Ultimately, cells with distinct differences in motility were transcriptionally analyzed to identify underlying mechanisms, which might play a role in relapse development of these cells.

Taken together, this project aimed at developing a pioneering *in vivo* model that allows the identification of novel characteristics of LCs with high relapse potential in their interaction with the microenvironment. These new insights will propose novel risk stratification strategies and therapeutic targets, ultimately helping patients in the future.

2 MATERIALS

2.1 Zebrafish

Table 2 Zebrafish lines.

Name	Source
Casper line (roy-/- nacre-/-) wild-type	L. Zon, Harvard Medical School, Boston, MA [42]
Tg(kdrl:mCherry)*	unknown
Tg(mpeg1:mCherry-F)*,°	A. Meijer, Leiden University, Leiden, Netherlands [90]
Wild-type line AB	Zebrafish International Resource Center (ZIRC), University of Oregon, Eugene, USA

* Respective 'Casper'-Reporter lines were generated by out-crossing the reporter fish line with the 'Casper' wild-type line.
° '-F' indicates farnesylation of mCherry.

2.2 Cells

2.2.1 Cell lines

NALM-6 cells were purchased from DSMZ, Braunschweig, Germany. EGFP or mCherry expressing NALM-6 cells were generated and provided by the laboratory of Irmela Jeremias, Helmholtz Zentrum, Munich, Germany.

2.2.2 Primary cells

All primary cells were obtained from the Dr. von Haunersches Kinderspital, Klinikum der LMU, Munich, Germany (see 3.1.1 for details).

2.2.3 Mouse-PDX cells

Mouse-PDX cells were kindly provided by the laboratory of Irmela Jeremias, Helmholtz Zentrum, Munich, Germany (see 3.2.3 for details).

2.3 Oligonucleotides

Table 3 Primer for PCR to determine knockout efficiencies.

Name	Sequence (5' → 3')
sele_1_fwd	CGTTTGTTCTTATCTCTTCAGG
sele_1_rev	CATAGAAGCCTTCAAAGCATG
sele_2_fwd	GGTAAATGGAATGATGAATCCTG
sele_2_rev	GTGGTTTGTTCAGCTGTG

Table 4 crRNA sequences.

Name	Target Gene	Targeted Exon	Sequence (5' → 3')
crRNA_sele_1	E-selectin	3	TAATAACCAGTGGACCTGGG
crRNA_sele_2	E-selectin	4	GACACAGGAGTCACTCGCGC
crRNA_nt_1*	non-targeting	-	CAGGCAAAGAATCCCTGCC
crRNA_nt_2*	non-targeting	-	TACAGTGGACCTCGGTGTC
crRNA_nt_3*	non-targeting	-	CTTCATACAATAGACGATG

For gRNA design see 3.3.5.1.
*sequences for non-targeting control were adopted from Wu et al. [91].

2.4 Chemicals and reagents

Table 5 Chemicals and reagents.

Reagent	Producer
Agarose	Invitrogen™, Waltham, MA, USA
Alt-R® CRISPR/Cas9 crRNA	Integrated DNA Technologies, Coralville, Iowa, USA
Alt-R® CRISPR/Cas9 tracrRNA	Integrated DNA Technologies, Coralville, Iowa, USA
Alt-R® S.p. Cas9 Nuclease V3	Integrated DNA Technologies, Coralville, Iowa, USA
BSA	Carl Roth, Karlsruhe, Germany
$CaCl_2$	Merck KGaA, Darmstadt, Germany

Reagent	Producer
CellTrace™ CFSE Cell Proliferation Kit	Invitrogen™, Waltham, MA, USA
Dead cell removal kit	Miltenyi, Bergisch Gladbach, Germany
DMSO	Sigma-Aldrich, St. Louis, MO, USA
FBS	Gibco, San Diego, CA, USA
Fixable Viability Dye eFluor 450	eBioscience, San Diego, CA, USA
Gentamycin 50 mg/mL	Lonza, Basel, Switzerland
KCl	Merck KGaA, Darmstadt, Germany
Liberase™ TM Research Grade	Sigma-Aldrich, St. Louis, MO, USA
MetaPhor™ Agarose	Lonza, Basel, Switzerland
Methanol	Carl Roth, Karlsruhe, Germany
NaCl	Carl Roth, Karlsruhe, Germany
NaOH (1N)	Merck KGaA, Darmstadt, Germany
N-Phenylthiourea	Sigma-Aldrich, St. Louis, MO, USA
Penicillin/Streptomycin (10,000 U/mL)	Gibco, San Diego, CA, USA
Phusion® High-Fidelity PCR Master Mix with HF Buffer	New England Biolabsm, Ipswich, MA, USA
Primer	Sigma-Aldrich, St. Louis, MO, USA
Pronase	Sigma-Aldrich, St. Louis, MO, USA
Single Cell 3’ v3 kit	10X Technologies, Inc., Pleasanton, CA, U.S.
Tricain	Sigma-Aldrich, St. Louis, MO, USA
TRIS Hydrochloride	Carl Roth, Karlsruhe, Germany
Trypan blue	Sigma-Aldrich, St. Louis, MO, USA

2.5 Buffers and media

Table 6 Commercial buffers and media.

Reagent	Producer
Binding buffer	Miltenyi, Bergisch Gladbach, Germany
DPBS	Gibco, San Diego, CA, USA
FACS Buffer	BD Bioscience, Heidelberg, Germany
HEPES Buffer 1M	Lonza, Basel, Switzerland
IDTE Buffer	Integrated DNA Technologies, Coralville, Iowa, USA
RPMI 1640	Gibco, San Diego, CA, USA
StemSpan™ SFEM	STEMCELL Technologies, Vancouver, Canada

Table 7 Homemade buffers and media.

Name	Components	Amount
Cas9-working-buffer (pH=7.5)	H2O HEPES KCl	 20 mM 15 mM
E3-medium	H_2O $CaCl_2$ KCl NaCl	 0.33 mM 0.17 mM 5 mM
Freezing-medium	Heat inactivated FBS DMSO	90% 10%
PBS-BSA-buffer	DPBS BSA	 0.5%
RPMI-medium	RPMI 1640 FBS	 10%

Name	Components	Amount
StemSpan-medium	StemSpan™ SFEM	
	Penicillin	100 Units/mL
	Streptomycin	100 Units/mL
	Gentamycin	100 µg/mL
TRIS-buffer (pH = 8)	H_2O	
	TRIS Hydrochloride	1 M

2.6 Consumables

Table 8 Consumables.

Name	Producer
4 Chamber 35 mm Glass bottom dish, well 20 mm, glass thickness #1.5	Cellvis, Mountain View, CA, USA
Borosilicate Glass Capillaries 1B120F-4	World Precision Instruments, Sarasota County, FL, USA
BRAND® PCR tubes,	Sigma-Aldrich, St. Louis, MO, USA
Cell culture flask (T25, T75)	Greiner bio-one, Kremsmünster, Germany
Cell strainer 30µm	Corning, Corning, NY, USA
Centrifuge tubes (15 mL, 50 mL)	Greiner bio-one, Kremsmünster, Germany
Cryotubes	Thermo Fisher Scientific, Waltham, MA USA
Disposable serological pipettes (5 mL; 10 mL, 25 mL)	Greiner bio-one, Kremsmünster, Germany
Eppendorf reagent tubes (1.5 mL, 2 mL)	Greiner bio-one, Kremsmünster, Germany
FACS tubes (with and without filter)	Corning, Corning, NY, USA
LS columns	Miltenyi, Bergisch Gladbach, Germany
Petri dishes	SARSTEDT, Nümbrecht, Germany
Pipette tips (with and without filter)	Starlab, Hamburg, Germany
Well-plates for tissue culture	Corning, Corning, NY, USA

2.7 Technical equipment

Table 9 Technical equipment.

Device	Name	Producer
Biological safety cabinet	Safe 2020	Thermo Fisher Scientific, Waltham, MA USA
CO_2 Incubator	Heracell 150L	Thermo Fisher Scientific, Waltham, MA USA
Confocal spinning disc microscope	Axio Observer Z1; CSU-X1 Yokogawa Spinning Disc; Axio Cam MRm	Zeiss, Oberkochen, Germany
Confocal spinning disc microscope	Nikon ECLIPSE Ti2; Andor Dragonfly 500; iXon Life 888	Nikon, Tokio, Japan Oxford Instruments, Abingdon, UK
Flow Cytometer	BD LSR Fortessa X20	BD Bioscience, Heidelberg, Germany
Fluorescence Stereomicroscope	SteREO Discovery.V8; Axiocam HRc; HXP 120 V Compact Light Source	Zeiss, Oberkochen, Germany
Freezing container	Nalgene Mr.Frosty	Sigma-Aldrich, St. Louis, MO, USA
Heat block	Thermomixer-Mixer HC	Starlab, Hamburg, Germany
Magnet for MACS	QuadroMACS Separator	Miltenyi, Bergisch Gladbach, Germany
Microinjector	FemtoJet 4i	Eppendorf, Hamburg, Germany
Needle puller	DMZ-Universal-Electrode-Puller	Zeitz Instrumente, Martinsried, Germany
Sequencing platform	Illumina Novaseq 6000	Illumina Inc., San Diego, CA, USA
Single-cell analysis platform	Chromium X Series	10X Technologies, Inc., Pleasanton, CA, U.S.
Stereomicroscope	Stemi 2000-C	Zeiss, Oberkochen, Germany
Thermocycler	ProFlex PCR System	Applied Biosystems, Waltham, MA USA
Water Purification System	Milli-Q® Reference	Merck KGaA, Darmstadt, Germany
Zebrafish incubator 28.5°C or 36°C	MIR-154-PE	Panasonic, Wiesbaden, Germany

2.8 Software

Table 10 Software.

Software	Supplier
Axiovision 4.0	Zeiss, Oberkochen, Germany
BD FACSDiva™	BD Bioscience, Heidelberg, Germany
Benchling	Benchling, San Francisco, CA, USA
Endnote X9	Clarivate, Philadelphia, PA, USA
FlowJo 10.6.1	FlowJo, Ashland, OR, USA
Fusion 2.2	Oxford Instruments, Abingdon, United Kingdom
GraphPad Prism 7	GraphPad Software, San Diego, CA, USA
ImageJ *	NIH, Bethesda, MD, USA
Imaris 8.3.1	Oxford Instruments, Abingdon, United Kingdom
Ingenuity Pathway Analysis	Qiagen, Venlo, Netherlands
Microsoft Office 2016	Microsoft Corporation, Tulsa, OK, USA
Python	Python Software Foundation, Wilmington,NC, USA
RStudio (R version 3.6.1)	Rstudio, Boston, MS, USA
TIDE version 3.2.0	The Netherlands Cancer Institute, Amsterdam, Netherlands
ZenBlue 2011	Zeiss, Oberkochen, Germany

* required plugins: MutiStackReg, TrackMate

3 METHODS

3.1 Ethical statements

3.1.1 Patient material

Primary patient material of the children was collected solely for diagnostic purposes. For all samples used in this study, written approval of the parents was given that leftover material could be frozen and archived for later research questions. The study was performed in accordance with the ethical standards of the responsible committee on human experimentation (written approval of the 'Ethikkommission der Medizinischen Fakultät der LMU München' with the numbers 19-495, 068-08 and 222-10) and with the Helsinki Declaration of 1975, as revised in 2000.

3.1.2 Animal work

Zebrafish (Danio rerio) were maintained at the research animal facility of the DZNE (Deutsches Zentrum für Neurodegenerative Erkrankungen e. V.) in Munich, Germany. All animal trials were performed in accordance with the official committee on animal experimentation. According to German law (Tierschutz-Versuchstierverordnung – TierSchVersV - §14), no specific approved animal protocol was necessary for the present study. Zebrafish larvae did not exceed an age of 5 days post fertilization and therefore, they do not take up nutrition by themselves. Animal husbandry of all lines used for this study are allowed with written approval by Regierung von Oberbayern, numbers GZ:55.21-54-2531-127-10, GZ:55.2-1-54-2532.0-50-2016, ROB-55.2-2532.Vet_03-16-50, ROB-55.2-2532.Vet_02-20-107.

3.2 Cell culture

All cells were cultured under constant humidity at 37°C and 5% CO_2 in an incubator and were processed in a safety cabinet to guarantee sterile handling.

3.2.1 Cell counting

Cell numbers were determined using a Neubauer chamber. An aliquot of cells was adequately diluted and stained with 10% Trypan blue to discriminate between living (colorless) and dead cells (blue). 10 µL of the cell suspension were filled into the chamber and the four quadrants were counted. Cell concentration was calculated as follows:

$$\text{Cell concentration}\left[\frac{\text{cells}}{\text{mL}}\right] = \text{Mean of counted cells per quadrant} * \text{dilution factor} * 10^4 \left[\frac{\text{cells}}{\text{mL}}\right]$$

3.2.2 Cell lines

3.2.2.1 Cultivation of cell lines

Suspension cell lines were maintained at a cell density between 0.1–2 x10⁶ cells/mL in RPMI-medium with 10% heat inactivated fetal bovine serum (FBS) and typically passaged twice per week.

3.2.2.2 Freezing and thawing of cell lines

For freezing, cells were centrifuged (400 g, 5 min, RT) and resuspended in freezing-medium at a concentration of 10 x10^6 cells/mL. Cells were transferred into cryovials and placed into freezing containers and stored at -80°C. For thawing, cryovials were rapidly warmed to 37°C and the cell suspension was washed with 10 mL DPBS. After centrifugation (400 g, 5 min, RT), the pellet was resuspended in 5 mL growth medium and the cells were seeded into a 25 cm^2 flask. After reaching confluence, cells were split and cultivated for at least three days before using them for experiments.

3.2.3 Mouse ALL-PDX cells

Mouse-ALL-PDX cells were kindly provided by the laboratory of Irmela Jeremias, Helmholtz Zentrum, Munich, Germany). ALL-PDX cells were generated by serial passaging in NOD.Cg-Prkds^{scid}Il2^{rgtm1Wjl}/SzJ (NSG) mice. Cells were freshly isolated from bone marrow or spleen of transplanted mice. Cells were either directly transplanted into zebrafish larvae (see 3.3.3) or first stained with Carboxyfluorescein Succinimidyl Ester (CFSE) (see 3.2.5). For short-term *in vitro* culture, cells were kept just like primary cells (see 3.2.4.2).

3.2.4 Primary cells

3.2.4.1 Thawing of primary cells

Cryovials were warmed up to 37°C and the cell suspension was washed with 10 mL DPBS. After centrifugation (300 g, 5 min, RT), the pellet was once again washed with 10 mL PBS-BSA-buffer (300 g, 5 min, RT). Cells were immediately subjected to CFSE staining (see 3.2.5).

3.2.4.2 Short-term culture of primary cells

Cells were cultivated for 16 - 24 h in StemSpan-medium at a density of 5 x10^6 cells/mL, prior to dead cell removal (see 3.2.6) and transplantation into recipient zebrafish larvae (see 3.3.3)

or fixation (see 3.2.7) for single cell RNA sequencing.

To evaluate *in vitro* proliferation, a small fraction of cells was kept in culture in StemSpan-medium at a density of 0.5 x10^6 cells/mL.

3.2.5 CFSE-staining

CFSE is a fluorescent cell staining dye, which penetrates the cell membrane and binds covalently to intracellular molecules. With this covalent binding, CFSE was retained within the cells. CFSE was used to label primary cells and to monitor cell proliferation of cell lines and ALL-PDX cells.

CFSE was dissolved in DMSO to a concentration of 5 mM. 2x CFSE-staining solution was prepared with a concentration of 10 µM CFSE in PBS-BSA-buffer. Cells were counted (see 3.2.1), resuspended in PBS-BSA-buffer at a density of 4 x10^6 cells/mL, an equal volume of 2x CFSE staining solution was added to reach a final concentration of 5 µM CFSE in PBS-BSA-buffer. Cells were incubated for 15 min at 37°C. To stop the staining process, 10% chilled FBS were added. Cells were washed twice in 10 mL PBS-BSA-buffer (300 g, 5 min, RT) and resuspended in the appropriate culture medium. All cells were kept in culture for at least 16 h prior to xenotransplantation (see 3.3.3), to avoid unspecific background CFSE signal.

3.2.6 Enrichment of viable cells

Magnetic-activated cell sorting (MACS) was used for enrichment of viable cells. Cell debris, dead cells, and dying cells are labelled and removed by magnetic separation using the dead cell removal kit (DCRK).

Cells that should be enriched for living cells were pelleted (300 g, 5 min, RT), and resuspended with 100 µL beads solution and incubated for 15 min in the dark. 2 mL Binding-buffer were added and the suspension was loaded on an equilibrated LS column. Viable cells were collected according to the manufacturer's instructions (300 g, 10 min, RT) and either transplanted (see 3.3.3) or fixed (see 3.2.7) for single cell RNA sequencing.

3.2.7 Methanol fixation of cells

1 x10^6 cells were pelleted (400 g, 5 min, RT) and resuspended in 100 µL chilled DPBS. 900 µl of chilled methanol were added dropwise during very gentle vortexing. The sample was kept on ice for 15 min, subsequently, samples were stored at -20°C overnight and transferred to -80°C for long-term storage. Fixed cells were subjected to single cell RNA sequencing (see 3.7.1).

3.3 The larval zebrafish xenograft model

3.3.1 Zebrafish husbandry

Wild-type and transgenic zebrafish were kept, mated and raised according to standard protocols [92], at the zebrafish facility at the DZNE in Munich, Germany. Embryos, larvae and adult fish were only handled when used for the experiment.

3.3.2 Breeding and rearing

In the evening, one female and one male adult zebrafish were transferred from tanks to mating boxes. For genetic manipulation of eggs, dividers were inserted to control time of fertilization. The next morning, eggs were collected either directly or after removing the dividers and transferred to a petri dish containing E3-medium and either injected for genetic manipulation (see 3.3.5.3) or kept at 28.5°C. The following day, solely fertilized eggs were transferred in fresh E3-medium for further handling. To enzymatically remove the chorion, eggs were treated with 12 µg/mL Pronase in E3-medium at around 24 hours post fertilization (hpf). At 48 hpf, hatched larvae were transferred in fresh E3-medium and used for xenotransplantation (see 3.3.3). Experimental larvae, either transplanted or untransplanted control siblings were reared at 36°C up to an age of maximal 5 dpf with daily exchange of E3-medium.

To suppress pigmentation of larvae that did not have a Casper-Phenotype, larvae were continuously raised in E3-medium plus 75 µM N-Phenylthiourea (PTU) from 24 hpf on, for the duration of the experiment [93].

3.3.3 Xenotransplantation of LCs

In case parents that were heterozygote for the required fluorescent reporter-transgene were used for breeding, exclusively reporter positive larvae were sorted under a fluorescent microscope. Larvae that developed from different clutches were pooled for one experiment to obtain enough individuals for xenotransplantation, in case several mating gave eggs. Larvae used for different groups were selected randomly from the pool.

Pulled glass capillaries (needle puller with the program P(A)60) were loaded with a cell suspension containing 1 x10^5 cells/µL in DPBS. At 48 hpf, hatched and morphologically normal developed embryos were anesthetized (750 µM Tricain) and transferred on an agarose plate (0.5% agarose in E3-medium). Embryos were orientated laterally and transplanted using a microinjector. Approx. 5 nL, which contained approx. 200-500 cells, were transplanted into the blood circulation via the duct of Cuvier. Transplanted embryos were transferred in fresh E3-

medium and raised at 36°C. Generally, more embryos were transplanted than needed for the experiment.

Daily, xenografts were checked for morphologic normal development, dead or malformed individuals were removed and E3-medium was exchanged.

3.3.4 Random selection of individuals for experiment

After transplantation, larvae with transplanted LCs in the CHT were selected for the experiment using a fluorescent microscope. Individuals used for different groups of one experiment were chosen randomly. Animal numbers analyzed for each experiment are indicated in the respective figure legend.

3.3.5 Generation of E-selectin knockout larvae using CRISPR/Cas9

3.3.5.1 gRNA design

For successful generation of knockout (KO) larvae, the Clustered Regularly Interspaced Short Palindromic Repeats (CRISPR) / Cas9 system was used. Suitable guideRNA (gRNA) sequences that specifically target the genomic region of interest were designed using http://www.benchling.com according to the homepages' recommendations.

Here, the *sele* gene of the Zv9 (danRer7, Danio rerio) genome was selected. First, exons that are present in all transcripts of the gene were identified. Next, 20 nucleotide long sequences followed by a NGG protospacer adjacent motif (PAM) were generated. Ultimately, sequences were selected with an on-target score > 60 and an off-target score > 50. Targeting exons closer the 5' end is more prone to result in a nonfunctional protein when frameshift mutations happen. The two best sequences according to these recommendations were selected and used as crRNAs.

Sequences for non-targeting (nt) controls were adopted from Wu et al. [91].

3.3.5.2 Assembly of ribonucleoproteins

Ribonucleoproteins (RNPs) were assembled using the Alt-R CRISPR/Cas9 System of Integrated DNA Technologies (IDT, Coralville, Iowa, USA).

Lyophilized CRISPR RNA (crRNA) and trans-activating CRISPR RNA (tracrRNA) were reconstituted in nuclease-free IDTE-buffer according to the manufacturer's recommendation to reach a concentration of 100 µM. These stock solutions were diluted to obtain working concentrations of 6 µM and stored at -20°C. Lyophilized Cas9 protein was reconstituted in Cas9-working-buffer to obtain a concentration of 10 µg/µL. This stock solution was diluted in

Cas9-working-buffer to reach a working concentration of 0.5 µg/µL.

Shortly before injection, crRNA (6 µM) and tracrRNA (6 µM) were mixed 1:1 and annealed at 95°C for 5 min to build a gRNA and allowed to cool down at room temperature for 10 min. The RNP complex was assembled by mixing equal volumes of the annealed gRNA (3 µM) and Cas9 protein (0.5 µM). This mixture was incubated at 37°C for 10 min.

3.3.5.3 Microinjection of ribonucleoproteins into one-cell stage embryos

Zebrafish eggs of the desired transgenic line were collected at the one cell stage, aligned on an agarose plate with indentations generated using microinjection molds (1% agarose in E3-medium) and injected with approx. 1 nL of the RNP solution using a microinjector. The solution was injected through the yolk sac directly into the cell. Embryos were reared as described before (see 3.3.2) and visually monitored for obvious toxicity of the RNP complex at 6 hpf and each subsequent day.

3.3.5.4 Analysis of gene targeting efficiencies

To determine successful gene editing, genomic DNA (gDNA) of individual animals was extracted of at least two days old embryos using the HotSHOT method as described earlier [94]. In brief, larvae were euthanized, 20 µL NaOH (50 mM) added and incubated in a thermocycler using the steps listed in Table 11. After completion, the solution was neutralized by adding 2 µL TRIS-buffer. Debris was pelleted using a table centrifuge and the supernatant including the gDNA was either directly used for further analysis or stored at 4°C.

Table 11 HotSHOT program.

Temperature	Ramp rate	Duration
90°C	1°C/s	10 min
4°C	0.1°C/s	-
4°C	-	hold

Polymerase chain reaction (PCR) was conducted to amplify the targeted region to assess gene editing efficiencies. Composition of the PCR reaction is shown in Table 12 and the program used in Table 13.

Table 12 Composition of PCR.

Compound	Volume/amount
Phusion High-Fidelity PCR Master Mix (2x)	12.5 µL
gDNA	1 µL
Forward primer	12.5 pmol
Reverse primer	12.5 pmol
MilliQ H_2O	ad 25 µL

Table 13 PCR program.

Cycle Step	Temperature	Time	Cycles
Initial denaturation	98°C	30 s	1
Denaturation	98°C	10 s	30
Annealing	61°C	10 s	
Extension	72°C	15 s	
Final extension	72°C	10 min	1
	4°C	hold	

After completion of the PCR, 1 µL unpurified product was sent for Sanger sequencing together with 10 µM primer (Microsynth AG, Balgach, Switzerland). To quantify gene editing, tracking of indels by decomposition (TIDE) analysis of the obtained sequences was performed (http://shinyapps.datacurators.nl/tide/) [95]. Here, all sequences were compared to a PCR product of one wt larva.

3.4 Fluorescent stereomicroscopy

The fluorescent stereomicroscope SteREO Discovery.V8 was used to acquire 8-bit images with a size of 1388 x 1040 pixel using the Axiovision software. Therefore, larvae were anesthetized (750 µM Tricain), placed on an agarose plate (0.5% agarose in E3-medium) and oriented laterally. Larvae were covered with sufficient E3-medium to keep them moist. For each larva, a bright field and fluorescent image was acquired with 8x magnification so that the whole CHT was in view. After completion, larvae were transferred to fresh E3-medium and further maintained.

3.4.1 Calculation of CTCF

To monitor engraftment of LCs after transplantation a commonly used method, which is normally applied to single cells, was adapted. Here, the corrected total CHT fluorescence (CTCF), which determines the level of fluorescence within the CHT, was calculated from fluorescence microscopy images as follows:

The brightfield image was used to draw a region of interest (ROI) of the CHT area. This ROI was applied to the fluorescent image. Using the 'Measure' function of ImageJ, the *area* of the ROI and the *mean fluorescent intensity* (MFI) was determined. For each larva, the integrated density was calculated. As a background level, the mean integrated density of ten untransplanted larvae was used. Ultimately, the CTCF was calculated for each individual transplanted larva. The following formulas were used:

$$\text{Integrated Density [RFU} * \mu m^2] = \text{ Mean Intensity CHT [RFU]} * \text{ CHT Area } [\mu m^2]$$

$$\text{CTCF [RFU} * \mu m^2] = (\text{Integrated Density}_{\text{ Transplanted}} - \text{ Integrated Density}_{\text{ Untransplanted}})\ [\text{RFU} * \mu m^2]$$

3.5 Confocal spinning disc microscopy

Confocal spinning disc microscopy is a technique for obtaining high-resolution optical images of biological objects labelled with fluorescent markers. For this study, two different confocal spinning disc microscopes were used: (i) the Yokogawa spinning disc setup controlled with the ZenBlue software, which was mainly used to analyze leukemia-niche interactions and (ii) the Andor Dragonfly system controlled with the Fusion software. The latter one was used for all cell tracking experiments. A Laser with an excitation wavelength of 488 nm was used to detect eGFP and CFSE. For mCherry detection, either a laser with an excitation wavelength of 587 nm (Yokogawa System) or 561 nm (Andor System) were used.

3.5.1 Embedding of zebrafish larvae

For *in vivo* live imaging larvae were anesthetized (750 µM Tricain) and transferred in a 4 Chamber 35 mm Glass bottom dish. Excess liquid was removed and 70 µL of pre-heated (50°C) 1.5% low melting agarose (MetaPhor™ Agarose) in E3-medium (750 µM Tricain) were added, larvae were rapidly orientated laterally to ensure that the whole CHT can be imaged. Once agarose solidified another layer of agarose was added to guarantee complete immobilization. Finally, approx. 500 µL E3-medium (750 µM Tricain) were added to avoid dehydration during imaging.

3.5.2 *In vivo* imaging

Embedded embryos (see 3.5.1) were placed under the spinning disc microscope with a breeding chamber pre-heated to 36°C. The CHT of individual larvae were imaged with a 20x air objective for a single time point or time lapse movies were generated. 16-bit images were recorded with a z-stack interval of maximum 4 µm, image sizes in x- and y-direction are indicated in Table 14 for the respective microscope. For time lapse records, larvae were imaged with defined intervals (e.g. 5 min) for up to 200 frames.

Table 14 Dimensions of the imaging systems.

Parameter	Yokogawa system	Dragonfly system
Size x-direction	1192 pixel	1024 pixel
Size y-direction	1040 pixel	1024 pixel
Pixel size	0.645 µm/pixel	0.603 µm/pixel

After completion of the measurement, larvae were gently liberated from agarose and either transferred in fresh E3-medium for later analysis or euthanized.

3.5.3 Image processing still frames

3.5.3.1 Two dimensional renderings

The ImageJ software was used to z-project the acquired multidimensional images by using maximal intensity projection. For visualization purpose, contrast enhancement was performed to get 0.1-0.3% saturated pixels. In a next step, images were rotated so that the main artery is horizontally orientated.

3.5.3.2 Three-dimensional surface renderings

Three-dimensional (3D) surface renderings were performed using Imaris software. For specific renderings, surfaces were visualized with transparency as indicated in the figure legend.

3.5.4 Image processing time lapse records

Scripted workflows were established to guarantee uniform and unbiased analysis of the multidimensional images using ImageJ software. In a first customized script, z-stacks were projected using maximal intensity projection and time lapse movies were corrected for any drift during the record by using the ‘Rigid Body’ transformation of the MultiStackReg Plugin. The channel that recorded endothelial cells was used to align the slices of the time series, as the vasculature does not massively change during the time course. This transformation was

applied to the stack of the LC channel. If endothelial cells were not fluorescently labeled, no drift stabilization was performed. Contrast enhancement was performed to get 0.1-0.3% saturated pixels. In a next step, a further customized script was applied; here, time stacks were rotated so that the main artery was horizontal orientated and cropped to only show the vessel bed of the CHT between the caudal artery (top) and caudal vein (bottom) for all time frames.

3.5.5 Cell tracking

LCs within the CHT of the processed time lapse records (see 3.5.4) were tracked using the ImageJ Plugin TrackMate [96] embedded in a script. Here, the movie was cut to a defined length and cells were detected using the 'LoG detector' with the following parameters: estimated blob diameter = 7 µm, threshold = 7, use median filter, do sub-pixel localization. The 'Hyperstack Displayer' was selected and spots were filtered by the mean intensity of the LCs (> approx. 800 RFU). Cells were tracked using the 'simple LAP tracker' with a maximal linking distance of 15 µm, no gap closing was allowed. The following three spreadsheets were generated and used for further analysis: spots_in_track_statistics, links_in_tracks_statistic, track_statistics.

3.5.6 Track analysis

3.5.6.1 Analysis of motion parameter

To analyze different motion parameters of the tracked cells within individual larva, the track_statistic file of each larva was used. This file listed all motion parameter of Table 15 for all tracks identified tracks.

Table 15 Parameter of track_statistic file.

Parameter
TRACK_DURATION
TRACK_DISPLACEMENT
TRACK_MEAN_SPEED
TOTAL_DISTANCE_TRAVELED
CONFINMENT_RATIO
LINEARITY_OF_FORWARD_PROGRESSION
MAX_DISTANCE_TRAVELED

Customized R-scripts were generated to extract the intended track parameter for a defined subset of tracks, for instance according to the track duration. The mean of each value of the respective parameter of one larva was considered as on data point.

3.5.6.2 Visualization of cell trajectories

To visualize individual tracks, so called rose-plots were generated. A customized R-script was generated to reconstruct the paths of all designated cells. Therefore, the parameters listed in Table 16 of the track_statistic file of each larva were used to calculated trajectories. The origin of all reconstructed trajectories were shifted to (0,0) to visualize extend of migration relative to a uniform starting point.

Table 16 Parameter of spots_in_track_statistics file.

Parameter
TRACK_ID
POSITION_X
POSITION_Y
FRAME

3.6 Flow cytometry

Flow cytometric analysis was performed using the BD LSRFortessa X-20 controlled with the BD FACSDiva™ Software. Laser and filter settings that were used for the respective fluorochrome detection are listed in Table 17. Data analysis was performed using FlowJo Software.

Table 17 Configurations of LSRFortessa X-20.

Laser	Excitation [nm]	Longpass filter	Bandpass filter	Parameter
Violet	405		405/50	mTagBFP, Fixable Viability Dye
Blue	488	505	530/30	eGFP, CFSE
Yellow-green	561	600	610/20	mCherry

3.6.1 Preparation of larvae

To analyze human LCs and zebrafish niche cells after transplantation by flow cytometry, cells of larvae were enzymatically individualized. Therefore, larvae were euthanized and cut with a sharp scalpel in two parts right after the yolk sac extension. Tails were collected, pooled as indicated, resuspended in 500 µl DPBS containing 25 µg Liberase and digested for 20-30 min at 37°C on a heat-block with rotating intervals: 30 s – 800 rpm; 60 s – 0 rpm. The suspension was filtered through a 30 µm mesh and cells were pelleted and washed in 500 µl DPBS once (200 g, 7 min, RT).

3.6.1.1 Detection of transplanted LCs

Fluorescently labeled LCs (eGFP, mCherry, mTagBFP, CFSE) were transplanted. At indicated time pointes, larvae were prepared for flow cytometric analysis (see 3.6.1) and the whole sample was measured.

First, debris was removed using FSC-A vs. SSC-A, followed by gating on singlets using FSC-H vs. FSC-W (Figure 4A). To retrieve LCs within the larvae, first, a fraction of the cultivated cells was measured and a gate was set to extract LCs using FSC-A vs. SSC-A (Figure 4B). Next, this gate was applied to all singlets of the larvae sample and all fluorophore labeled events were considered to be LCs (Figure 4A). These cells were either subjected to further fluorophore analysis to determine the CFSE signal intensity or the percentage of LCs in the caudal part of the larvae was calculated as follows:

$$\text{Proportion}_{\text{ LCs in caudal part}}\ (\%) = \frac{\text{count}_{\text{ fluorophore positive cells}}}{\text{count}_{\text{ all singlet cells}}} * 100$$

3.6.1.2 Detection of Macrophages

To analyze number of macrophages, LCs were transplanted into Tg(mpeg1:mCherry-F) larvae. At indicated time pointes, larvae were prepared for flow cytometric analysis (see 3.6.1) and the whole sample was measured.

Debris was removed using FSC-A vs. SSC-A, followed by gating on singlets using FSC-H vs. FSC-W. To determine numbers of macrophages, mCherry positive events upon all singlets were determined (Figure 4A). Wild type larvae show negligible numbers of mCherry positive events within the used gate (Figure 4C).

Percentage of macrophages in the caudal parts of the larvae were calculated as follows:

$$\text{Proportion}_{\text{ Macrophages in caudal part}}\ (\%) = \frac{\text{count}_{\text{ mCherry positive singlet cells}}}{\text{count}_{\text{ all singlet cells}}} * 100$$

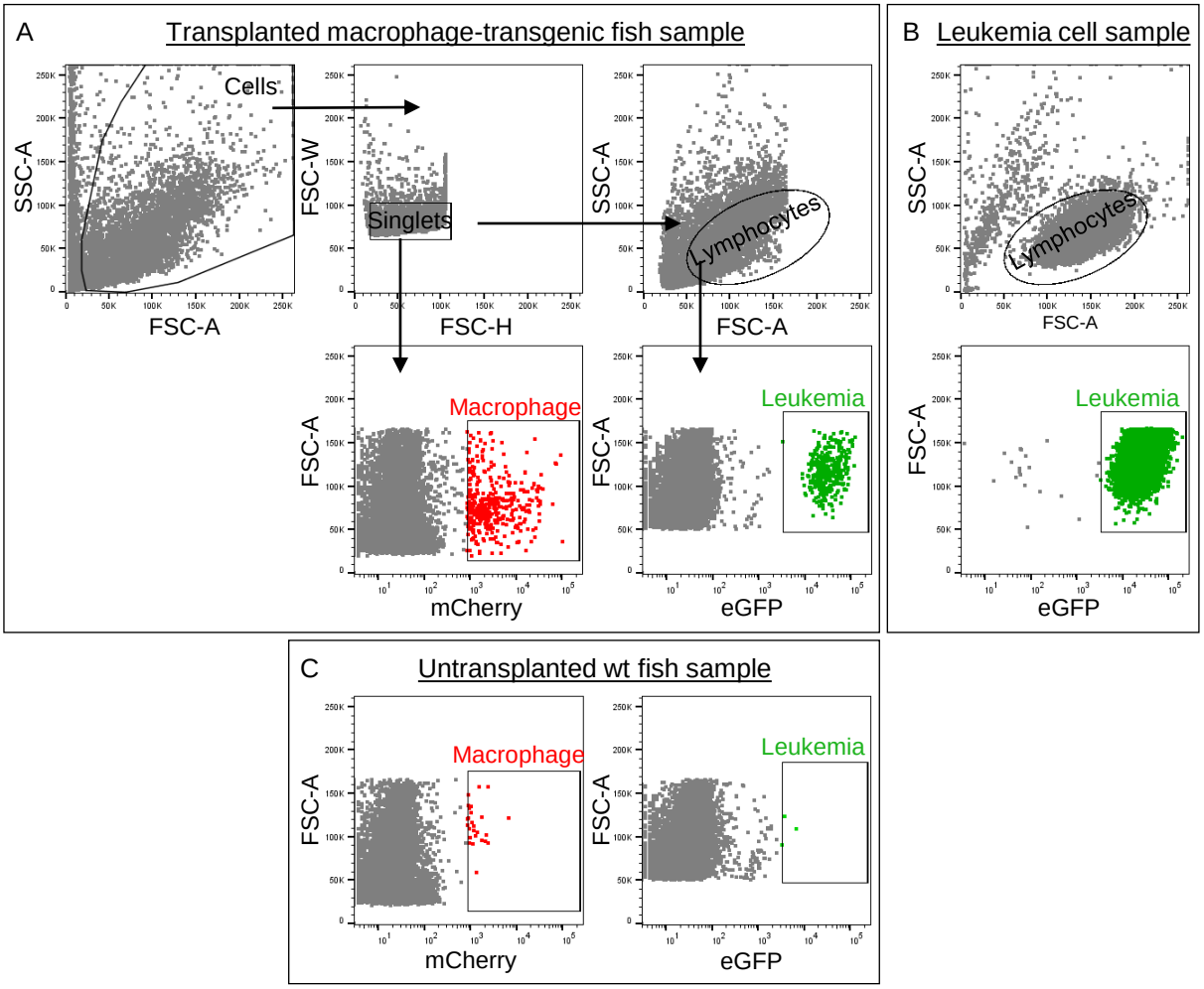

Figure 4 Exemplary gating for quantification of LCs and macrophages of larvae.
(A) 'Cells' were selected using FSC-A/SSC-A. 'Singlets' were gated using FSC-H/FSC-W. mCherry positive 'macrophages' were selected by gating on mCherry positive events using mCherry/FSC-A. 'Leukemia cells' were detected by applying the 'lymphocytes gate that was drawn using a leukemia cell sample (see (B)) on the singlets gate (FSC-A/SSC-A). Next, events that were positive for the fluorescent marker (here: eGFP) were considered as leukemia cells by eGFP/FSC-A. **(B)** Exemplary gates of the pure LC sample. **(C)** Exemplary plots of untransplanted wt larvae sample.

3.6.2 Viability analysis of primary cells

To assess viability of primary cells during *in vitro* culture, a small fraction of the cells at the respective time point was pelleted and resuspended in DPBS containing the Fixable Viability Dye eFluor 450 (1 µL/mL). Cells were incubated for 5 min at RT protected from light. Next, cells were washed once with DPBS (300 g, 5 min, RT) and analyzed by flow cytometry. Viable cells were negative for the dye (Figure 5).

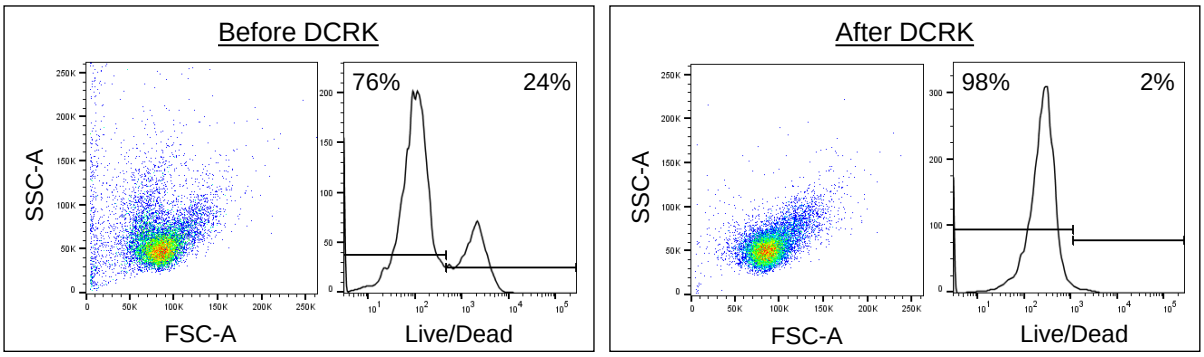

Figure 5 Exemplary gating for quantification of viable primary cells before and after DCRK.
Exemplary plots of one analyzed primary sample before and after DCRK. All measured events were plotted using FSC-A/SSC-A (left) and analyzed for staining with the viability dye (right). Viable cells were dye negative while dead cells were positive for the dye.

3.7 Single cell transcriptome analysis

3.7.1 Sample preparation and sequencing

Cryopreserved BM aspirates were thawed (see 3.2.4.1), CFSE stained (see 3.2.5), cultured (see 3.2.4.2), enriched for living cells (see 3.2.6) and methanol fixed (see 3.2.7) before processing for transcriptomic analysis.

Single cell transcriptome analysis was performed by the laboratory of Bradley Blaser (Ohio State University, Columbus, OH, USA) using the 10x Genomics Chromium System. Cell rehydration was performed using published methods [97]; single cells were isolated and barcoded expression libraries were generated using the Single Cell 3' v3 kit according to the manufacturer's instructions. Targeted recovery was 4,000 cells per sample. Sequencing was performed on an Illumina Novaseq 6000 and more than 20,000 reads per cell were obtained. Sequencing data were pre-processed using Cell Ranger v3.1. Low quality cells and doublets were identified and removed using *scater* [98] and *doubletfinder* [99], respectively. All cells passing quality control were included in the analysis unless otherwise indicated.

3.7.2 Visualization of gene expression

Dimension reduction and visualization was performed using custom single cell analysis tools (https://github.com/blaserlab/blaseRtools) based on functions found in *monocle3* [100]. For UMAP projection, datasets from both samples were merged and UMAP coordinates of all individual cells were calculated and plotted [101]. Partitions were assigned after manual inspection of the top specific genes in each partition. Gene module analysis was used to identify groups of co-regulated genes across individual cells [102]. Expression of individual

genes of interest was plotted as an overlay on the initially generated UMAP. Analysis was conducted by the Blaser Lab.

3.7.3 Differential gene expression

Differential gene expression between patient-12 (ER-sample) and patient-17 (NR-sample), was calculated between the LCs of the two samples (exclusion of T-cells and red blood cells (RBC)) using regression analysis. Calculation was performed by the Blaser Lab.

Significantly dysregulated genes were defined with the following two cut-offs: q-value < 0.05 and estimate >1.5 or < -1.5. These genes were subjected to Core Analysis (Expression Analysis) of Ingenuity Pathway Analysis (IPA) to identify dysregulated functions between the two samples. Here, the estimate value of each gene was used as Expr Fold Change to estimate directionality of the functions. Functions with a z-score below -2 or above 2, were considered to be significantly down- or up-regulated in the ER-sample, respectively. Genes that were assigned to the respective function of interest were extracted and further investigated.

3.7.4 Co-expression analysis

Unsupervised clustering was performed using the “Louvain” method to identify subpopulations of leukemic cells in both samples [103]. A panel of genes of interest was selected from those that were significantly upregulated in either the NR or the ER patient according to our regression analysis. An aggregate expression value was calculated for each cell cluster with respect to each gene of interest using size-factor-corrected, log-transformed gene counts. A Pearson Correlation matrix was then calculated from aggregate expression values for each gene. Analysis was conducted by the Blaser Lab.

3.7.5 Software availability

A precompiled R data package containing processed data files is available at https://datadryad.org/stash/share/Lx9XPx-4KXG5Wqdvx9lbZTOj-I5-2VS9jkBmIN78MQQ.
Data processing scripts are available at https://github.com/blaserlab/arner.binder.datapkg and final analysis scripts are available at https://github.com/blaserlab/arner_binder. All analysis was performed using R v4.1.

3.8 Calculation of niche anchoring score

To grade the analyzed migratory parameter (see 3.5.6.1) for each individual patient and to summarize the observation in one anchoring score, the following calculations were performed. First, the mean value of the analyzed parameter (e.g. velocity) was calculated for each patient. Next, the sub-score for the respective patient was calculated according to this formula:

$$Subscore = 10 - (Reference_{Value} - Min_{Value}) * \frac{10}{Max_{Value} - Min_{Value}}$$

For the summary score, all five calculated sub-scores (velocity, maximal (max.) distance traveled, displacement, confinement ratio, mean straight line speed) were summed up. For the final score the mean value of all five sub-scores was calculated. A high score represents strong niche anchoring, while a low score indicates less anchoring.

3.9 Statistics

All statistical analysis was performed using GraphPad Prism™ 7 or R v4.1. The statistical tests used in specific experiments are provided in the respected figure legend. Levels of significance were depicted with asterisks as follows: $p \leq 0.05$: *, $p \leq 0.01$: **. In case no significant difference was observed, the abbreviation ns was used.

4 RESULTS

For children with ALL, relapse development implies a poor prognosis [11]. A better understanding of the mechanisms that lead to relapse is important in order to improve risk stratification at the time of diagnosis and to develop novel therapies.

Most studies investigate LCs independent from their surrounding tissue. Model systems that consider the microenvironment are rare. Commonly, the analysis of LCs in the context of a functional microenvironment is performed with *in vitro* co-culture experiments where LCs are cultured in the presence of typically only one other cell type [104, 105]. Mostly, the addition of expensive cytokines and growth factors is necessary to ensure cell viability and to mimic the niche to some extent [106]. Apart from that, mouse models are used, which represent an appropriate environment, but are very costly and tedious and therefore only small numbers of animals can be analyzed [77]. The zebrafish is an emerging animal model in cancer research. Studies show an adequate conservation of the zebrafish hematopoietic niche to study human LCs in a reasonable complex microenvironment, resembling human bone marrow [43, 44]. However, a zebrafish model to study leukemia-niche interactions was not described so far.

4.1 Establishment of the larval xenotransplantation model of ALL

During the past two decades, xenotransplantation models of diverse cancer entities into zebrafish embryos have been described [57, 58, 62, 63, 67]. These references were used as a basis to establish the BCP-ALL xenograft model for my project.

As is customary in the field of larval xenotransplantation, cell injections were performed at a developmental stage of 48 hpf [107]. To study LCs in an orthotopic manner within the CHT, which is the proper hematopoietic niche at this stage of development (see 1.2.1), 200-500 cells were injected into the common cardinal vein (CCV). The CCV, also known as the duct of Cuvier, is a large vessel, dorsal of the yolk sac where blood of the head and trunk comes together and dispenses on both sides of the yolk sac to the sinus venosus (SV) of the heart. Upon transplantation, cells get distributed with the blood flow throughout the whole body and can find their proper niche (Figure 6). The CHT is a well perfused vessel bed with different niche cells e.g. endothelial cells, macrophages and stroma cells [46]. Henceforth, in this study, the term ‘niche’ will refer to all cells present in the tissue between the CA and CV in the caudal part of the fish. In order to perform microscopy based approaches, the optically transparent strain ‘Casper’ (roy$^{-/-}$, nacre$^{-/-}$), which lacks melanocytes and iridophores, was used [42]. In case ‘Casper’ fish were not available, larvae were treated with PTU to ensure transparency. Given the differential body temperatures of humans and fish of 37°C and 28.5°C, respectively,

it is important to compromise between the temperatures to not harm fish development but to support cancer cell proliferation and engraftment. For the present study, adequate development of the larvae is important when analyzing niche components of the fish. Consequently, transplanted larvae were raised at 36°C, as this temperature allows larvae to develop normally and human cells to survive and proliferate [59]. Only morphologically normal developed individuals were used for the analysis.

To retrieve LCs upon transplantation, using flow cytometry and microscopy approaches, cells were previously either lentivirally transduced to express a fluorescent protein (mTagBFP, eGFP, mCherry) (transgenic human cells were provided by the laboratory of Irmela Jeremias, Helmholtz Zentrum, Munich, Germany) or stained using the fluorescent dye CFSE.

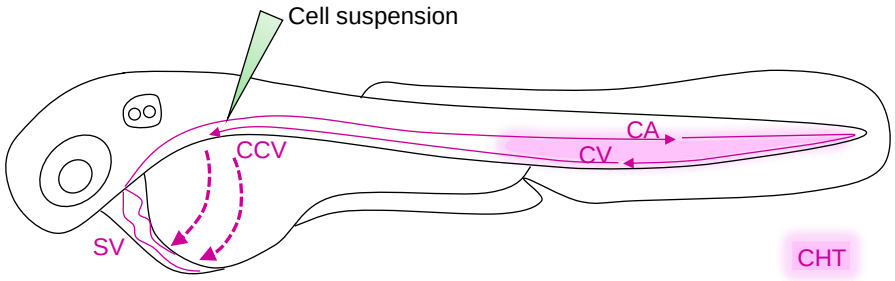

Figure 6 Schematic illustration of a zebrafish larvae at 48 hpf.
Cell suspension of LCs was injected via the common cardinal veil (CCV) where cells were taken along with the blood flow. Upon passing the sinus venosus (SV) of the heart, cells were quickly distributed throughout the whole body. The CHT is delimited by the caudal artery (CA) and caudal vein (CV).

4.1.1 LCs survived within the CHT after transplantation

In a first step, the xenotransplantation assay was performed to assess dissemination of LCs in larvae after injection into the blood flow.

The BCP-ALL cell line NALM-6, which was transgenic for eGFP, was transplanted. Larvae were anesthetized and the caudal parts were imaged using a fluorescence stereomicroscope to monitor LCs at one and three days post injection (dpi). A specific fluorescent signal of NALM-6 cells was detected in transplanted larvae, which was absent in untransplanted larvae. NALM-6 cells homed to the proper hematopoietic niche at this time point, the CHT, where they resided during the three days of follow up time (Figure 7).

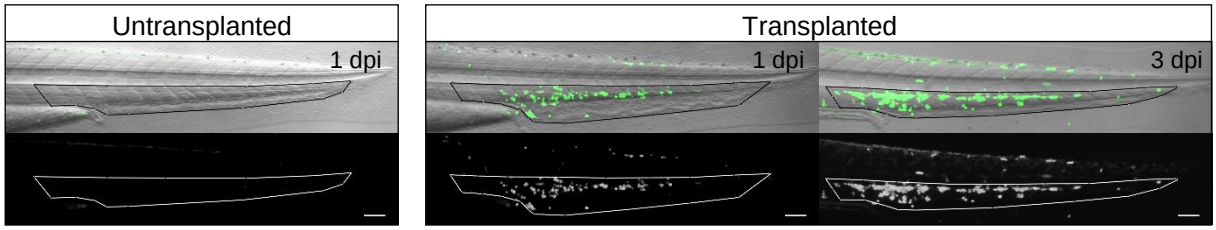

Figure 7 LCs homed to the CHT area and survived for at least three days.
Representative fluorescent (lower panel) and brightfield (merge, upper panel) images of the caudal part of a untransplanted larva (left) and a transplanted larva (NALM-6) (right), at 1 and 3 dpi. The outline of the niche area is highlighted and was used to assess the CTCF of transplanted larvae (see 3.4.1). Scale bar 100 µm.

This targeted colonizing of the niche area indicated that zebrafish cytokines, chemokines and growth factors were sufficient to guide the human LCs to the hematopoietic niche and hold them there, after xenotransplantation.

4.1.2 LCs engrafted and proliferated

The images of the transplanted larvae in Figure 7 already suggested an increase of the fluorescent signal within the marked niche area of the representative larva within two days. This rise could indicate that more LCs homed to the niche over time, but possibly also that cells proliferated. To better characterize LC engraftment, a set of experiments was performed and this process was analyzed in more detail.

In a first step, LCs were quantified over time in order to monitor colonization of the niche. Transplanted larvae were analyzed using *in vivo* microscopy. This non-invasive method allowed the analysis of the same animal at different time points. The MFI of the eGFP signal, normalized to the CHT area was determined for transplanted and untransplanted larvae. Subtracting the average value of untransplanted larva from the transplanted larva gave the CTCF, representing the leukemic burden within the niche. For ten transplanted larvae, CTCF was calculated at one and three dpi. On average, the CTCF significantly increased by 68% within 48 h. When looking at single larva, the strongest observed increase showed a triplication while only for one larva, the leukemic burden decreased (Figure 8).

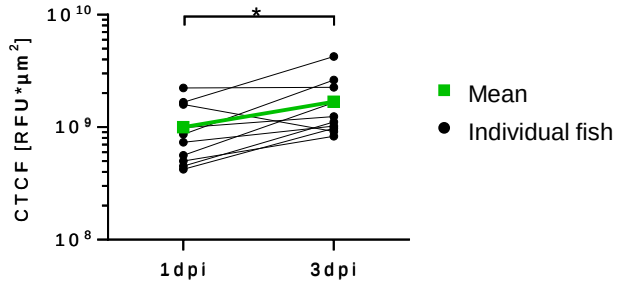

Figure 8 *In vivo* imaging showed an increase in leukemic burden over time.
Repetitive measurement of the CTCF of 10 larvae at 1 and 3 dpi. Each point represents one larva. Lines connect individual larvae at both time points. Mean value of all larvae is indicated in green (n=10, Wilcoxon matched-pairs signed rank test, * p≤0.05).

In addition, a flow cytometric approach was established to detect LCs of transplanted larvae. Using flow cytometry, relative numbers of fluorescent NALM-6 cells can be determined. To assess sensitivity of the assay, different numbers of NALM-6 cells were transplanted. For 50 larvae, the CTCF was calculated at one dpi. Larvae were divided up into groups of ten (group A-E), according to the CTCF, prior to analyzing the caudal parts of the 10 larvae as one sample using flow cytometry (Figure 9A). Group A included larvae with the highest CTCF (~3 x10^9 RFU*µm^2) while for group E, larvae with the lowest CTCF were pooled (~5 x10^7 RFU*µm^2) (Figure 9B). Representative dot plots of the flow cytometric analysis depicted higher numbers of NALM-6 cells in group A than in group C. As expected, for untransplanted larvae no eGFP positive events were detected (Figure 9C). As fluorescent intensity of eGFP+ cells was very homogeneous in the flow cytometry analysis (Figure 9C), the increased fluorescent intensity of the images over time (Figure 8) was most likely due to an increased cell number and not to higher eGFP expression of some cells. Furthermore, the correlation of imaging and flow cytometry for all five groups showed that both methods correlated linearly, as an increased fluorescent signal of the imaging analysis resulted in an increased number of detected cells as determined by using flow cytometry (Figure 9D). Hence, both assays could equally be used to monitor engraftment of LCs at different time points.

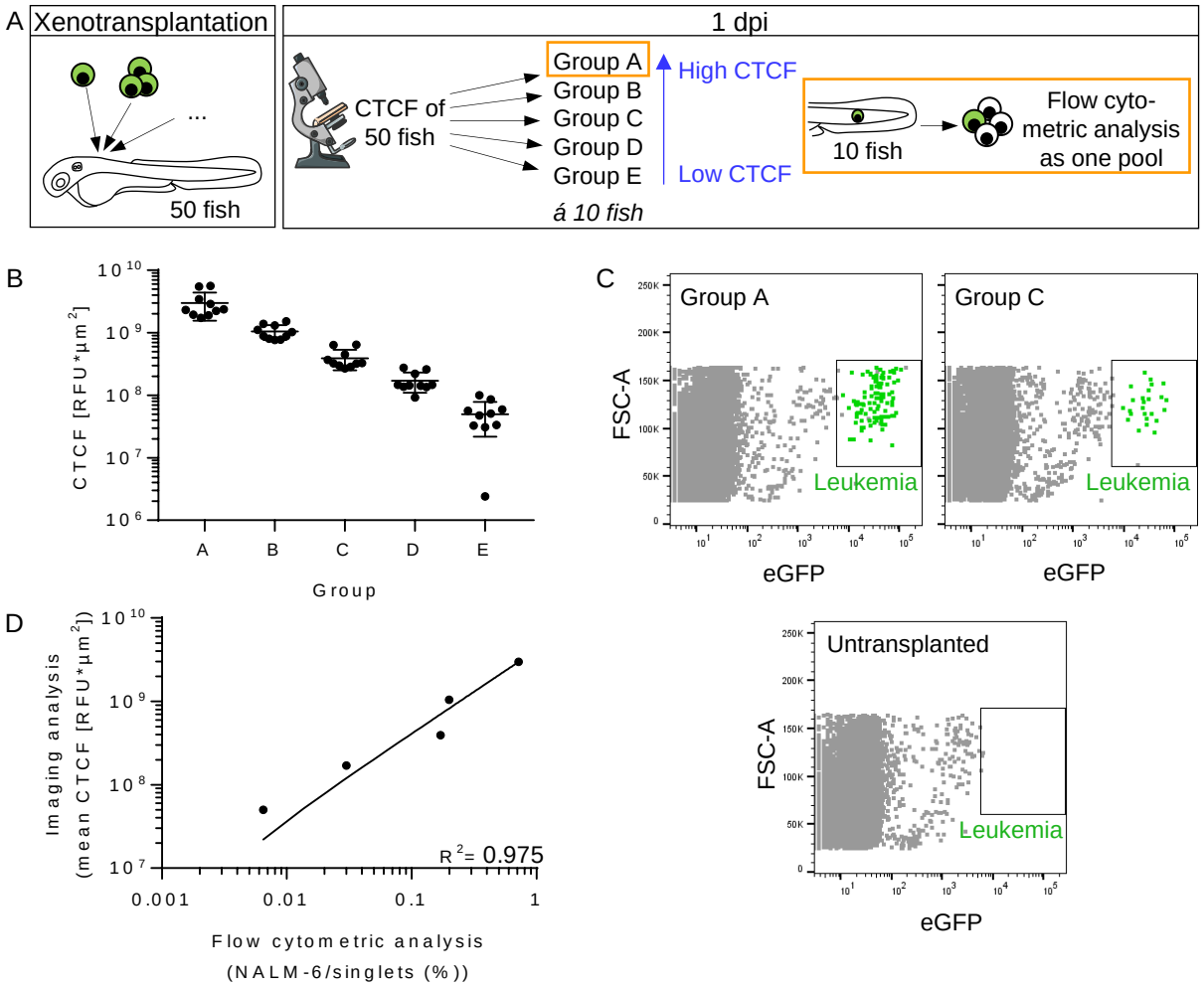

Figure 9 *In vivo* imaging and flow cytometry analysis correlated linearly.
(A) Experimental setup: Larvae were transplanted with NALM-6 cells (eGFP+). At 1 dpi CTCF was calculated and larvae were grouped into groups of 10 according to the values obtained. Larvae of each group were pooled and measured as one sample using flow cytometry. **(B)** Grouping of the 50 analyzed larvae at 1 dpi with corresponding CTCF. Scatter-plot displays the calculated CTCF value per larva and mean value ± SEM per group. **(C)** Dot plot of the flow cytometry measurement of two representative transplanted samples (group A and C) and an untransplanted sample. Gray dots show cells in singlets gate; green dots show NALM-6 cells. For detailed gating see 3.6.1.1. **(D)** Correlation of the flow cytometric analysis and imaging analysis. One dot represents one group (for imaging analysis, mean value of the 10 larvae in (B) is depicted, for flow cytometric analysis, the result of the pooled sample is depicted). Correlation curve and R^2 was calculated with linear regression.

To determine whether LCs also proliferate *in vivo* or if more LCs colonize the niche over time, a cell proliferation assay was performed. Here, mCherry expressing NALM-6 cells were labeled with the fluorescent proliferation sensitive dye CFSE, which covalently binds to proteins of the cells. Upon cell divisions, cells with halved CFSE signal can be detected using flow cytometry. Groups of transplanted larvae were sacrificed at one, two and three dpi and mCherry positive NALM-6 cells were identified and the CFSE intensity of the cells was analyzed.

The histogram of NALM-6 cells in Figure 10A shows the CFSE signal of all transplanted LCs at different time points. Importantly, over time, defined populations with halved CFSE-signal appeared, representing cells that underwent cell division (Figure 10A). As the present work

aimed at applying the model for transplantations of primary LCs, next, PDX cells were transplanted since they were biologically closer to patient material. MTagBFP expressing PDX cells, were generated using the mouse model of the laboratory of Irmela Jeremias (Helmholtz Zentrum, Munich, Germany) and supplied by her group. Strikingly, histograms of the PDX cells of two different ALL patients (ALL-199, ALL-265) showed reduced CFSE intensities when analyzing the LCs at different time points (Figure 10A). Quantifying the MFI of the three different transplanted leukemia samples over time showed that NALM-6 cells proliferated faster than the two analyzed PDX cells (Figure 10B). ALL-199 and ALL-265 showed similar proliferation rates. Comparing the MFI of LCs *in vivo* and *in vitro* showed similar kinetics. Interestingly, ALL-199 showed slightly increased proliferation under *in vivo* conditions when compared to *in vitro* conditions. On average, xenografted PDX cells divided twice within three days, however, histograms show that some cells underwent up to three cell divisions. For NALM-6 cells, the number of average cell divisions was four, while the maximum within three days, was five divisions.

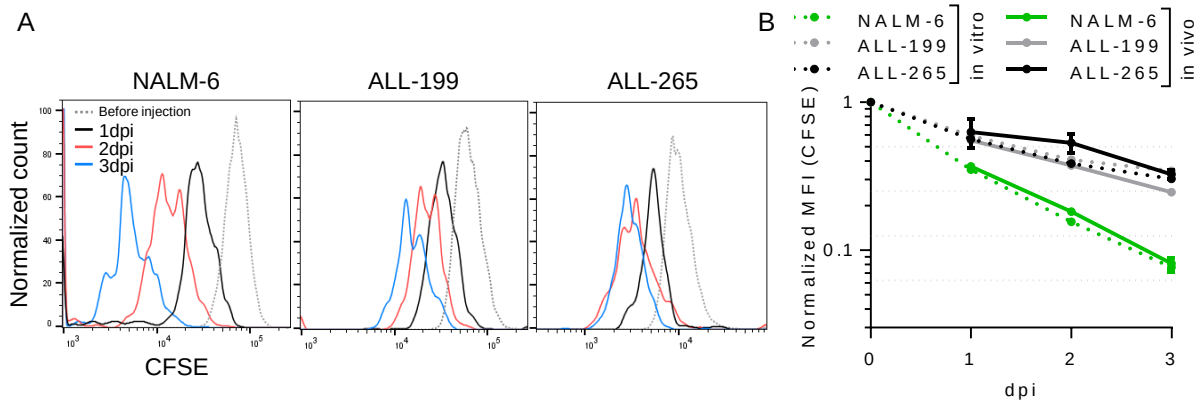

Figure 10 Proliferation of human LCs *in vivo*.
(A) Representative histograms of the CFSE signal of different transplanted LCs at daily measurements of 10 pooled larvae are depicted. **(B)** Quantification of the normalized MFI of the CFSE signal over time (*in vivo* samples: n=3 (NALM-6: mean value of three independent experiments performed in duplicates; ALL-199 & ALL-265: values of one experiment performed in triplicates), mean value ± SEM; *in vitro* samples: NALM-6: n=3 values of three independent experiments; ALL-199 & ALL-265: n=1 value of one measurement in one experiment)

In addition, *in vivo* time lapse shots of confocal microscopy clearly confirmed a cell division of a NALM-6 cell within the vasculature of a zebrafish at 15.5 hours post injection (hpi). After cell division the two daughter cells remained at the site of division (Figure 11A). 3D surface rendering confirmed the presence of only one cell at the beginning and excluded one cell being behind the other (Figure 11B). Cell divisions of ALL-199 and ALL-265 were observed as well (data not shown).

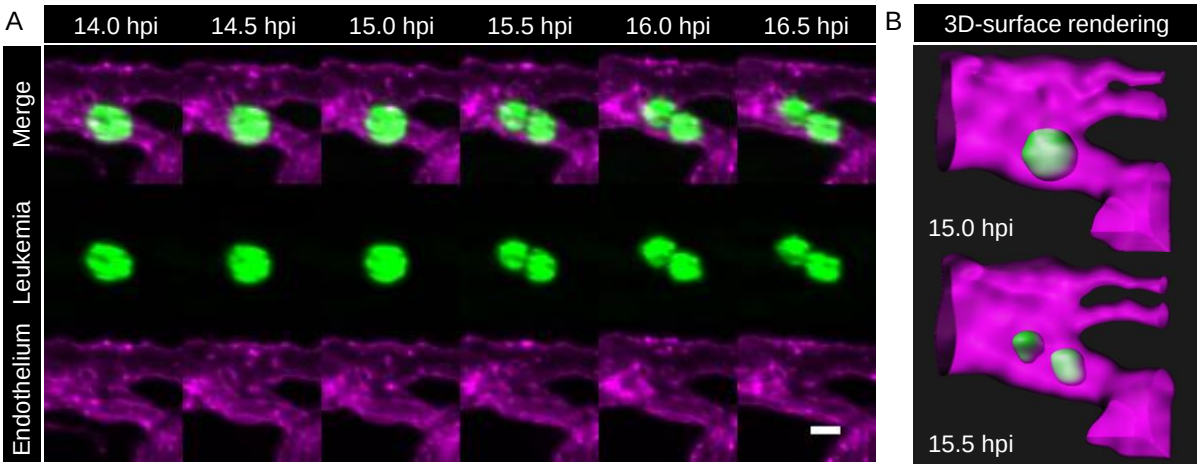

Figure 11 Leukemia cell divided in a vessel.
(A) Six frames of a time lapse video between 14 and 16.5 hpi with a frame interval of 30 min are depicted. Upper row shows the merged image of eGFP+ NALM-6 cells (green, middle row) and kdrl:mCherry endothelial cells (magenta, lower row). These images illustrate a NALM-6 cell located in a vessel for an extended period of time. Between 15 and 15.5 hpi the NALM-6 cell divided. Scale bar 10 µm. **(B)** 3D-surface renderings. Surface of endothelial cells is visualized with transparency.

Taken together, this set of experiments demonstrated the successful establishment of larval zebrafish xenografts of human LC lines and, importantly, also PDX cells. The LCs can be transplanted and homed to the expected niche compartment, the CHT. There, cells resided within the monitored time frame of three days and the tumor burden increased over time. More cells could have homed and colonized the CHT over time, but as cells underwent several cell divisions, this increase is mostly due to proliferation.

4.2 Interaction of LCs with niche cells in the CHT area

To further characterize the established model with regard to the microenvironment, the interplay of LCs and two different niche cells was analyzed. As this model was established with the aim to monitor LCs in an environment that should mimic the human bone marrow, it is particularly interesting to examine where LCs reside with respect to surrounding niche cells and if LCs are in contact with them. So far, there is no description of xenotransplanted LCs interacting with host niche cells. There are different reporter fish lines available with fluorescently labeled niche cells that enable co-visualization of LCs and niche cells *in vivo* in a spatio-temporal manner.

4.2.1 LCs were in contact with macrophages

Macrophages belong to cellular elements of the innate immune system and are highly interesting niche cells to study as they are known to play diverse rolls in malignant diseases.

Generally, two different activation states are described, an immune-stimulating and therefore anti-tumor (M1) and an immune-suppressive and therefore pro-tumor (M2) state [34]. In zebrafish embryos, macrophages are present as early as 24 hpf [61] and can be nicely monitored in transgenic larvae expressing the fluorescent protein mCherry specifically in macrophages (Tg(mpeg1:mCherry-F)).

In a first step, the relative frequencies and distribution patterns of macrophages within the niche were examined for transplanted and untransplanted zebrafish larvae. NALM-6 cells (eGFP+) were transplanted into Tg(mpeg1:mCherry-F) zebrafish larvae. At one dpi, transplanted larvae and untransplanted siblings were anesthetized and the caudal parts were imaged using confocal microscopy. Representative images showed that macrophages were found throughout the caudal part of the larval body but were mainly localized in the CHT. This was similar for transplanted and transplanted larva (Figure 12). Notably, some macrophages and NALM-6 cells were in close proximity to each other.

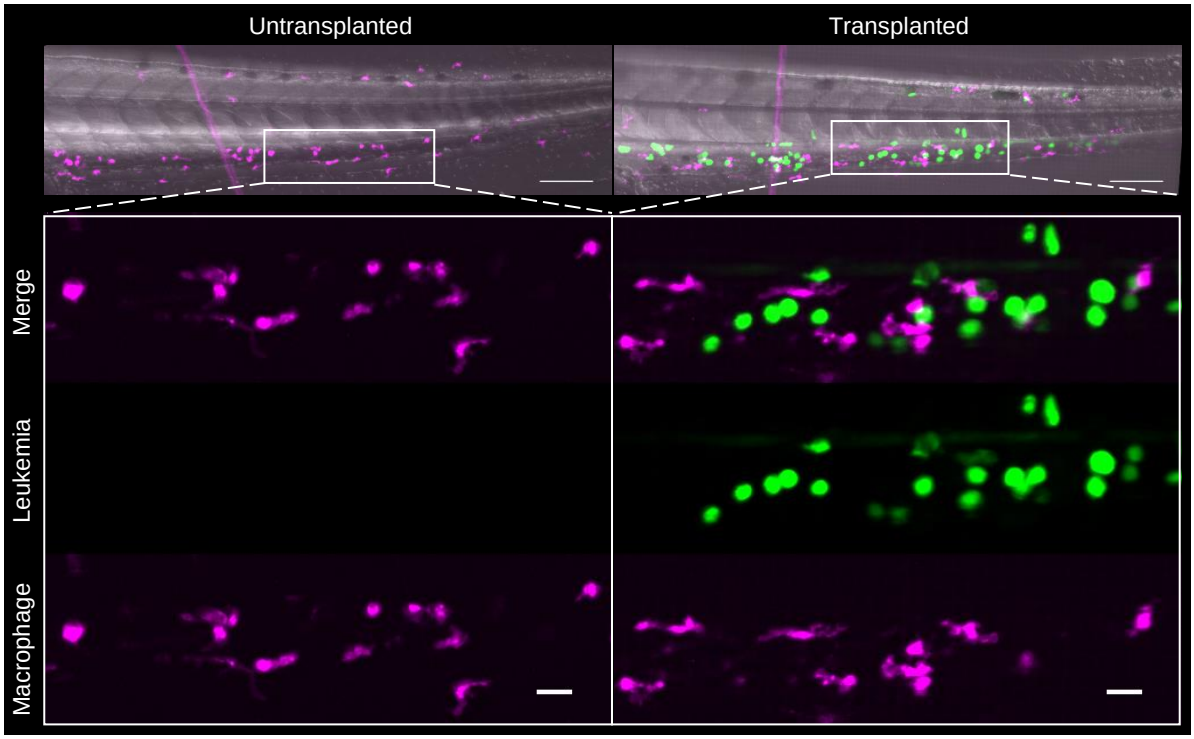

Figure 12 Macrophages were prominent niche cells.
On the top, representative overview images of the caudal parts of an untransplanted (left) and a transplanted larva (right) at 1 dpi are depicted. Scale bar 100 µm. Upper panels of the zoomed sections depict merged image of eGFP+ NALM-6 cells (green, middle row) and mpeg1:mCherry-F macrophages (magenta, lower row). Scale bar 20 µm.

4.2.1.1 LCs interacted for an extended period

Since still frames of transplanted larvae showed spatial vicinity of macrophages and LCs, spatio-temporal confocal microscopy was conducted for several hours to monitor LCs and macrophages at the same time.

Tg(mpeg1:mCherry-F) larvae were transplanted with NALM-6 cells (eGFP+). At indicated time points post transplantation, larvae were anesthetized, embedded and imaged. The recorded time-lapse movies visualized that macrophages as well as LCs were highly mobile within the CHT. Despite high mobility of both cell types, for some LCs extended periods of close interaction with macrophages were observed, while other LCs had no direct contact with surrounding macrophages. In Figure 13A, one representative interaction was documented, which lasted for more than 10 h. At the start of the interaction (0 min) it was visible that the macrophage forms two pseudopodial extensions that reach the LC. At 240 min and 360 min, it is visible how the macrophage embraced the LC during the interaction. 3D-surface renderings support the observations (Figure 13A). In Figure 13B, a shorter lasting interaction is depicted. The LC was very stationary during the interaction while the macrophage arrived rapidly and within 15 min it embraced the LC. However, after 45 min the contact ended and the macrophage migrated away from the LC. Again 3D-surface renderings confirm the contact (Figure 13B).

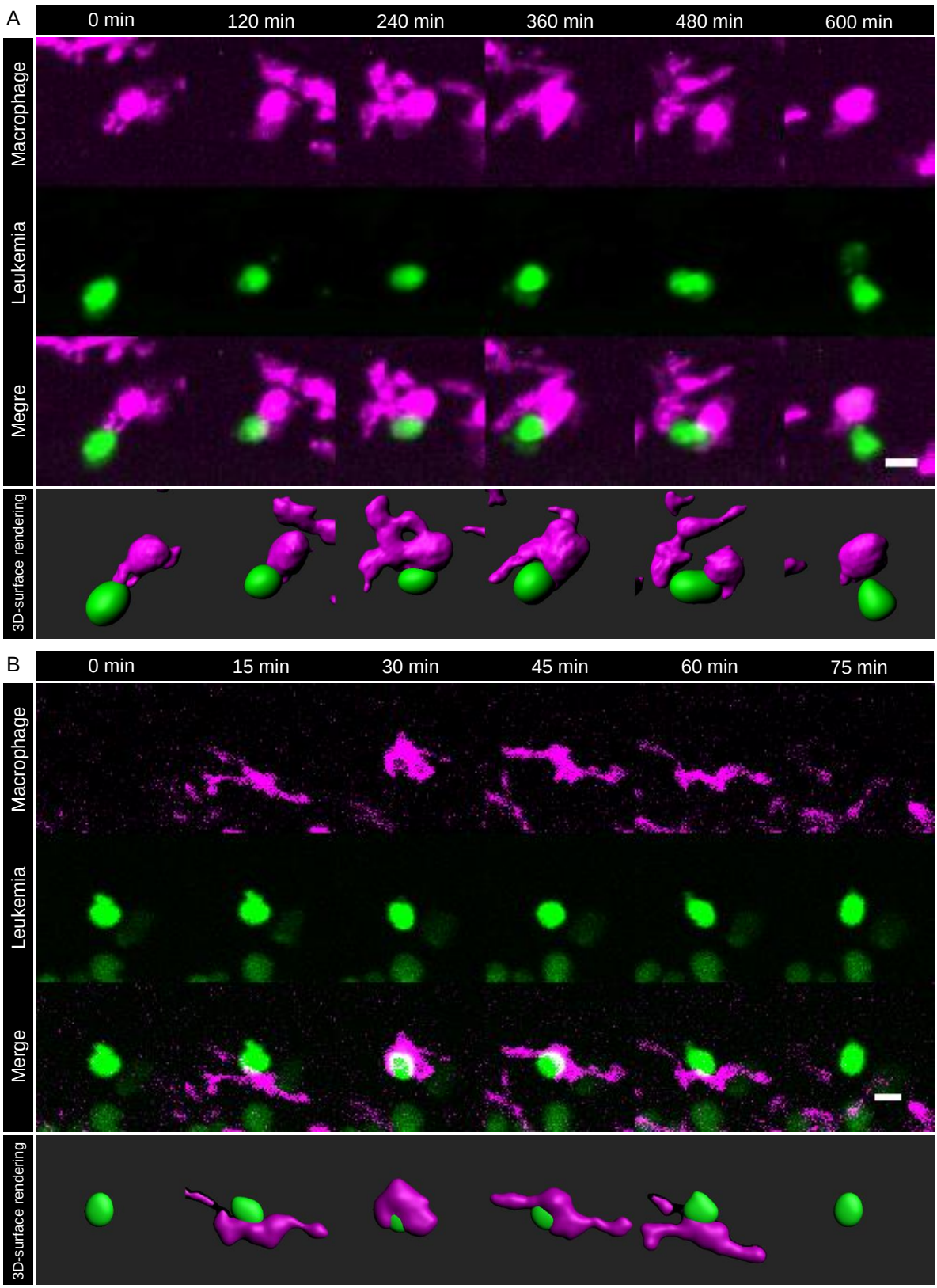

Figure 13 Persisting interactions of macrophages and leukemia cells.
(A, B) Six still frames of a time lapse movie are depicted. Images show a eGFP+ NALM-6 cell (green, upper row) and one macrophage mpeg1:mCherry-F (magenta, middle row) closely interacting. Lower row shows the merged image. Scale bar 10 µm. Separate panel below shows 3D-surface renderings. Selected frames of the movie are depicted **(A)** Time lapse movie starting at 31 hpi with a frame interval of 20 min was recorded**. (B)** Time lapse movie starting at 35 hpi with a frame interval of 5 min was recorded.

4.2.1.2 LCs could be phagocytized

As close interactions of LCs and macrophages were observed, and macrophages occasionally embraced the LC, the question arose whether zebrafish macrophages are able to phagocytize the human LCs or if they were simply not able due to inter-species incompatibilities.

Hence, time lapse movies of transplanted larvae were revised to specifically look for phagocytosis events. In Figure 14, one representative phagocytosis event of one LC by a macrophage is depicted. First, the LC and one macrophage got into contact. Two minutes later, the macrophage began to surround the LC. Already 6 min after close contact, the LC was completely phagocytized by the macrophage. 3D-surface renderings clearly depict this process. Here, surfaces of macrophages were pictured with transparency to emphasize that the LC is enclosed inside the macrophage (Figure 14). Notably, LC and macrophage co-localized only shortly before the phagocytosis event (data not shown).

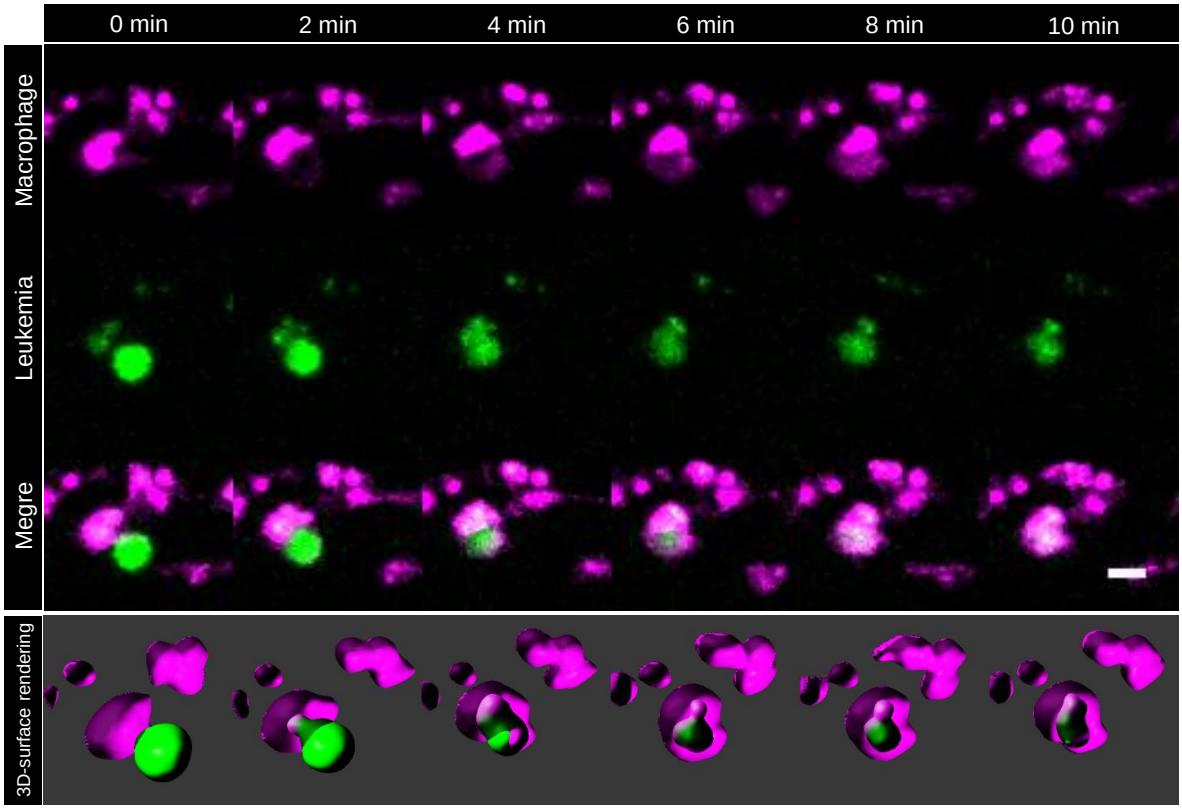

Figure 14 Phagocytosis of a LC.
Six still frames of a time lapse movie starting at 23 hpi with a frame interval of 2 min are depicted. Images show a CFSE labeled primary LC (green, upper row) and one macrophage mpeg1:mCherry-F (magenta, middle row) during a phagocytosis event. Lower row shows the merged image. Scale bar 10 µm. Separate panel below shows 3D-surface renderings. For macrophages, surface is visualized with transparency to emphasize engulfed LC.

Taken together, this demonstrated that LC elimination via phagocytosis by macrophage in general is possible in the xenotransplantation setting. However, close contact between LCs and macrophages without elimination of the LC was observed.

4.2.1.3 No enhanced infiltration or phagocytosis activity of macrophages

After observing intensive contact between LCs and macrophages, the question arose whether more macrophages were recruited to the CHT of transplanted larvae when compared to untransplanted control siblings.

Tg(mpeg1:mCherry-F) larvae were transplanted with NALM-6 cells (eGFP+). Groups of ten larvae, either untransplanted (control (Ctrl)) or transplanted, were sacrificed at three dpi and the caudal parts were subjected to flow cytometric analysis (Figure 15A). Proportions of macrophages among all singlets within the CHT were analyzed and compared between transplanted and Ctrl larvae. Here, the amount of macrophages in larvae transplanted with LCs was similar to Ctrl larvae (Figure 15B). To assess, whether differences in leukemic burden influenced the number of macrophages in the CHT, the percentage of NALM-6 cells was correlated to the amount of macrophages. This showed no clear connection as the correlation coefficient r was low and R^2 was close to 0 (Figure 15C). In a next step, the MFI of all macrophages in the respective sample was calculated as a measurement of phagocytosis activity. In case a macrophage engulfed a NALM-6 cell, the cells' fluorescence can be detected as demonstrated using confocal microscopy (Figure 14). Here, no increased eGFP signal was detected for the macrophages of transplanted larvae when compared to Ctrl siblings (Figure 15D).

Taken together, macrophages were in contact with LCs as persisting interactions were observed. In addition, zebrafish macrophages pursued their host defending function as they phagocytized some malignant LCs. Overall, no increased infiltration or phagocytosis activity within the niche was observed. In conclusion, this set of experiments supports the suitability of the present larval zebrafish xenograft model to study leukemia in a functional and complex surrounding tissue.

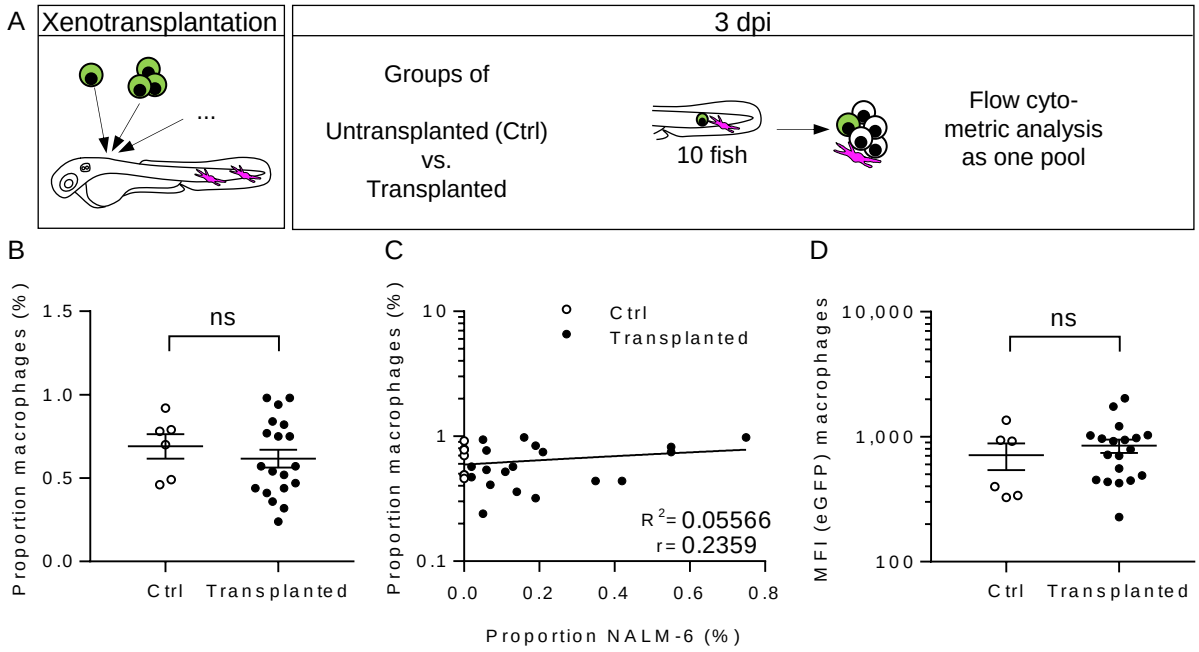

Figure 15 No enhanced infiltration or phagocytosis activity of macrophages.
(A) Experimental setup: Tg(mpeg1:mCherry-F) larvae were transplanted with NALM-6 cells (eGFP+). At 3 dpi untransplanted (Ctrl) and transplanted larvae were grouped into groups of 10 and measured as one sample using flow cytometry. **(B, C, D)** Each point of the plots represents a group of ten larvae measured as one sample out of three independent experiments. (untransplanted: n=6; transplanted: n=19). For gating see 3.6.1.1 and 3.6.1.2. **(B)** Quantification of the percentage of macrophages within singlets was assessed. **(C)** Point plot of the correlation of the percentage of macrophages and NALM-6 cells. Correlation curve was calculated using linear-regression (r=0.2359, R^2=0.056). **(D)** Quantification of the eGFP MFI of all detected macrophages. Each point of the scatter-plot represents the MFI of all macrophages within the sample. (B, D) Mean value ± SEM is depicted. (unpaired t-test with Welch's correction, ns not significant).

4.2.2 LCs left the vasculature and formed clusters

Endothelial cells represent the putatively most prominent cell type within the CHT. This tissue can generally be considered as a very well perfused plexus and is delimited with the CA and the CV [46]. Analyzing LCs location with respect to the vasculature is highly interesting, as endothelial cell mediated niche interactions have been observed before [32].

The distribution of LCs within the niche was analyzed in larvae expressing the fluorescent protein mCherry specifically in endothelial cell (Tg(kdrl:mCherry)). On consecutive days after transplantation of NALM-6 cells (eGFP+), larvae were anesthetized and the CHT was imaged and analyzed using confocal microscopy. At one dpi, LCs were evenly distributed throughout the niche (Figure 16A). Physiologically, at two dpi distinct non-vascularized pockets emerged in the CHT, ventral of the CA. These pockets were colonized with many LCs that formed clusters. At three dpi, LCs were almost exclusively found extraluminal (Figure 16B). This observation demonstrated that LCs were able to extravasate the endothelium. Extravasation is a complex process, since it requires signaling between extravasating cells and the endothelium [108]. Strikingly, this specific behavior of LCs was not exclusively observed for

NALM-6 cells (Figure 16), as ALL-199 and ALL-265 and some primary samples showed the same specific behavior (data not shown). This suggests a specific process, confirming the functional signaling between host niche cells and human LCs.

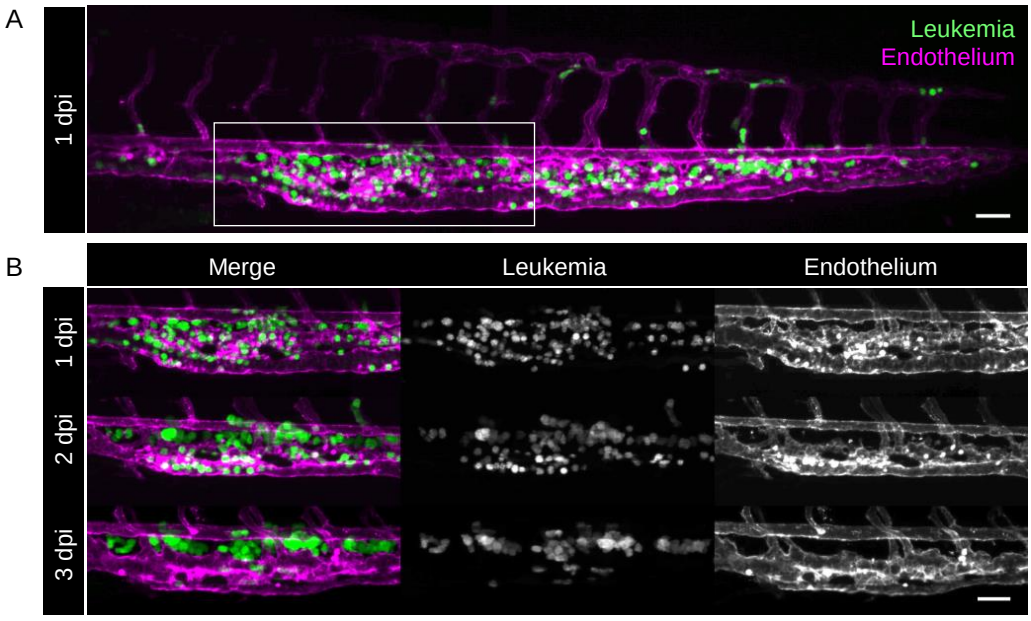

Figure 16 Extravasation and cluster formation of LCs.
Confocal microscopy of one representative transplanted Tg(kdrl:mCherry) larva over the course of three days is depicted. **(A)** Complete caudal part of the larva at 1 dpi. Marked area indicates field of view of (B). Scale bar 50 µm. **(B)** Section of the CHT at three consecutive days. Left panel shows merged images of NALM-6 (green, middle panel) and the endothelium (kdrl:mCherry) (magenta, right panel). Scale bar 50 µm.

Taken together, diverse interactions of different zebrafish niche cells and LCs were observed. Macrophages closely interacted for an extended period of time, despite the possibility to phagocytize them. Similar distribution patterns of LCs within the vasculature were monitored for a number of different LCs indicating a specific behavior, highlighting the expediency of the established model.

4.2.3 Analyzing LC migration and adhesion

The overall aim of this project was to identify cellular features of LCs that might play a role in relapse development of children with ALL. We hypothesized that LCs that later caused relapse interact more effectively with niche cells. To address the hypothesis, a method was developed that allowed the analysis of adhesion and migration of LCs as a measured value of niche interaction. One of the main advantages of the larval zebrafish model is the opportunity to monitor cells in the living organism in real-time for an extended period of time using confocal *in vivo* microscopy. Hence, a proof of principle experiment was performed to establish the microscopy based assay.

Strong shear and hemodynamic forces push LCs throughout the vessels. To interact with niche cells, LCs need to slow down. Specific adhesion molecules of the endothelium, such as E-selectin (CD62E) are known to play a role in the retention of leukocytes and LCs within the vasculature [109, 110]. The functional domains of E-selectin are highly conserved between humans and zebrafish [87]. Thus, E-selectin represents a highly suitable target to perform a loss of function experiment. Upon loss of E-selectin, LCs were expected to be retained less effective within the niche when compared to niches with functional E-selectin.

4.2.3.1 Generation of E-selectin knockout larvae

In order to perform the above described proof of principle experiment, E-selectin KO animals had to be generated. As zebrafish embryos develop outside the mother, they are available for genetic manipulation already at the single cell stage and KO animals can be generated using CRISPR/Cas9-technology [111]. When applying functional analysis to larvae of the mutagenized generation (G0), a few things need to be considered. To achieve a full KO animal, (i) the genetic change has to occur before the first cell division, (ii) on both alleles and (iii) the editing has to result in a complete loss of function mutation of the targeted protein. In zebrafish, this critical cell division takes place at around 40-45 min after fertilization. In case the mutation occurs at a later time point, this leads to a larva with a mixture of cells, some are still harboring the wild type (wt) gene while in some cells the targeted gene is mutated. The extent of mutated cells therefore depends on the developmental stage gene editing takes place. For instance, gene editing of both alleles in one of the two cells at the 2-cell stage will result in larva with 50% mutated cells, while editing in one cell at the 128-cell stage will result in a larva with less than 1% mutated cells (Figure 17A). Even though, the genetic manipulations occur at an early developmental stage, mosaic animals are generated resulting in multiple different mutations among the mutated cells. Each DNA double stand breaks (DSB) is repaired independently resulting in different insertions and deletions (indels) and thereby desired mutations. Hence, larvae with a genetic mosaicism for the targeted gene are generated in G0 (Figure 17B).

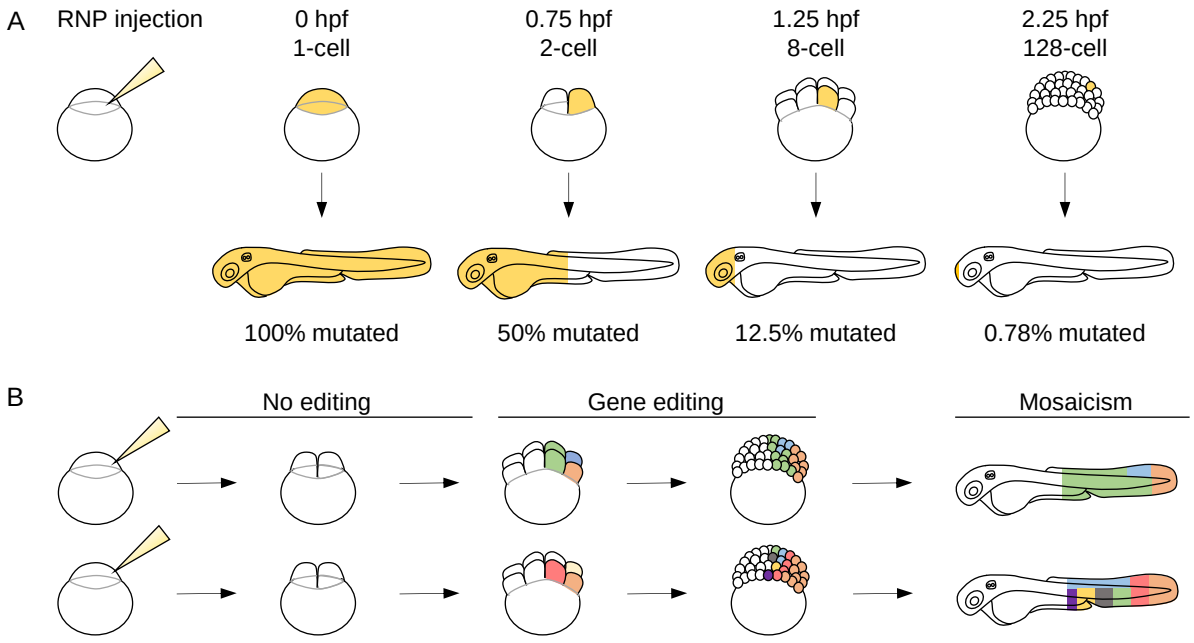

Figure 17 Illustration of CRISPR/Cas9 efficiencies in G0.
(A) Assembled RNP complex is injected into the first cell. Gene editing is visualized in yellow. If gene editing happened during the 1-cell stage, completely mutated larvae develop. With the gene editing occurring later, the extent of mutated cells decreases. **(B)** Gene editing occurs independently in each cell, leading to larvae with diverse gene variants (indicated with different colors) (= Mosaicism). Earlier gene editing leads to reduced mosaicism.

In the present study, E-selectin KO-larvae were generated using RNPs targeting the zebrafish E-selectin gene (*sele*). Two different crRNA sequences were designed that targeted different regions of the *sele* gene. RNPs were assembled by annealing the specific crRNAs with a tracrRNA resulting in a gRNA, which was then combined with Cas9 protein. These complexes were injected separately into the first cell of fertilized eggs (Tg(kdrl:mCherry)). To evaluate KO-efficiencies of the two different crRNAs, genomic DNA (gDNA) of individual larva was extracted and an approx. 700 bp long fragment, including the targeted region, was PCR amplified and sequenced. Aligning the sequences of RNP injected larva to the sequence of a wt larva showed that for injected larva the sequence trace did not map after the expected cutting site, three base pairs upstream of the PAM (Figure 18A), due to indels. To quantify KO-efficiencies of the two different crRNAs and determine, which of the two has better KO-efficiencies, TIDE analysis was performed. As expected and explained above, different values of KO-efficiencies were obtained. On average, crRNA_1 had a KO-efficiency of 13%, whereas crRNA_2 reached 38%. None of the crRNA_1 injected larvae exceeded 20% (Figure 18B), while for crRNA_2, several larvae with a KO-efficiency of > 40% were generated. Consequently, for all further experiments, crRNA_2 was used.

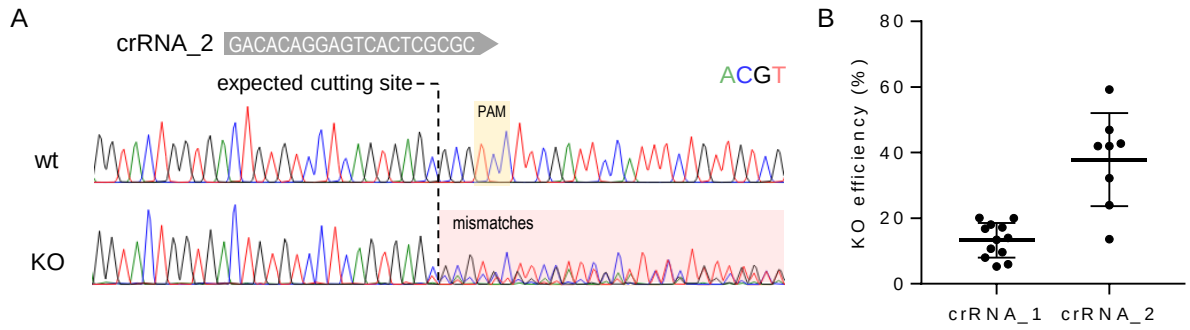

Figure 18 Generation of E-selectin KO-larvae.
(A) Alignment of the wt sequence and a representative sequence for a KO larva (crRNA_2). Sequence of the crRNA_2, PAM site, expected break site and mismatching region are indicated. **(B)** Scatter-plot of RNP injected larva with two different crRNAs. Each dot represents one larva out of two independent experiments (crRNA_1: n=12; crRNA_2 n=8). Mean value ± SEM is indicated.

Taken together, by injecting RNPs at the 1-cell stage of larvae, unique individuals with partially mutated E-selectin are generated in G0 with KO-efficiencies reaching above 40%. These mutated larvae can be subjected to functional analysis.

4.2.3.2 A semi-automated workflow to analyze cell adhesion and migration

To study motility of LCs after transplantation, multidimensional time-lapse movies were generated using confocal microscopy and a workflow was established to analyze the cellular motion of LCs. In order to process the large datasets unbiased and straightforward, a semi-automated workflow was established to extract detailed information on cellular movement.

In a first step, a customized script for the image processing program ImageJ was generated to pre-process the time-lapse movies. Here, the 3D images were projected in z-direction and the drift that occurred during the time course of the movie was stabilized. Despite 3D imaging (x, y, z) of the vessel bed, cells were tracked in two dimensions (x, y), as z-direction of the CHT is relatively thin (~25 µm) compared to x- and y-direction of the field of view (~600 µm and 100 µm, respectively) With this simplification, results were only marginally changed. Next, LCs were detected and tracked for the time course of the movie using the ImageJ Plugin TrackMate [96], embedded in a further customized script (Figure 19). To increase the likelihood that one track comprised exclusively the same cell, the max. distance of the spots within two frames was limited. The two-fold length of the cell diameter seemed to be a reasonable distance to guarantee keeping track of the same cell. Given that LCs have a diameter of ~8 µm, the max. distance was set to 15 µm. However, with this restriction, loosing oversight of few very fast moving cells was accepted as the main interest was given to cells that were in contact with the surrounding tissue and thereby moving relatively slow.

The dataset with detailed tracking information for all cells was subjected to further analysis. Here, R based scripts were generated to automatically and uniformly analyze the datasets to

get information on the cell movement-parameter of interest. For instance, tracks can be analyzed according to their duration as a measured value of LC residence time within the niche.

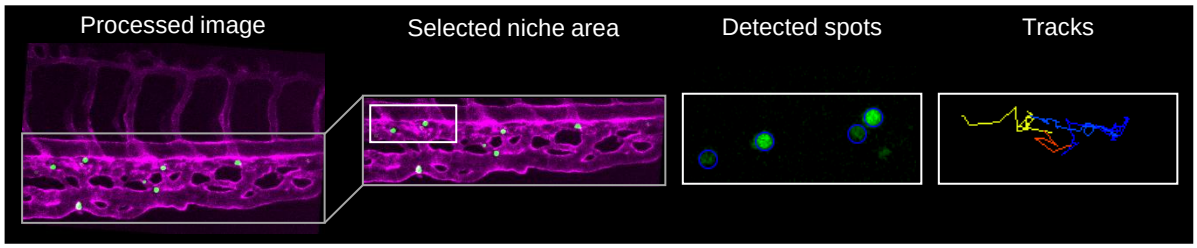

Figure 19 Image processing for cell tracking.
Multidimensional time-lapse movies were processed including z-projection, drift stabilization and cropping of the niche area (gray selection) (for details see 3.5.4). Next, cells were tracked using the ImageJ Plugin TrackMate [96]. Cells were automatically detected as spots and tracked for the duration of the movie. For each track numerous parameter were collected (for details see 3.5.5).

In order to determine robustness of the established semi-automated workflow, three independent experiments of NALM-6 cells were performed with the established analysis pipeline. NALM-6 cells were transplanted at 48 hpf. Three hpi larvae were anesthetized and immobilized in agarose. Time lapse movies of the niche were recorded for a duration of 250 min with a frame interval of 5 min and tracking statistics were calculated. All cells that were in the niche for at least 30 min were used for further analysis. Comparing the mean value of the replicates did not show any significant differences of all analyzed parameter. For all replicates, track duration was ~90 min, whereof ~70% were longer than 50 min and had a velocity of ~0.4 µm/min (Figure 20).

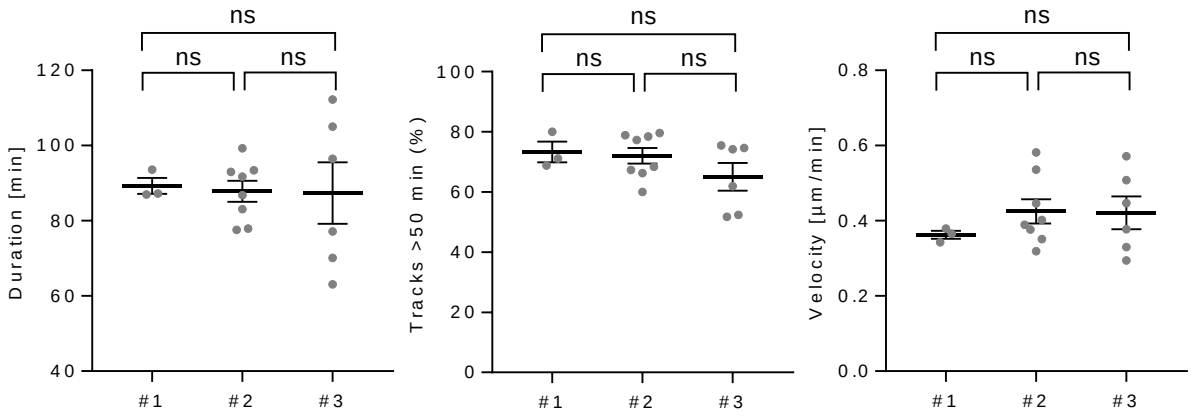

Figure 20 The established semi-automated workflow allowed robust cell tracking.
Analysis of representative tracking parameter of three independent replicates (#1, #2 and #3). Each dot of the scatter-plot represents one larva within one experiment (#1: n=3, #2: n=8 and #3: n=6). Mean value ± SEM is depicted. Kruskal-Wallis-Test was conducted to examine the differences between three independent experiment. For all parameter, no significant (ns) differences were found.

Taken together, the established approach allowed the rapid, uniform analysis of LC motility of individual cells within the niche area to study dynamics and behavioral patterns. Repeated measurements demonstrated the robustness and reproducibility of the established assay.

4.2.3.3 LCs and endothelial cells interacted via E-selectin

With the robust performance of the established analysis pipeline, next, the sensitivity of the assay was evaluated. Therefore, LC motility upon E-selectin KO was assessed and compared to xenografts in control larvae.

Eggs at the 1-cell stage of Tg(kdrl:mCherry) fish were injected with a RNP targeting E-selectin or a control RNP, which was built using a nt crRNA. At 48 hpf, NALM-6 cells (eGFP+) were transplanted into the RNP-injected larvae. After two hours, transplanted larvae were anesthetized and embedded for confocal microscopy. Time lapse movies of the niche were recorded for a duration of 250 min with a frame interval of 5 min. After completion of the movie, gDNA of each individual larva was extracted and the KO-efficiency was determined. Only larvae with mutated E-selectin were analyzed, while larvae with insufficient editing were excluded from the analysis.

Quantification of the KO-efficiency showed that for this experiment, the highest KO-efficiency that was achieved reached 47%, while for some larvae, the KO-efficiency was lower than 1%. Three groups were defined according to their KO-efficiencies. A KO-efficiency of below 5% was considered as no KO, and above 20% as high KO. All values in-between were defined as intermediate (interm) KO (Figure 21A). On average, 50% of all RNP injected larvae showed a KO-efficiency >5% and half of them reached a high KO-efficiency of above 20% (Figure 21B). For further functional analysis, all larvae that reached a KO-efficiency of above 5% were included.

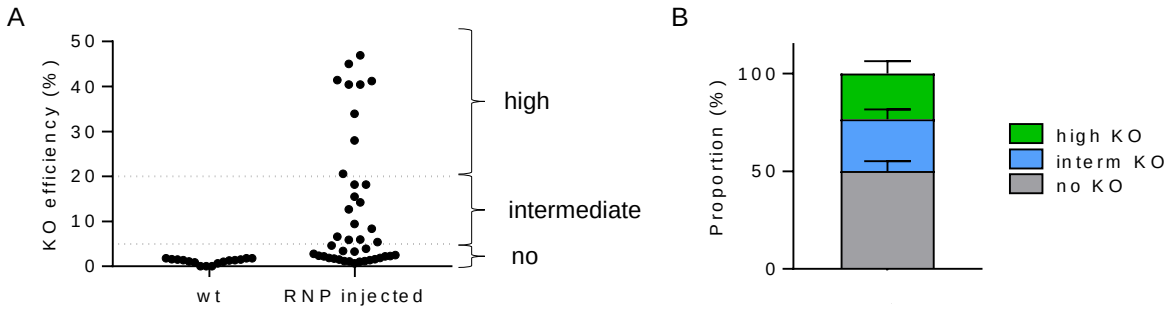

Figure 21 Distribution of E-Selectin KO-efficiencies.
(A) Scatter-plot of wt (n=16) and RNP injected larvae (crRNA_2) (n=41). Each dot represents one larva out of three independent experiments. Thresholds for grouping are indicated with dashed lines. KO-efficiency <5%: no KO (n=21); KO-efficiency >5% & <20%: interm KO (n=11) and KO-efficiency >20%: high KO (n=9). **(B)** Stacked bar depicting the frequencies of larvae with high, interm and no KO among all RNP injected larvae out of three independent experiments. Mean value +SEM is indicated.

To compare the retention of NALM-6 cells within larvae with mutated E-selectin, first, the mean residence time of all cells that were in the niche for at least 10 min was analyzed for each larva. Cells in KO-larvae were in the niche for an average time of 66 min while cells that were transplanted into nt-larvae, resided in the niche for 70 min. Hence, E-selectin KO led to a slightly reduced residence time (Figure 22A). For each larva, a high number of cells was tracked, but most probably, E-selectin was mutated in only a part of the niche due to mosaicism and KO-efficiencies not exceeding 50%. Next, the percentage of cells that resided for a rather short duration (< 50 min), was analyzed. Here, for KO-larvae, on average 60% of the LCs were within the niche shorter than 50 min, while for nt-larvae it were significantly fewer (55%) (Figure 22B). For all cells that were within the niche for at least 50 min, the velocity was analyzed to assess whether there is a difference in their retention. The velocity of LCs in KO-larvae was 16% faster than of cells in nt-larvae, indicating reduced adhesion. Importantly, embryos injected with a RNP targeting E-selectin, but not reaching a KO-efficiency of above 5%, behaved like the nt control (data not shown).

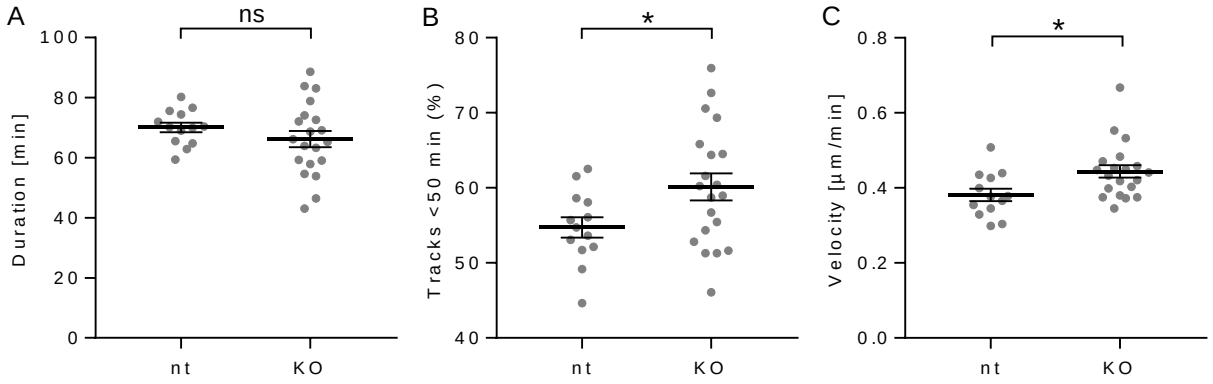

Figure 22 E-selectin KO diminished LC retention within the niche.
(A) Scatter-plot of the mean duration of all tracks that lasted for more than 10 min within one larva were analyzed. **(B)** Scatter-plot of the percentage of tracks that lasted shorter than 50 min within one larva. **(C)** Scatter-plot of the velocity of all track that were shorter than 50 min within one larva. **(A, B, C**) Each point of the scatter-plot represents one KO-larva out of three independent experiments, for nt control, three different crRNAs were used in one experiment. (nt: n=13; KO n=20) Mean value ± SEM is depicted. (unpaired t-test with Welch's correction, ns not significant, * p≤0.05).

Taken together, this experiment demonstrated the successful establishment of a quantitative assay that allowed the analysis of LC motility within the niche. The proof of principle experiment of E-selectin KO highlights, on the one hand that it is possible to quantify LC migration and on the other hand suggests that critical adhesion molecules, such as E-selectin are sufficiently conserved to hold human NALM-6 cells within the niche of larval zebrafish. In summary, this confirms the suitability of our zebrafish xenograft model to study leukemia in the context of a complex microenvironment.

4.3 Migration behavior of primary pediatric BCP-ALL cells in the CHT area

The established model allowed transplantations of LCs and showed interactions with the surrounding tissue. In addition, a pipeline was established whereby LC migration can be analyzed robustly and with high sensitivity.

In a next step, these approaches were applied to address the hypothesis that LCs that later caused relapse, interact more efficient with niche cells. Therefore, suitable patients were selected and their LCs were transplanted, followed by a comparative detailed analysis of the migration patterns.

4.3.1 Patient selection

To conduct the study in a translational model, we aimed at working with primary patient material. At the Dr. von Haunersches Kinderspital of the LMU in Munich a collection of more than 1,000 biopsies of various types of leukemia at different disease stages are cryopreserved. Importantly, for this study, treatment naïve material of the BM aspirations of the initial diagnosis were selected, as we aimed to identify features that were present at time of diagnosis. In case no BM material was available, peripheral blood was used. For almost all patients, detailed information on the clinical course was available. Two groups of patients with BCP- ALL, with different clinical outcome, were defined. For one group, children with no documented relapse within at least five years of follow-up time were selected (= no relapse (NR)). For the other group, children that suffered from a very early (≤ 18 months from diagnosis) or early (> 18 and ≤ 30 months from diagnosis) relapse were identified (= very early or early relapse (ER)) [14]. Table 18 and Table 19 summarize clinical data of all NR-patients and ER-patients used for this study, respectively.

Table 18 Primary B-cell precursor ALL with clinical data and characteristics – no relapse samples.

ID	Initial risk stratification	Sex	Age at diagnosis [years]	Leukocyte count [cells/µL]	Cytogenetics
01	High	m	3.9	25,000	Normal
04	High	m	5.1	25,000	ETV6-RUNX1, deletion 9p
06	High	f	9.2	137,000	Hyper-diploid
10	High	f	5.7	109,000	ETV6-RUNX1, hyper-diploid
15	High	m	8.6	-	ETV6-RUNX1
17	Low	f	5.3	-	ETV6-RUNX1

Table 19 Primary B-cell precursor ALL with clinical data and characteristics – relapse samples.

ID	Time to relapse [months]	Initial risk stratification	Sex	Age at diagnosis [years]	Leukocyte count [cells/µL]	Cytogenetics	Additional Information
02	31	Low	f	8.7	8,500	ETV6-RUNX1	One relapse
03	15	High	m	12.5	220,000	Complex aberrant	Multiple relapses Deceased
05	16	High	f	11.5	49,500	Deletion 12p	Late responder Multiple relapses Deceased
12	16	High	f	8.5	40,000	Monosomy 9, hyper-diploid	One Relapse Transplant
14	18	-	f	1.8	-	-	-

4.3.2 Preparation of primary patient material

Working with primary, cryopreserved LCs is rather complex as these cells are difficult to cultivate and require optimized conditions. The recovery and transplantation of viable cells was essential for the present study. All samples were stored for several years, and variable cell viability after thawing was observed. In order to recover a high number of viable cells for transplantation, a robust protocol for cell preparation was established, comprising gentle cell thawing, fluorescent cell labeling and cell culture before transplant to allow them to recover. In addition, emerging dead cells were removed shortly before transplantation (Figure 23A).

To detect transplanted cells using fluorescent microscopy, cells had to be fluorescently labeled after thawing. The non-toxic fluorescent labeling dye CFSE was used, which passively diffuses into cells and binds covalently to proteins in the cytoplasm. Therefore, it is highly suitable to label cells directly after thawing and label them uniformly for several days. To ensure specific detection of the patient material and to prevent unspecific transfer of unbound CFSE to fish tissue, cells were kept *in vitro* overnight before getting transplanted. During this time, not bound CFSE gets transferred out of the cell. To guarantee best culturing conditions and recovery of the cells, they were kept in StemSpan™ SFEM medium, which was specifically developed for hematopoietic stem and progenitor cell. After approx. 16 h, dead cells were removed using magnetic bead based depletion and transplanted into zebrafish embryos. This protocol was successfully applied to most of the cryopreserved samples and ensured transplantation of highly viable cells.

To monitor cell viability of all primary samples during the different stages of the *in vitro* culture, cell viability was determined using flow cytometry. A fraction of the cells was stained using a cell viability dye that penetrates the cell membrane of dead cells and is excluded by living cells. At d-1, viability was measured after thawing and showed on average 81% viable cells. After

16 h of *in vitro* culture, viability dropped to a mean of 60%. For five samples, less than 50% viable cells were recovered. Upon application of the DCRK, viability reached on average 90%, however, for two of the samples with low viability, too few cells were recovered to quantify viability before transplantation. Still, sufficient cell numbers for transplantation were recovered (Figure 23B).

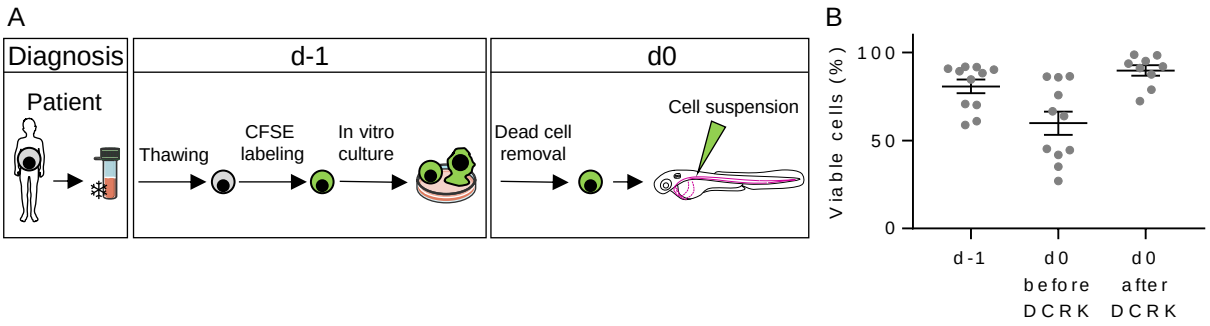

Figure 23 Preparation of primary material.
(A) Workflow for cell preparation of cryopreserved primary patient material. At d-1 cells were thawed, labeled with CFSE and kept in culture overnight. At d0, dead cells were removed and highly viable cells were transplanted. **(B)** Quantification of the cell viability at different time points was assessed using flow cytometry. Each point represents one patient sample (d-1 & d0 before DCRK n=11; d0 after DCRK n=9). Mean value ± SEM is depicted.

Taken together, a protocol for preparation of primary patient samples was established, which provided sufficient viability for successful transplantation into larvae in order to perform functional assays.

4.3.3 Tracking of ALL cells in the niche

All eleven primary patient samples were prepared (see 4.3.2) and transplanted into Tg(kdrl:mCherry) larvae as previously established (see 4.1). To avoid any impact on the experiment due to the order of the transplanted samples, ER- and NR-samples were transplanted alternating. One patient sample was handled at the same time, as number of larvae that could be imaged simultaneously was restricted to approx. 16 individuals, due to the used frame interval of 5 min. Due to one person handling all steps of the trial, the experiment could not be blinded.

At 4 hpi transplanted larvae were anesthetized and embedded. For each larva, a time lapse movie with one field of view of the niche was recorded for a duration of 180 min. On average, approximately ten larvae per patient survived the imaging under anesthesia and did not drift out of the frame (Figure 24A). These larvae were subjected to tracking analysis as established before (see 4.2.3.2). Again, the max. distance of the spots within two frames was set to 15 µm (see 4.2.3.3). Putatively, fast moving cells that could be overseen are not the ones interacting strongly with niche cells. In addition, cells that resided for an extended period within the niche are more likely to interact more efficiently with niche cells. Thus, solely tracks with a minimum

duration of 30 min were considered. This reduced the total number of tracks that were analyzed (all patients and all larvae), of initially 13,278, to 4,379 (Figure 24B). For later comparative analysis, the mean value of all tracks per analyzed parameter within one larva, was calculated and considered as one data point.

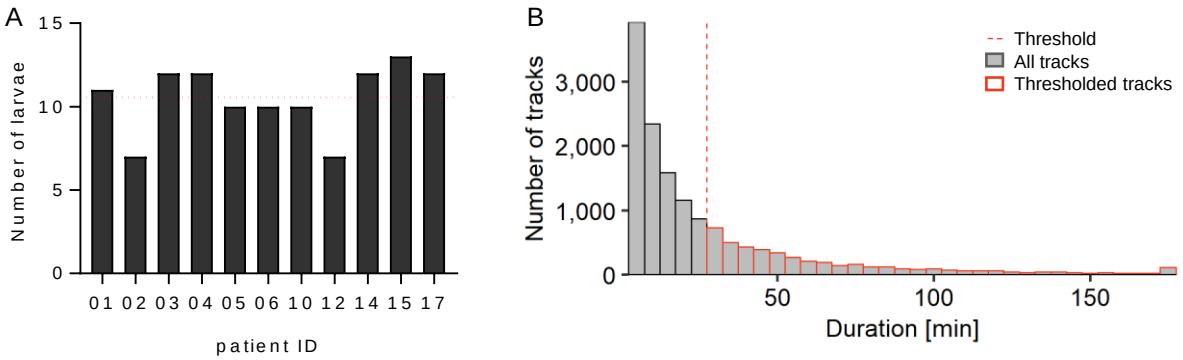

Figure 24 Numbers of analyzed larvae and tracks.
(A) Number of analyzed larvae per patient. Mean value of analyzed larvae is marked with red dashed line. **(B)** Histogram of all detected tracks (of all patients and all larvae), depicts the track duration distribution (filled gray). Tracks that had a minimum duration of 30 min (threshold indicated with red dashed line) were used for analysis and are framed in red.

4.3.3.1 ER-LCs migrated slower

As a first parameter of cell migration, the velocity of LCs was analyzed. Applying the track analysis as described above (see 4.3.3), the highest possible detectable velocity was 3 µm/min. Comparative analysis of NR-LCs vs. ER-LCs showed that ER-LCs migrated on average 0.61 µm/min while NR-LCs had a velocity of 0.69 µm/min. Hence, ER-LCs moved significantly slower, with a reduction of 12% (Figure 25A). To determine the cause of this reduced velocity, the mean duration of the tracks within the niche was analyzed. ER-LCs and NR-LCs had an average track duration of 66 min and 62 min, respectively. No statistical difference in track duration between NR-LCs and ER-LCs was observed, however, by trend, ER-LCs resided longer within the niche (Figure 25B).

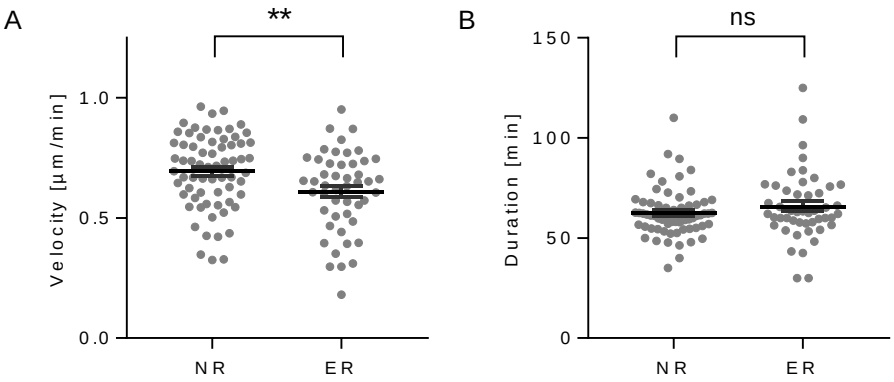

Figure 25 ER-LC migrated slower.
(A) Quantification of the cell velocity**. (B)** Quantification of the track duration. **(A, B)** Each point of the scatter-plot represents one larva of NR-patients or ER-patients. Mean value ± SEM is depicted. (NR: n=68; ER: n=48, unpaired t-test with Welch's correction, ** p≤0.01, ns not significant). Data of individual patients can be found in Supplementary Figure 1.

4.3.3.2 ER-LCs were more confined in their movement

Since track durations were statistically very similar between the groups, the difference in velocity must be due to a change in distance traveled. In a first step, all the paths of all tracks were plotted in one graph (rose plots). They show that LCs migrated more in x-direction than in y-direction, as the CHT is an oval shaped tissue. Only very few of the ER-LCs migrated more than 25 µm in x-direction, while NR-LCs migrated approximately 10 µm more. Interestingly, all the very long tracks of the NR-LCs showed a high degree of forward progression (long extensions), indicating free movement. For ER-LCs, some of the rather longer tracks turn more stationary at the end, as for instance the two tracks in the area of (+10/-22) and (-30/+15) (relative x-/y-position) (Figure 26).

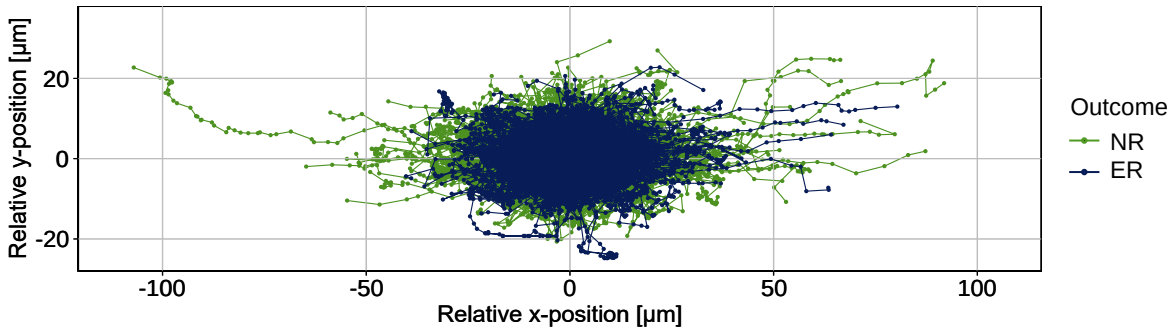

Figure 26 Visualization of migration via rose plots of single-cell trajectories.
Overlaid rose plots visualizing all cell trajectories present in the NR-sample (green) and ER-sample (blue). (Cumulated data of all larvae per outcome). The origin of all trajectories was shifted to (0,0).

To analyze the paths in more details, different parameters were quantified. Figure 27 illustrates the three analyzed distance parameters: (i) *Total distance traveled,* represented the cumulated distances between all frames (all black lines summed up), (ii) *Max. distance traveled*, represented the max. distance of a cell within all frames of the whole track (blue line), (iii) *Track*

displacement, represented the distance between the location of the cell at the first and the last frame (red line).

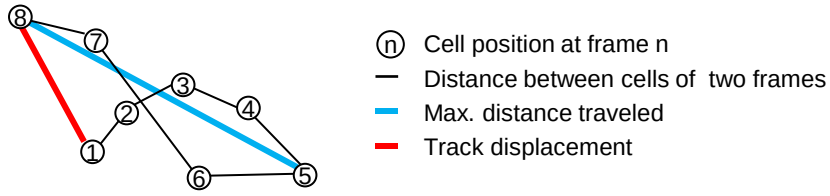

Figure 27 Schematic visualization of distance parameters.
Each circle represents the localization of a cell at the given frame of the movie, indicated with the number (frame 1 to 8, representing a 35 min lasting track). Black lines connect the cell position of two consecutive frames. Sum of all black lines is analyzed as 'Total distance traveled'. Blue line depicts the 'max. distance' of this cell during the whole track. Red line depicts the 'track displacement' of the cell between the first and last frame of the track.

The analysis of the total distance traveled showed that ER-LCs and NR-LCs migrated on average 37 µm and 39 µm, respectively. No statistically relevant difference was detected (Figure 28A). For the max.distance traveled, a significant difference was observed. While ER-LCs migrated maximally 14 µm, NR-LCs migrated 16 µm (Figure 28B). On average ER-LCs moved around within a 13% smaller area than NR-LCs. In addition, the track displacement was significantly decreased by 17% for ER-LCs (Figure 28C). ER-LCs and NR-LCs had a track displacement of 12 µm and 14 µm, respectively. This data indicates that ER-LCs moved within a more restricted area of the CHT.

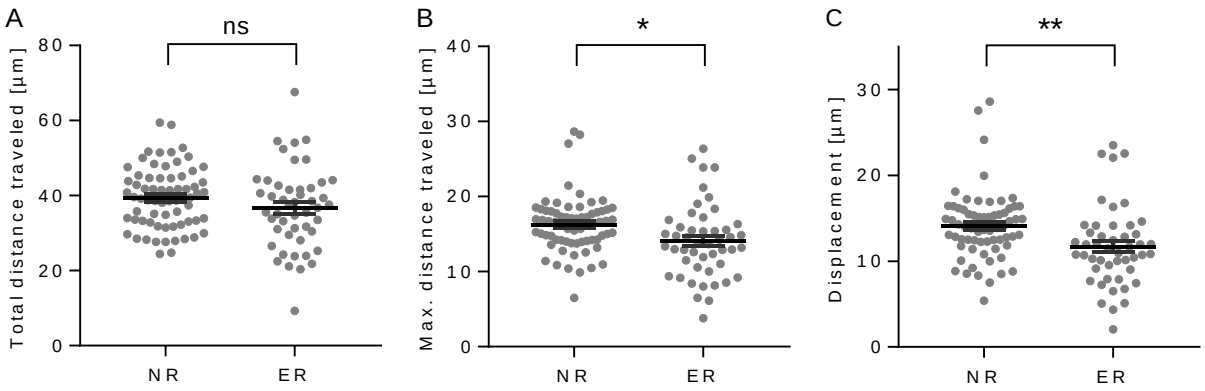

Figure 28 ER-LCs had a reduced max. distance traveled and track displacement.
(A) Quantification of the total distance traveled**. (B)** Quantification of the max. distance traveled. **(C)** Quantification of the track displacement. **(A, B, C**) Each point of the scatter-plot represents one larva of NR-patients or ER-patients. Mean value ± SEM is depicted. (NR: n=68; ER: n=48, unpaired t-test with Welch's correction, * p≤0.05, ** p≤0.01, ns not significant). Data of individual patients can be found in Supplementary Figure **1**.

The confinement ratio describes how efficient cells migrate with regards to forward progression and is calculated by dividing the track displacement by the total distance traveled. This parameter does not have a unit and can range from 0 to 1. High values indicate a very efficient forward migration, while a low number indicates a rather stationary path. Calculating the confinement ratio of ER- and NR-LCs showed mean values of 0.34 and 0.39, respectively and

demonstrated that ER-LCs were by 11% more confined in their movement. This difference was statistically different (Figure 29A). Another parameter that characterized migratory features was the mean straight line speed. This value gave information about the notional speed of the cell when moving along a straight line. Here, ER-LCs were migrating significantly slower than NR-LCs, 0.22 µm/min and 0.27 µm/min, respectively. Mean straight line speed was by 20% reduced for ER-LCs (Figure 29B).

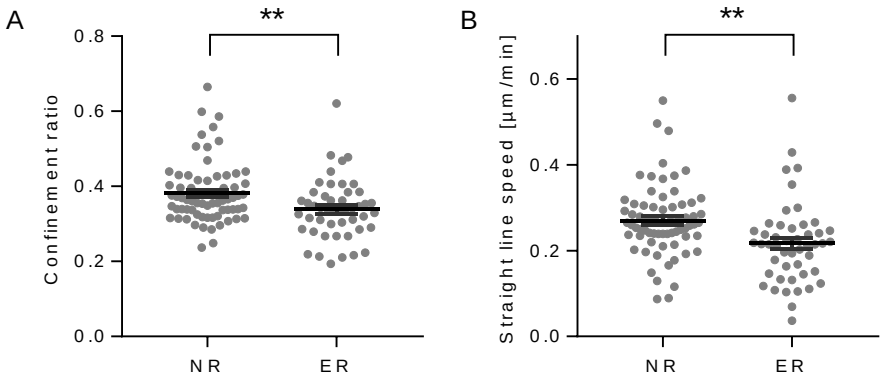

Figure 29 ER-LCs were more confined in their movement and had a reduced straight line speed.
(A) Quantification of the confinement**. (B)** Quantification of the straight line speed. **(A, B)** Each point of the scatter-plot represents one larva of NR-patients or ER-patients. Mean value ± SEM is depicted. (NR: n=68; ER: n=48, unpaired t-test with Welch's correction, ** p≤0.01). Data of individual patients can be found in Supplementary Figure **1**.

Taken together, ER-LCs migrated slower and were more confined in their movement. This suggests that ER-LCs were more anchored within the niche as these cells moved within a more restricted area.

4.4 Scoring of migration patterns identified risk potential

To determine the observed migratory differences for individual patients, a score that ranked the migration behavior was established. For each significantly altered parameter, namely velocity, max. distance traveled, displacement, confinement ratio and straight line speed, high scores were assigned to the effect of the ER-group. Hence, the effect of the NR-group received low scores. As an example: ER-LCs traveled slower than NR-LCs, thereby the patient with slowest LCs got the score 10 and the patient with the fastest LCs got the score 0. For all other patients the score was calculated relatively (Figure 30A). Adding up the individual scores for each patient, a summary score was calculated. Generally, most patients had an intermediate score. However, some patients, namely patient-12, -06 and -17 showed a clear difference in their behavior within niche. Still, it is remarkable that four out of five ER-patients received the highest scores (Figure 30B). Calculation of the mean score for each patient and statistical comparison of ER- and NR-patients reveals significantly higher scores for ER-patients (Figure

30C).

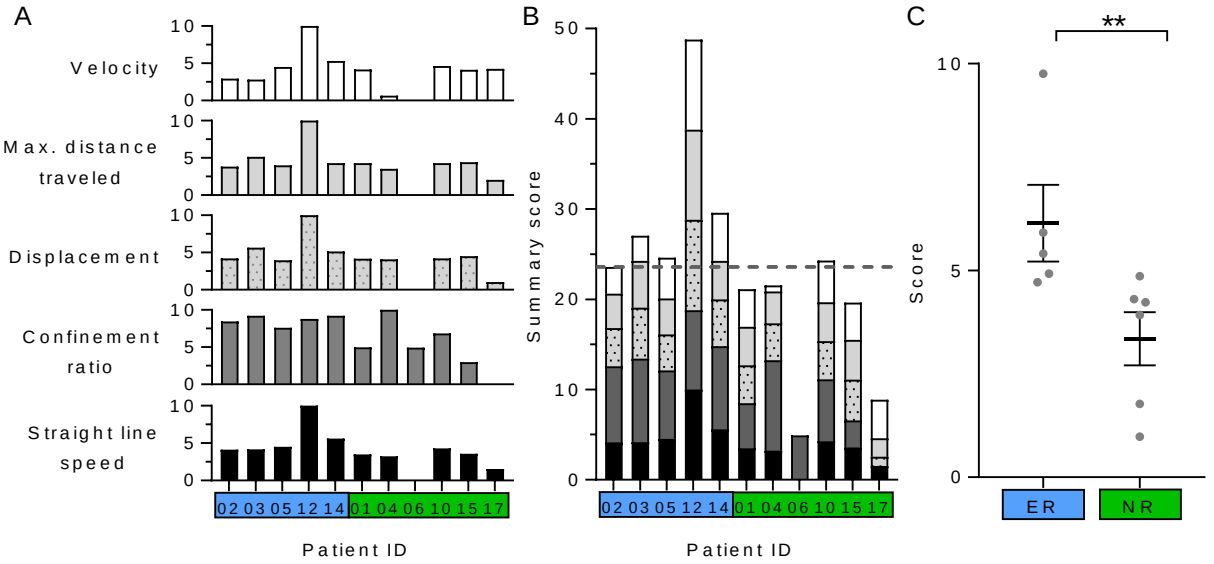

Figure 30 Scoring of migration parameters for individual patients.
Bar graphs depict the calculated score for **(A)** each significantly different migration parameter or **(B)** the summary score for all eleven individual patients. (ER-samples: blue, NR-samples: green). **(C)** Quotient of the summary score divided by the five parameters for each individual patient is depicted, grouped according to their outcome. (ER: n=5; NR: n=6, Mann-Whitney test, ** p≤0.01)**.**

Taken together, this pilot study of eleven patients showed that the identified differential migratory behavior between ER and NR-samples correlated with the clinical outcome of all individual patients. This might be a useful prognostic tool, at the time point of initial diagnosis, to assess relapse potential with regards to leukemia-niche interaction in the clinic.

4.5 Single cell sequencing of pediatric BCP-ALL cells with different risk potential

The analysis of the migration patterns of LCs with different clinical outcome revealed differences and suggests an increased anchoring of ER-LCs within the niche. In order to identify mechanisms that are involved in the phenotype of stronger niche anchoring of ER-LCs, transcriptome analysis of the LCs was performed. Two patient samples with distinct phenotypes were selected for further analysis. Considering the calculated score (see 4.4) as the indicator of niche anchoring, patient-12 represented the most anchored sample and was therefore selected to represent the phenotype of relapse cells, while patient-17 was analyzed as the no relapse sample, which was more mobile within the niche (Figure 30). Notably, patient-06 showed a stronger phenotype, however, no patient material was available for further analysis.

Single cell RNA sequencing using the 10x Genomics technology was performed, to determine differentially expressed genes of these two patient samples. Applying this method, individual cells of a complex mixture can be characterized. Rare cell populations, which would be overlooked using conventional bulk methods, can be identified. Consequently, the analysis of bone marrow aspirates offers the possibility to identify transcriptional differences not only of leukemic blasts, but also of niche cells.

4.5.1 Identification of cell populations

Cells of identical bone marrow aspirates that were used for the xenotransplantation assay to identify differential migratory behavior, were applied to single cell RNA sequencing. Library construction of single cells, quality control and next generation sequencing (NGS) as well as initial sequencing data analysis was performed by the laboratory of Bradley Blaser at Ohio State University, USA.

Quantification of the recovered cells that met quality control criteria, resulted in 4,082 and 3,134 cells for the NR- and ER-sample, respectively and were included into further analysis. To visualize the high-dimensional data in one graph, datasets form both samples were merged, cell coordinates calculated, using uniform manifold approximation and projection‘ (UMAP) and plotted (Figure 31A). Labeling of the individual patients showed that the cells of the two samples were very different regarding their expression profiles. There was no overlap of the relative localization in the UMAP-projection between cells of the ER-sample (blue) and NR sample (red) (Figure 31A). Nine distinct cell clusters were identified and differentially colored in Figure 31B. The partitions were assigned to cell types after manual inspection of their top 50 specific genes. In Figure 31C, two representative marker genes for each partition are emphasized and demonstrate transcriptional differences. For the ER-sample, two leukemic blast populations (*blast2.1* and *blast2.2*) were identified. In addition, one partition was identified that represents dividing cells (*dividing*), which can also be associated to the leukemic blasts. The NR-sample consisted out of three separated blast populations (*blast1.1*, *blast1.2* and *blast1.3*) plus one blast population consisting of stressed cells (*stressed*). In contrast to all blast populations, which were clearly defined for each individual patient, there was a T-cell partition (*T*) that consisted of cells of both patients, just like the partition of red blood cells (*RBC*) (Figure 31B). Interestingly, no other type of niche cells, such as macrophages or endothelial cells could be identified. Possibly, this was due to the fact that for both patients the bone marrow aspirates consisted of more than 85% leukemic blasts (data provided by the clinic).

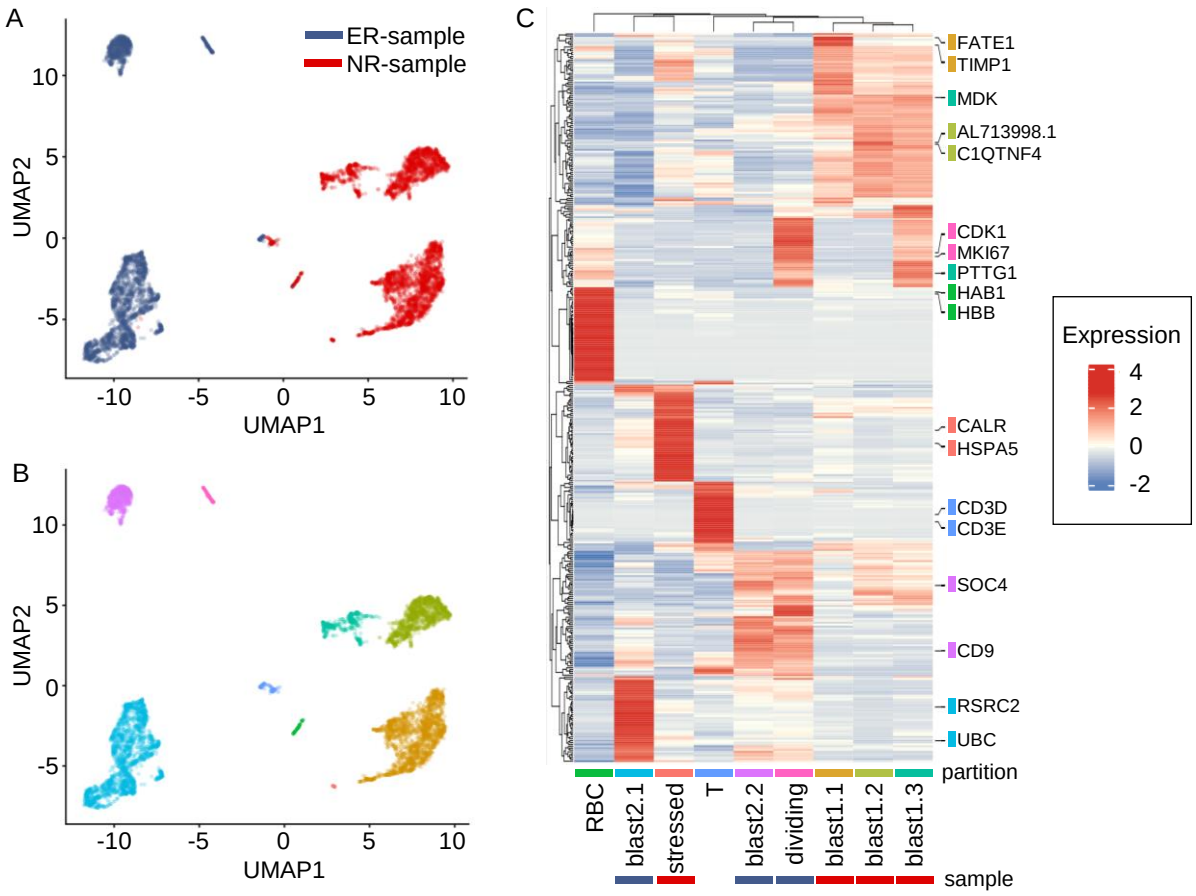

Figure 31 Categorization of samples and cell types.
(A, B) UMAPs of 7216 single cells**. (A)** Individual cells of the two analyzed samples are colored (red = NR; blue = ER). **(B)** Color-coded visualization of the partitions. Cell type assignment as indicated with the color-code in (C). **(C)** Unsupervised hierarchical cluster heat-map of all 450 genes (50 top specific genes per partition). For each partition, the two top specific genes are labeled. Partitions are affiliated with respective sample color (red = NR; blue = ER).

Taken together, we analyzed single-cell gene expression profiles of two patient samples with different *in vivo* phenotypes. The leukemic blast populations clustered separately between the ER and NR-sample, but also within one patient sample, a number of distinct cell populations were detected.

4.5.2 Identification of differentially expressed genes

In a next step, comparative analysis of the gene expression data between all blast cells of the ER- and NR-sample was conducted (in collaboration with laboratory of Bradley Blaser). Generally, 33,538 different transcripts were identified. The comparison revealed 5,965 significantly ($q < 0.05$) differentially expressed genes. To narrow down the high number of candidate genes for further analysis, only genes with an estimate of >1,5 or <-1,5 were included. After this step, 752 genes that were up-regulated and 875 genes that were down-regulated in the ER-sample were processed for further analysis (total 1,627 genes) (Figure 32A, B).

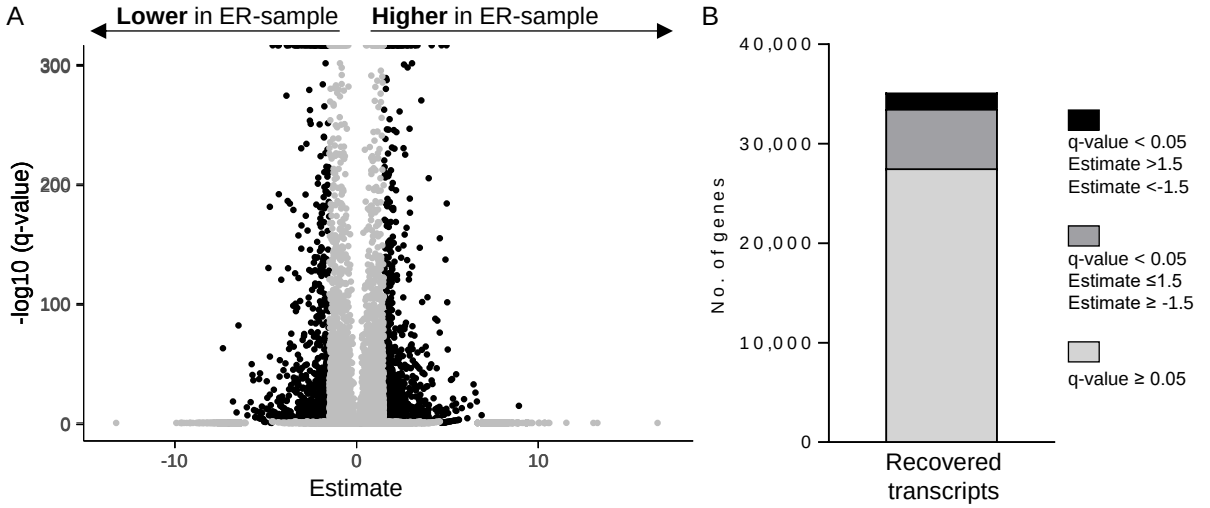

Figure 32 Selection of significantly dysregulated genes.
(A) Volcano plot of 33,538 detected genes. Black labeled: q-value < 0.05 and estimate >1,5 or <-1,5; gray labeled: q-value ≥ 0.05 or estimate ≤1,5 and ≥-1,5. **(B)** Stacked bars visualizing the distribution of the gene numbers according to p-values and estimate. Black labeled genes were used for further analysis.

4.5.3 Identification of affected signaling pathways

Next, cellular functions that were differentially activated between the two samples were identified. Therefore, all 1627 dysregulated genes were used and a pathway analysis using IPA (QIAGEN) was performed. Here, 54 significantly influenced diseases and cellular functions were identified (z-score < -2 or > 2) (Figure 33). The two most inactivated functions in the ER-sample were ‘morbidity or mortality’ and ‘organismal death’, indicating high survival of ER-cells. Interestingly, in the ER-sample, characteristics of hematologic malignancies were inactivated when compared to the NR-sample (e.g. ‘hematopoietic neoplasm’, ‘neoplasia of blood cells’, ‘neoplasia of leukocytes). The most activated function found, was ‘development of body trunk’, which belongs to embryonic and organismal development, followed by functions that were related to infectious diseases (‘infection by RNA virus’, ‘replication of virus’, ‘infection of cells’, ‘replication of RNA virus’ and ‘development of vasculature) and functions involved in endothelial cell interaction (‘angiogenesis’ and ‘extravasation of cells’). Furthermore, functions that demonstrate the tumors’ high aggressiveness were found (‘cell survival, ‘advanced stage tumor’, ‘advanced malignant tumor’, ‘secondary tumor’, ‘invasive tumor’ and ‘cell viability of tumor cell lines’). Interestingly, processes, such as ‘adhesion-‘, ‘binding-‘ and ‘interaction of tumor cell lines’ were also shown to be significantly activated within the ER-sample. This result matched my functional observations of the ER-sample being more anchored within the niche (see 4.3.3). Genes that were involved in processes, such as adhesion represent highly interesting candidates for further functional analysis to investigate their contribution to relapse development.

Taken together, IPA provided a high number of activated and suppressed functions that are involved in multiple cellular processes and indicate the high aggressiveness of the ER-sample. As stronger niche anchoring of cells of the ER-sample was observed in the xenotransplantation assay, functions, such as adhesion, binding and interaction were particularly interesting to analyze in more detail. With this rationale, we subsequently focused on the functions ‘adhesion-‘, ‘binding-‘ and ‘interaction of tumor cell lines’.

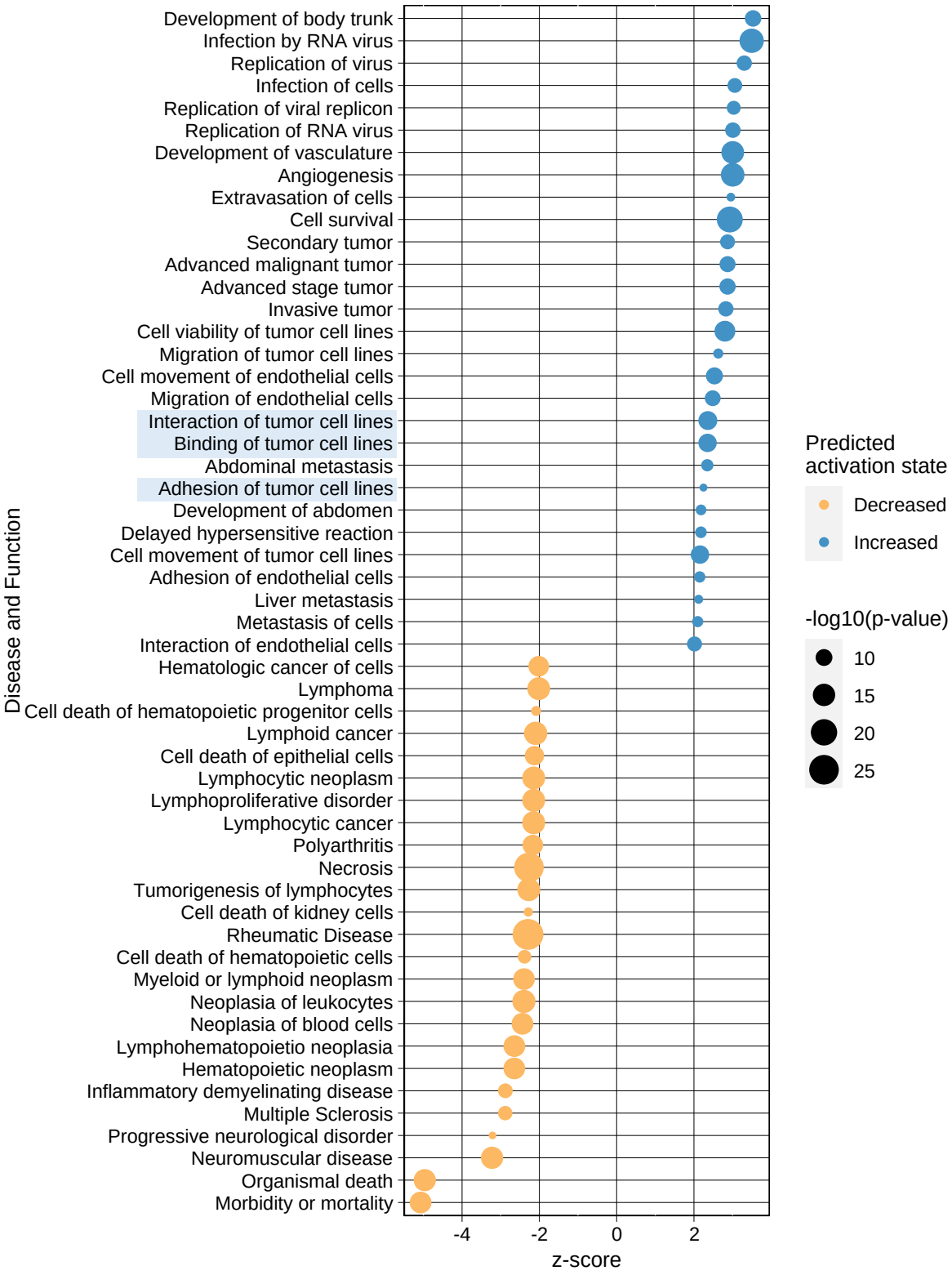

Figure 33 Overview of 54 significantly altered diseases and functions.
Result of the IPA. Blue labeled functions are predicted to be activated; Activation of orange labeled ones are predicted to be decreased.

4.5.4 Identification of candidate genes that were involved in adhesion, binding and interaction

IPA analysis provided evidence that processes of ‘adhesion-‘, ‘binding-‘ and ‘interaction of tumor cell lines’ were involved in enhanced niche anchoring of cells causing relapse. Consequently, genes, that are assigned to these functions represent highly interesting candidates to better understand relapse development.

The three functions comprised 86 genes in total, whereof 58 genes were predicted to affect or increase the respective function (‘adhesion-‘, ‘binding-‘ and ‘interaction of tumor cell lines’) (Supplementary Table 1), while 28 genes did not. These 58 genes showed an overlap of 40 consistent genes within all three functions (Figure 34A) of which 10 genes were down regulated (negative estimate) and 30 genes were up-regulated in the ER-sample (positive estimate) (Figure 34B).

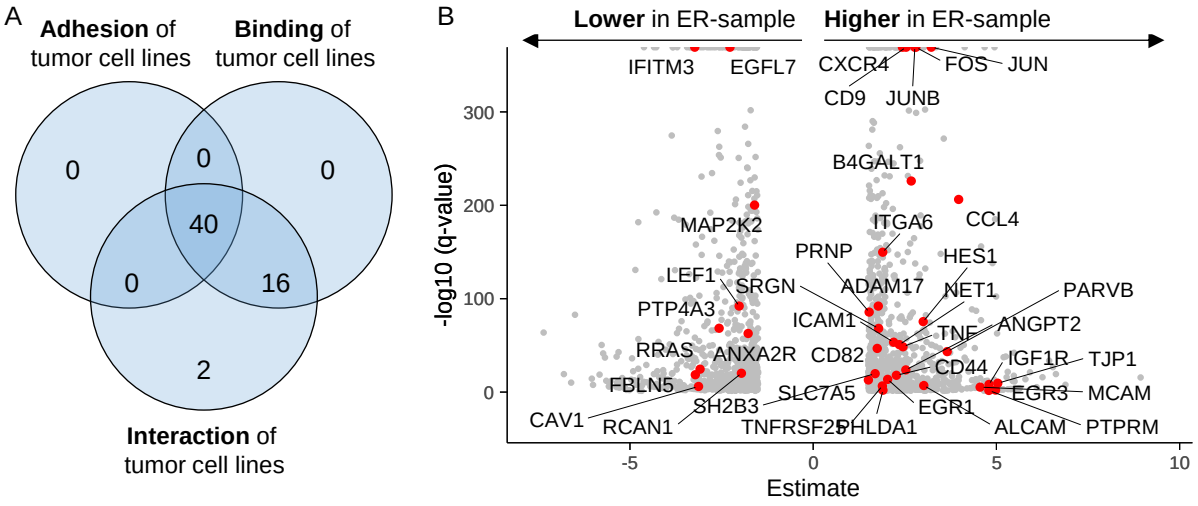

Figure 34 Selection of interesting candidate genes involved in adhesion, binding and interaction.
(A) Venn diagram of the genes predicted to activate or alter the function for the three interesting functions. **(B)** Volcano-plot of all genes subjected to IPA analysis. Genes that were commonly involved in all three functions are labeled and marked in red.

Among these 40 overlapping genes, interesting cell adhesion molecules, such as the immunoglobulin superfamily MCAM, ICAM-1 and ALCAM, the integrin ITGA6 and the tetraspanins CD9 and CD82 were found. Furthermore, chemokines and cytokines as well as receptors, such as CCL4 and CXCR4 were detected. Visualization of the gene expression in individual cells using the UMAP projection showed that some genes were frequently expressed among the blast cells of the ER-sample (e.g. CD9, ITGA6 and CXCR4) while others were expressed only in certain blast cells of the ER-sample (e.g. ALCAM, MCAM and CD82) (Figure 35). However, it did not appear that these genes were exclusively expressed in one of the three blast partitions that were assigned to the ER-sample (Figure 31A, B).

This single cell data demonstrates heterogeneous expression profiles of certain adhesion molecules among blast cells, which would not have been detectable with bulk sequencing.

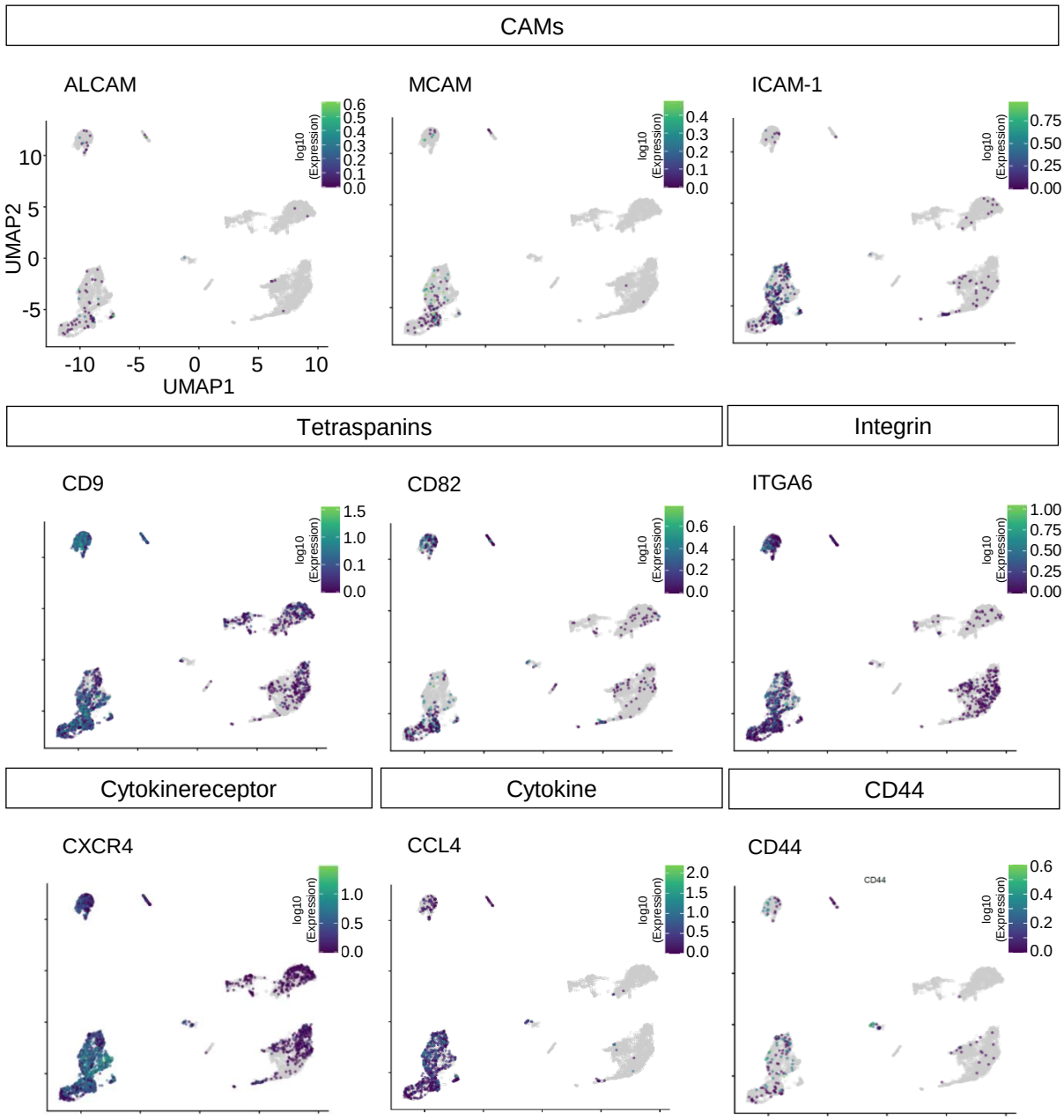

Figure 35 Expression pattern of selected candidate genes.
Relative expression of indicated genes was visualized on UMAPs for individual cells. Assignment of the partitions to the respective patient can be seen in Figure 31.

4.5.5 Co-expression analysis of candidate genes

A single molecule is rarely responsible for a complex process such as cell adhesion. It is rather a collaborative effect of a number of molecules that ultimately cause adhesion and therefore, a subpopulation with a distinct “adhesion signature” might have been decisive during relapse development. Also, literature suggests a subpopulation of the initial tumor being responsible

for relapse development [112]. Consequently, I assessed whether there was a specific fraction of blasts in the ER-sample that expressed a particularly high number of certain adhesive transcripts by analyzing co-expression of a number of candidate genes associated with adhesion.

From the overlapping 40 genes (Figure 34), genes that were up-regulated in the ER-sample and known to be directly involved in cellular adhesion (based on literature research), were selected as candidate genes. This resulted in 14 interesting candidate genes, associated with the ER-sample (depicted in Figure 36C, blue) that were used for further analysis. For these candidate genes, co-expression analysis was conducted (in collaboration with the laboratory of Bradley Blaser). The aggregated expression of the candidate genes was calculated for each cell within the dataset. Figure 36A depicts the “aggregated expression score” using UMAP projection. ER-LCs had a high aggregated expression score, indicating that candidate genes were co-expressed in most cells. When looking at the individual partitions, it looks like the co-expression was rather evenly distributed and not enhanced within one of the blast populations. Consequently, blasts of the ER-sample seemed to express a rather uniform pattern of these adhesion molecules and not one specific population being responsible for enhanced adhesion. In contrast, NR-LCs did mostly not express these genes and if, they obtained a low co-expression score. To analyze specificity of co-expression, a contrasting list of 14 genes (depicted in Figure 36C, red), associated with the NR-sample was selected. Here, the ‘neuromuscular disease’ function of the IPA, was used to select the genes. As expected, these genes were highly co-expressed in the NR sample, while cells of ER-sample received low co-expression scores (Figure 36B). This further demonstrates the difference of the two samples.

The aggregated co-expression score suggested that the 14 candidate genes were uniformly co-expressed in the ER-cells. However, this analysis did not consider sufficiently enough that not all the genes were expressed in all cells, as the score was an aggregated value. Hence, to take a closer look on the probability of specific genes to be co-expressed, the correlation of each gene to the respective others was assessed. With this, specific highly co-expressed genes among the candidate genes might be identified. As statistical and technical limitations impeded one to one correlation of the candidate genes for single cells, cells were clustered into 32 small groups according to Louvain clusters (Figure 36C). Next, the average counts for each gene across the cells in those groups were taken and correlated to all other genes of interest. Figure 36D shows the heat-map of the 14 candidate genes (red) and the 14 additional genes, associated with the NR-sample (blue). Here, strong co-expression of all 14 candidate genes was visible (positive pearson correlation, shades of red), while these candidate genes were not co-expressed with the list of 14 contrasting genes (negative pearson correlation, shades of blue). Analyzing the unsupervised hierarchical cluster heat-map, it became apparent that all 14 candidate genes clustered together when compared to the contrasting gene set.

Within the 14 candidate genes, three main clusters are visible, indicating three groups of genes that were more likely to be co-expressed. Looking at specific correlations of the candidate genes, it is visible that for instance CXCR4 is very likely to be co-expressed with most of the genes (pearson correlation > 0.5), while CD44 is only moderately (pearson correlation < 0.5) co-expressed with only few genes (e.g. ADAM17, CCL4 and ICAM-1).

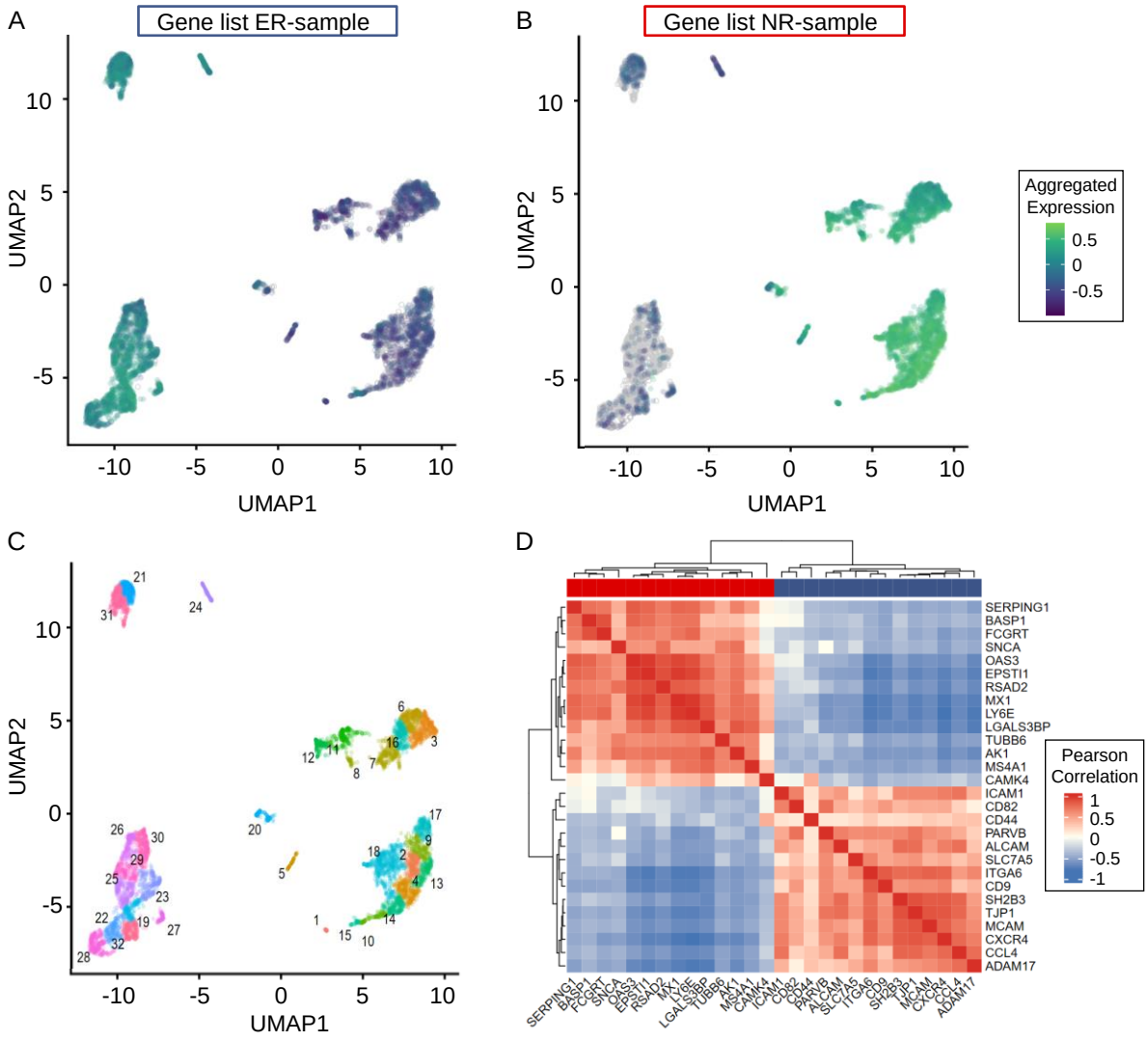

Figure 36 Co-expression of candidate genes.
(A, B, C) UMAPs of the single cell data. **(A)** Depiction of the aggregated expression score for the 14 candidate genes, associated with the ER-sample. **(B)** Depiction of the aggregated expression score for the 14 genes, associated with the NR-sample. **(C)** Visualization of the cell clusters (n=32) used for co-expression correlation of two genes. **(D)** Unsupervised hierarchical cluster heat-map of the co-expression correlation of two genes for the 14 candidate genes (blue) and 14 genes associated with the NR-sample (red). Positive pearson correlation is depicted in red, negative in blue.

Taken together, the single cell data analysis demonstrated that there were different subpopulations of leukemia cells within the ER-sample. However, the selected candidate genes, that were associated with stronger adhesion, were rather uniformly co-expressed within the ER-cells. In my data, no specific subpopulation was identified with an altered adhesive signature. This data emphasizes the potential of single cell data, as these observations would

not have been possible with bulk sequencing.

In summary, I established an innovative xenotransplantation model of ALL using larval zebrafish, which enabled the analysis of human primary LCs in a functional and complex microenvironment. Comparative analysis of the migration of cells of ER- and NR-patients revealed five parameters that demonstrated differential migration. It became apparent that ER-cells migrated slower within the niche and resided in a reduced area compared to NR-cells, indicating stronger anchoring and interaction with niche cells. An anchoring score was implemented, which ranked “niche anchoring” for all eleven individual patients used for this study. Interestingly, four out of five ER-patients received the highest anchoring scores, suggesting its relapse-prognostic potential in a clinically timely manner of the analysis within only two days. Ultimately, cells with distinct differences in motility were transcriptionally analyzed and showed that ER-cells co-express a distinct pattern of certain adhesion molecules, making them very different from NR cells.

5 DISCUSSION

Children with ALL that suffer a relapse have a poor prognosis [11]. A better understanding of the mechanisms that lead to relapse is important in order to improve risk stratification at the time of diagnosis and to develop novel therapies. Recent studies suggest a pivotal role of the leukemia microenvironment during leukemia development, maintenance and also relapse onset [19, 20]. However, appropriate models that enable the analysis of LCs in an orthotopic niche are lacking.

In this project, I developed a model to study leukemia-niche interactions *in vivo* by means of the establishment of a larval zebrafish xenograft model of pediatric ALL. Here, LCs engrafted within the niche and showed distinct interaction with niche cells. The systematic transplantation of primary patient BCP-ALL cells with different risk potentials revealed differential migratory and adhesive properties, which were demonstrated to be potentially relevant for clinical risk stratification. Ultimately, LCs of two patients, which showed a clear differential *in vivo* migratory behavior, were transcriptionally analyzed and provided interesting candidate genes that were potentially involved in stronger niche anchoring of the ER sample.

5.1 Larval zebrafish constitute a reliable orthotopic model for xenotransplantation of ALL cells

Larval zebrafish xenografts represent attractive models to study LCs in a reasonable complex microenvironment, as zebrafish are highly fertile, cost effective and easy to rear and keep. Furthermore, optically transparent mutants enable *in vivo* high resolution imaging in high numbers, which is not as feasible with rodent models [113]. I aimed at establishing a robust workflow for the xenotransplantation procedure, which required LC homing, engraftment and proliferation as well as normal development of larvae, to ensure an intact niche compartment for functional studies.

Larval xenotransplantation models of cell lines and primary cells of different tumor entities were published in the past [57, 58], including leukemias [62, 63, 67]. Current gold standard for the developmental stage for xenotransplantation is 48 hpf [107]. The growing number of studies published, showed that the transplantation procedure and subsequent rearing temperature differed greatly, depending on the research question.

Human cancer cell injections directly into the yolk sac were widely used for pre-clinical drug testing [63, 67] and the analysis of the metastatic phenotype of solid tumors [72], while systemic injections into the blood circulation were mainly used to study cell dissemination [83] and metastatic features [64]. To allow dissemination of LCs in the whole body, in order to

monitor LC homing and engraftment within the orthotopic niche, in the present study, LCs were transplanted into the blood circulation via the duct of Cuvier and were distributed with the blood flow throughout the body. Subsequent evaluation of the dissemination of LCs after transplantation using *in vivo* imaging demonstrated homing of LCs to the hematopoietic niche, the CHT area (Figure 7).

Given the differential body temperatures of humans and fish of 37°C and 28.5°C, respectively, it is an ongoing debate how to compromise best between the temperatures to not harm fish development but to support cancer cell proliferation and engraftment. Up to a developmental stage of 48 hpf, rearing at the physiologic temperature of fish is very important for optimal development. Rearing of the embryos at 36°C after 48 hpf showed only minor mortality rates or malformations of the larvae when compared to rearing starting earlier at 36°C [114]. Subsequent to the transplantation, increasing the rearing temperature to 36°C enhanced proliferation and survival of human cells greatly, when compared to 34°C [59], which was widely used in other studies [62, 65], while transcriptional differences remained minor [114]. Adequate development of the larvae upon transplantation was essential when analyzing niche components of the fish, however, engraftment of LCs was considered equally important for the intended model. In conclusion, for the present project, embryos were bred at 28.5°C until 48 hpf, according to published literature [59]. Subsequent to the xenotransplantation of LCs, larvae were reared at 36°C. In my experiments, no severe developmental abnormalities were observed and most of the larvae developed normally. This is in line with the results of Cabezas-Sainz et al. [59]. Larvae that showed developmental abnormalities were excluded from the study.

With the described transplantation and rearing procedure using published literature as a basis, I was able to observe LC homing and engraftment in the CHT within three days of follow up time (Figure 7), with the tumor burden increasing over time (Figure 8) as monitored with serial *in vivo* imaging. Notably, not exclusively LCs are documented to home to the CHT. Sacco et al. transplanted multiple myeloma cells into the blood circulation of larvae and showed that the myeloma cells resided in the CHT area shortly after transplantation while cells of a cervix carcinoma did not [83]. Interestingly, a breast cancer cell line, known to build bone marrow metastasis, also homed to the CHT area [83, 115]. In addition, primary cells of a breast cancer bone marrow metastasis engrafted within the CHT area [115], supporting the idea of an appropriate conservation of zebrafish niche components to resemble a bone marrow like environment, recognized by human cancer cells.

When analyzing LCs after systemic transplantation, monitoring of the tumor burden at a single time point is not sufficient to clearly demonstrate whether LCs underwent cell divisions or if they homed more efficiently to the CHT over time. As demonstrated using *in vivo* time lapse

imaging, my results clearly demonstrate cell divisions of human LCs within the zebrafish (Figure 11). Furthermore, the analysis with a proliferation sensitive dye using flow cytometry showed that individual cells underwent up to five cell divisions within only three days (Figure 10). This result is comparable to the data of Vargas-Patron et al., who demonstrated up to four cell divisions of glioblastoma cells within three days using a similar approach [116]. Notably, to my knowledge no other study demonstrated cell divisions within larval xenografts of LCs in such detail.

In summary, by compiling published methodologies, I established a workflow for orthotropic LC xenotransplantation into larval zebrafish for the first time in our laboratory.

5.2 LCs interact with macrophages and show specific distribution pattern within the vasculature

I assessed the suitability of the established model to study LCs in a complex and functional microenvironment. Yet, larval xenografts were mainly used to study drug response [63, 67, 117] or metastatic properties of solid tumors [64, 65, 72, 115] and the model was seldom used to analyze interactions with surrounding tissue. However, identifying crucial interactions would be important to identify characteristics of the microenvironment that are important in processes, such as tumor development, maintenance but also relapse onset. The CHT niche consists of endothelial cells, macrophages, stromal cells and other cell types, very similar to the architecture of the equivalent mammalian bone marrow niche, except for osteoblasts and osteoclasts [46]. In order to assess the suitability of the model, I investigated if and how LCs were in contact with certain niche cells. Larval zebrafish are especially good recipients for xenotransplanted cells as they did not develop adaptive immunity yet [60]. Still, the analysis of cellular parts of the innate immune system is feasible, as macrophages are already present as early as 24 hpf [61]. To date, only a very few studies exist that analyze the interplay of macrophages and BCP-ALL. Thus, I assessed the feasibility to use larval zebrafish as a model to study macrophages in more detail.

Using *in vivo* imaging of macrophage-transgenic reporter larvae, I was able to directly monitor macrophages of the larvae (Figure 12). Generally, macrophages can be considered as a rather mobile cellular component of the niche. While fulfilling their host defending function, they patrol throughout the fish. Interestingly, some macrophages slowed down and were very stationary during the observed contact with LCs. I was able to document dynamic, close and persisting cellular interactions between LCs and macrophages, which lasted up to 10 h (Figure 13). Especially 3D renderings emphasized the close contact of the two cells. At the onset of the contact, macrophages changed their shape and developed protrusions to reach the LC. Later,

the LC was embraced by the macrophage. I observed that these long lasting contacts were released and both cells went their own way afterwards. Contrary to these observations, I saw rapid phagocytosis events of macrophages eliminating transplanted LCs (Figure 14). This demonstrated that macrophages showed a very diverse behavior towards transplanted LCs, as they were on the one hand temporary closely interacting with LCs, and, on the other hand, they were able to eliminate LCs. During these approximations, macrophages and LCs could possibly communicate extensively, resulting in processes, such as niche remodeling and leukemia progression. For instance, Roh-Johnson et al. were able to demonstrate in melanoma zebrafish xenografts that during such close contacts macrophages transferred cytoplasm to the melanoma cell, which then led to enhanced melanoma dissemination [82]. In contrast, Asokan et al. documented a prolonged interaction of an immune cell with a breast cancer cell, which finally got phagocytized [81], demonstrating the versatile polarization potential of macrophages. In another very recent publication, Póvoa et al. identified that a colorectal cancer cell population (progressors) can block macrophage-mediated tumor clearance of another colorectal cancer cell population (regressors) in a co-transplantation approach. Using individual recipients for both populations, the regressive population could not engraft, demonstrating the progressors' potential to modulate macrophages towards a pro-tumoral polarization [118].

Despite the observation of intensive contact between LCs and macrophages in my study, no enhanced infiltration or even recruitment of macrophages to the caudal part of the larva could be observed at three dpi, when analyzing relative cell numbers in a flow cytometric approach. In addition, no extensive phagocytosis of the fluorescently labeled LCs was detected when analyzing the inclusion of LCs' fluorescence within macrophages (Figure 15). Still, sporadic phagocytosis events were observed (Figure 14) and demonstrated the inter-species compatibility of phagocytes to eliminate human cells. In contrast to my observation of mild phagocytosis activity, Asokan et al. detected significantly more macrophages co-localizing with breast cancer cells, as a measurement of phagocytosis activity, after a comparable period of time after transplantation as I used for my experiments [81]. This indicates differential behavior of macrophages within different tumor microenvironments.

My data suggests a leukemia-supporting polarization of the macrophages, as a result of the close and persisting interactions, rather than an anti-tumoral phenotype, with extensive phagocytosis and active macrophage recruitment to the niche. To my knowledge, this is the first study visualizing and analyzing the interaction of innate immune cells and LCs in a zebrafish model and demonstrates the potential of the model to study their interplay in more detail.

In a next step, the localization pattern of LCs within the CHT area over time was analyzed. The larval zebrafish model enables repetitive imaging of individual larvae at different days. Here, I was able to monitor an increase in LC burden over time (Figure 8). With regards to the localization of LCs, it became apparent that at one dpi, LCs were rather uniformly spread within the vasculature of the niche, while starting at two dpi, LCs tended to build clusters within physiologically emerging extraluminal pockets. At three dpi, LCs were almost exclusively localized within these pockets and around the main artery (Figure 16). As I observed this dissemination pattern of LC localization for a number of different LCs, the extravasation and cluster formation seemed to be a specific process rather than a random behavior. Extravasation is a complex process and requires functional signaling between extravasating LCs and the endothelium [108], demonstrating a functional signaling between human LCs and the zebrafish endothelium in the present model. Subsequent to LC homing to the CHT, LCs were surrounded by a dense vessel bed, enabling signaling and thereby reprogramming of this niche component. For HSCs, Tamplin et al. showed that the remodeling of endothelial cells around HSCs, which they called “endothelial cuddling”, led to HSC proliferation [47]. A similar important function of the endothelium might be conceivable for LCs. The accumulation of cancer cells within extraluminal pockets was also described by Marcatali et al. when they were transplanting breast cancer cells. They observed these cells within these pockets for two more days, up to five dpi [115]. Interestingly, ventral of the main artery, at around three to five dpf, a vessel of the lymphoid system is emerging [119]. This is exactly the time span, in which I observed the specific distribution pattern towards the pockets. Lymphatic organs are known to be infiltrated with tumor cells [120], so there is a possibility that the pockets are associated to lymphatic tissue. This hypothesis could be proven with a suitable reporter fish line. Notably, these extraluminal pockets are not colonized by healthy HSCs. While HSCs are also evenly distributed throughout the CHT at three dpf, these cells shift towards the caudal vein at four dpf during relocation to the kidney marrow [121].

Taken together, the generated larval xenograft model is suitable to study leukemia in a complex environment. In line with studies of other tumor entities [81, 115, 118], LCs showed close and persisting interactions with macrophages and a specific dissemination pattern within the vasculature, suggesting a functional interplay with the microenvironment.

5.3 Analyzing LC migration within the hematopoietic niche of larval zebrafish

In the present project, I hypothesized that LCs that later caused relapse, utilized the niche more efficiently compared to LCs that did not. As demonstrated before, larval zebrafish xenografts are ideal to perform *in vivo* time lapse imaging, which allowed LC tracking and

thereby the analysis of cell migration as a measurement of niche utilization. In order to test the hypothesis, an experimental workflow was established that enabled the quantitative analysis of the migration of LCs. Therefore, I developed a semi-automated protocol for analysis of LC migration using the ImageJ Plugin TrackMate [96]. Subsequently, all tracks were filtered using R based scripted protocols to extract the anticipated tracks for the detailed analysis.

The robustness of the established transplantation, imaging and analysis workflow was verified using replicated transplantations of the same LCs and subsequent analysis. Here, no statistically significant differences of all analyzed migratory parameters between the individual replicates were observed (Figure 20), demonstrating its robustness and reproducibility. In contrast to my study, other studies performed manual tracking [78-80], however, these studies analyzed by far less cells and samples than I did in my project. Moreover, during manual tracking, certain bias or inaccuracies are more likely to occur. Using my semi-automated approach, the possibility of incorrect tracking can also not be ruled out completely, however, for each analyzed sample, the errors are supposed to be the same and not due to human bias. Only recently, Asokan et al. also developed a semi-automated approach applying broadly-used open-source software tools [81].

Next, I endeavored to analyze the sensitivity of the established cell tracking protocol to identify differential migration patterns. Therefore, a proof of principle experiment was designed. The adhesive molecule E-selectin, which is expressed on the larval endothelium [87] was modified, using a CRISPR/Cas9 approach with subsequent transplantations in the founder generation (G0). E-selectin is well-known to be involved in LC retention [110] and leukocyte rolling [109]. Consequently, knocking out E-selectin is expected to result in altered LC migration. This differential migration should be measurable with the established cell tracking approach. Sun et al. characterized the zebrafish E-selectin gene and protein in detail. Despite only approx. 42% amino acid sequence homology, the five domains putatively involved in E-selectin function are highly conserved [87], indicating consistent function across species and a high likelihood to cross react with human binding partners, expressed on transplanted LCs. Hence, E-selectin represented an interesting target for the proof of principle experiment.

I was able to identify significant differences in the migratory behavior of LCs after knockdown of E-selectin when compared to xenografts in control larvae. LCs resided for a shorter period of time and migrated with an increased velocity within the niche, indicating loss of anchoring due to lacking E-selectin (Figure 22). Considering that analyzed mosaic KO-larvae did most probably also express functional E-selectin in some of the cells, the fact that I was still able to detect differences within the analyzed groups demonstrates the high sensitivity of the assay. Furthermore, this proof of principle experiment demonstrated that E-selectin is high enough to be functional to interact with human counterparts.

Taken together, *in vivo* time lapse imaging and the establishment of a customized semi-automated, unbiased protocol allowed the monitoring of migratory patterns of LCs *in vivo*.

5.4 LC adhesion and migration as an indicator of relapse potential

Next, the developed model was applied to identify differences in the behavior of LCs, which clinically showed a different outcome with regards to relapse development. Importantly, for this experiments, therapy naïve cells of the initial diagnosis were used as I aimed to identify differences that were already present at time of diagnosis. Clinically, the initial risk stratification of the leukemia is decisive for the treatment approach (see 1.1.1). As relapse mainly develops due to therapy failure, innovative approaches that identify leukemias with higher relapse potential are important. I hypothesized that LCs that later developed relapse, utilize the surrounding tissue more efficiently and with different mechanisms than LCs that did not. A parameter that considers the niche is not yet considered in current risk stratification.

I transplanted eleven primary patient samples of children with BCP-ALL and analyzed their migratory behavior using the established workflow. Strikingly, I was able to identify five parameters characterizing the migration patterns that showed significant differences between the five ER- and the six NR-samples. ER-LCs migrated slower and were more confined in their migration as measured by the extent of max. distance traveled, displacement and the confinement ratio (Figure 25, Figure 28, Figure 29). A number of other studies analyzed the dissemination pattern of cancer cells using a larval zebrafish xenograft model [81, 122, 123]. While most studies analyzed cancer cell locations at a single time point after transplantation [122, 123], only Asokan et al. used *in vivo* time lapse imaging and identified differences in migration patterns of different tumors. In their study, they were comparing the dissemination of AML cells and breast cancer cells. Here, they showed that the AML-cells migrated faster and were traceable for longer distances when compared to the breast cancer cell line [81]. In contrast to my study, they compared the migration patterns in the whole body of the fish and of two very different tumor entities. Hence, differences in migration patterns are not surprising. In my study, I used cells of the same tumor entity and analyzed them within the hematopoietic niche area. Here, differential migration patterns were identified for LCs that differed in their outcome. This provides novel, highly clinical relevant insights into the biology of LCs. The more confined movement of ER-LCs suggested an enhanced utilization of the niche, which might play a role in relapse development and could potentially represent a novel important measured value during risk stratification.

In a next step, I evaluated the identified differential migratory parameters for each individual child of the eleven patients and summarized it in a score, which rated the anchoring within the

niche of the respective patient. Remarkably, four out of the five ER-samples received the highest score values (Figure 30). This result suggests a relapse predictive potential of the surveyed score. However, an independent patient cohort has to be investigated to validate this statement. Still, in view of the experimental design, it is highly promising to further explore its potential during risk stratification. The conducted assay can be performed in a clinically timely manner of only two days, which could help during risk stratification and would, for the first time, include niche-related factors in the stratification process.

Considering the transplanted cohort in more detail, it becomes apparent that five ETV6-RUNX1-positive samples (patient-02, -04, -10, -15 and -17) were analyzed. Patients with this translocation have in general a good prognosis [4, 124]. In my cohort, one out of these five patients with an ETV6-RUNX1 fusion relapsed and strikingly, this sample (patient-02) received a high score. Only one other ETV6-RUNX1-positive sample (patient-10) received a higher score out of all ETV6-RUNX1-positive sample. Correlating these results with the clinical data showed that, while patient-10 was already initially stratified as high-risk, due to very high leukocyte count in peripheral blood, patient-02 was initially stratified as low risk, and therefore presumably received less intensive therapy. One may speculate that for patient-02, the interaction with the niche might have been enhanced due to its migratory behavior described by the high score and that a reprogramming of the niche to the LCs advantage was involved in relapse development. State of the art stratification parameters, only include cell intrinsic features [5, 7], independent of surrounding tissue. Possibly, patient-02 would have benefitted from an initial classification that takes protective niche interactions into consideration.

Beside five ETV6-RUNX1-positive samples, my cohort included three hyper-diploid samples (patient-06, -10 and -12) that were initially stratified as high-risk due to high leukocyte count in peripheral blood. Interestingly, in my score, two patients that did not relapse (patient-06 and -10) received a rather low score, while patient-12 received by far the highest score of all samples and developed a very early relapse. Notably, patient-12 showed, while being hyper-diploid, a monosomy of chromosome 9. This genetic alteration is infrequent (~1.4% of all childhood acute leukemia cases) and occurs rather in T-ALL with unclear prognosis [125]. Knowing more about the underlying mechanisms that led to this high anchoring score, might represent attractive targets to fight this specific leukemia.

To my knowledge, so far only one other study tried to utilize larval zebrafish xenografts as a tool to predict outcomes of acute leukemias. Gacha-Garay et al. analyzed very different types of adult leukemia, particularly five different AML samples and only two ALL samples. Applying an integrative model, which combined clinical features, leukemia stem cell characteristics and the *in vivo* behavioral analysis in zebrafish, they suggest to predict the patients' remission outcome [122]. In contrast to my study, they transplanted LCs into the pericardial space and

not into the blood circulation. Still, they were able to identify LCs within the CHT area, meaning cells were able to intravasate and home to the distant niche site. After one day, they assessed dissemination patterns of different LCs. They suggest, that broader and random migration patterns of the cells are related to worse clinical outcome after induction chemotherapy, however, this was not an independent measurement but contributed to their integrated model of stratification [122]. This result might be partially contrasting to my observation, where ER-LCs were more anchored within the niche. However, they did not perform dynamic analysis but analyzed the distribution pattern of the LCs within the fish only at a single time point. Hence, what they describe as dispersion and migration is not comparable to the approach I used. Regarding the prognostic clinical relevance, their study lacks a clear definition of the compared groups as various leukemias were analyzed, including AML and ALL [122]. Still, my results, together with theirs, demonstrate the potential of the larval xenograft model as a meaningful addition to current risk stratification for treatment regime decisions of leukemia.

Taken together, interesting correlations between the clinical data of some specific samples and their ability to anchor within the niche, could be observed and suggested that some patients might have benefited from treatment, that releases the anchoring with the niche to make the leukemic cell accessible for chemotherapy again. It is very promising to increase the sample size in the future, to better estimate the prognostic impact of niche anchoring on relapse risk, using the established score.

5.5 Relapse causing LCs activate pathways involved in adhesion, binding and interaction processes

In order to identify the underlying mechanisms that could potentially be involved in the differential migratory and adhesive phenotype of LCs with opposing clinical outcome, two patients with diverse phenotypes were selected for further analysis. For this purpose, the calculated score (Figure 30) was considered as a measured value for niche anchoring. Patient-12 represented the most anchored sample, and was therefore selected as the ER-sample while patient-17 was analyzed as the NR-sample, which was more mobile within the niche.

As leukemia is a heterogenic disease, single cell transcriptome analysis was performed to better recapitulate different cellular subpopulations. Cells of the BM aspiration of the initial diagnosis were subjected to single cell analysis. Interestingly, the two analyzed samples showed very different expression patterns in UMAP projections and distinct subpopulations. For the ER- and NR-sample, three and four distinct blast populations were identified, respectively. In addition, two further populations were detected, which were assigned to red

blood cells and T-cells for both patients (Figure 31). No other niche cell type, such as endothelial cells or macrophages could be identified, possibly due to the bone marrow aspirates of the patients consisting of above 85% leukemic blasts.

A high number of differentially expressed genes were identified between the two samples with different relapse potential (Figure 32). *In silico* analysis of these genes using IPA revealed highly interesting functions. Thus, for instance, cell survival was predicted to be strongly increased in the ER-sample, indicating the leukemias aggressiveness. In addition, functions involved in endothelial cell interaction were described. Here, the process of extravasation was also predicted to be increased which matched my observation of LCs extravasating after xenotransplantation (Figure 16). The fact, that the ER-sample appeared to be less related to hematopoietic malignancies, as associated functions were predicted to be decreased in the ER-sample, were rather difficult to interpret, as I was comparing two samples of the same malignancy and not compared to a healthy control. Moreover, functions such as interaction-, binding- and adhesion of tumor cell lines appeared to be increased in the ER-sample (Figure 33). Genes of these functions were very likely to be involved in the mechanisms of the differential behavior observed between these two samples. Consequently, I was focusing on the detailed analysis of these genes. While for solid tumors, migration and thereby reduced adhesion is likely to result in an invasive, metastatic phenotype, which is generally associated with inferior outcome, little is known about the prognostic value of enhanced cell adhesion in leukemias and the adhesion molecules involved. In the present study, a high number of cell adhesion molecules were stronger expressed on the ER-sample. Among these genes were interesting cell adhesion molecules, such as the integrin ITGA6, the tetraspanins CD9 and CD82 and members of the immunoglobulin superfamily MCAM, ICAM-1 and ALCAM. Furthermore, chemokines and cytokines as well as –receptors, such as CCL4 and CXCR4 were found (Figure 34).

One of the strongest differentially expressed genes in my analysis was CD9, which belongs to the tetraspanins. CD9 is known to be involved in many cellular functions, such as proliferation, differentiation, migration and adhesion. In diverse cancer entities, the prognostic significance is documented variably, which is presumable due to its association with many other molecules, influencing its functionality [126]. Interestingly, for B-cell ALL, Yamazaki et al. identified CD9 as a positive modifier of cancer stem cell properties and as a marker for drug resistant cells. Moreover, knockdown of CD9 was associated with reduced leukemogenic potential in an *in vivo* experiment, indicating a tumor supportive function [127]. In a very recent study, Leung et al. reported CD9 as an independent prognostic marker for the outcome of BCP-ALL in a cohort of 153 pediatric patients. Here, patients with CD9 positive LCs had a significantly lower 5-year overall and relapse-free survival rate [128]. This is in line with my observation of a strongly enriched CD9 expression in the sequenced ER-sample, which is lowly expressed in the NR-

sample. In addition, they could show that targeting CD9 enhances sensitivity towards chemotherapy, demonstrating its clinical potential [128].

Cell adhesion is a complex process where mostly a number of molecules are involved. To assess whether genes involved in adhesion were co-expressed on a subpopulation of the ER-cells, co-expression analysis of the candidate genes was performed and showed a high aggregated co-expression score in the ER-sample while the score was low for the NR-sample (Figure 36A). Interestingly, the co-expression score was uniform among the different blast populations of the ER-sample, suggesting that the majority of cells had an enhanced adhesive potential and not one specific subset.

Among those molecules that were known to associate with CD9 [129], a number of genes were also found within the significantly dysregulated genes in my comparison, such as ALCAM, CD44 and ADAM17 (Figure 34). My gene-gene co-expression analysis showed that CD9 was likely to be co-expressed with ALCAM and ADAM17 (pearson correlation ~0.5), while CD9 co-expression with CD44 was rather moderate (pearson correlation <0.5) (Figure 36D). Of note, Jeannet et al. described that the glycoprotein ALCAM was highly expressed on HSCs, especially on long-term HSCs, where ALCAM was shown to be important for the long-term repopulating potential of those HSCs [130]. With regards to malignant cells, as for many adhesion molecules, the prognostic potential of ALCAM expression is found to be controversial as reviewed by Ofori-Acquah et al. [131]. In prostate and breast cancer, ALCAM was downregulated in high-grade tumors, while for esophageal squamous cell carcinoma and bladder cancer, higher levels were associated with poor prognosis [131]. For AML patients, Shimura-Nukina et al. proposed high ALCAM expression as an indicator of shorter overall survival. ALCAM was even higher expressed on CD34 positive AML cells than on HSCs [132]. Despite my co-expression analysis suggesting uniform co-expression of the adhesive molecules (Figure 36A), some individual genes were only lowly expressed and also not in all cells. In my single cell data, ALCAM was significantly stronger transcribed in ER-LCs, however, expression levels were low and the expression was infrequent, but uniformly distributed among the defined blast populations (UMAP projection) (Figure 35). This means only a few cells that were evenly distributed within the blast populations expressed low levels of ALCAM. Still, in my data, there were some cells with more ALCAM expression, which might have been decisive during relapse development, as literature suggests a subpopulation of the initial tumor being responsible for relapse [112]. However, this population was not clearly defined in the UMAP-projection. Interestingly, Gilsanz et al. found that in leukocytes, ALCAM functionality is enhanced via increased clustering of ALCAM molecules, directly mediated by CD9 and by CD9 mediated inhibition of ADAM17 which would otherwise cleave extracellular portions of ALCAM by its sheddase activity [133]. The very strong and uniform expression of CD9 in the ER-cells in my data suggests that its functional inhibition of ADAM17 might also be relevant

for the analyzed ER-sample. Additional potential substrates of ADAM17 that are higher expressed in the ER-cells are CD44 and ICAM-1 [134]. While CD44 was lowly and infrequent expressed but uniformly distributed among the blast populations, ICAM-1 was lowly expressed and more frequent on the blast2.1 population in my data. ICAM-1 is another adhesion molecule, which is controversially discussed regarding its prognostic significance. While some studies suggest a rather aggressive phenotype of ICAM-1 expressing breast cancer cells [135], for colorectal cancer, ICAM-1 expression was associated with reduced metastatic spread and consequently, predicted with better outcome [136]. Notably, to my knowledge, no study investigated the role of ICAM-1 in the context of malignant hematopoietic cancers, making ICAM-1 an interesting candidate for further functional studies on leukemia. Given these interesting results, it is worth to consider the analysis of more samples specifically with regards to adhesion molecules.

Taken together, the transcriptomic analysis of the two patient samples that showed a clear differential migration behavior *in vivo*, revealed very interesting genes that might be involved in the process of cellular adhesion. Some of these genes are already under discussion for their prognostic value in solid cancers while only very few studies in leukemias are looking at these adhesion signatures. Possibly, ER-LCs of patient-12 in my study utilized CD9, ALCAM and ICAM-1, to anchor within the niche for better interaction with surrounding tissue, which might have been the cause for later relapse development.

5.6 Conclusion and outlook

In the present work, a pioneering larval zebrafish xenotransplantation model of LCs was established and proven to be suitable for the analysis of LCs within a functional orthotopic niche. LCs were demonstrated to home, proliferate and engraft with a specific distribution pattern and interact closely with host macrophages. The transplantation of primary LCs of patients with different clinical outcomes revealed that LCs of ER-patients were more confined and slower in their movement, suggesting a stronger anchoring within the niche. Scoring this migratory behavior for each individual patient proposed the potential of larval zebrafish xenografts as a complementary tool during risk stratification in the clinic, which takes interactions with the microenvironment into account, whereas currently only LC-intrinsic factors are considered. Especially the rapidity of the established assay, where functional characteristics of LCs can be assessed *in vivo* in a for the clinic timely manner of only two days, makes this innovative model highly attractive. However, to promote the model into clinical routine, more samples need to be analyzed in order to verify and validate the score.

Furthermore, transcriptomic analysis of two samples with clearly differential *in vivo* behavior

revealed strong dysregulation of adhesion molecules, which were enriched in the analyzed ER-cells. In order to analyze their relevance, loss of function experiments are planned as follow up projects. These genes represent highly interesting potential drug target candidates.

In summary, the established model has the potential to identify high-risk patients upfront and identified potentially novel therapeutic targets to improve clinical outcome in pediatric BCP-ALL.

6 REFERENCES

1. Erdmann F KP, Grabow D, Spix C: **German Childhood Cancer Registry - Annual Report 2019 (1980-2018)**. *Institute of Medical Biostatistics, Epidemiology and Informatics (IMBEI) at the University Medical Center of the Johannes Gutenberg University Mainz* 2020.

2. Hunger SP, Mullighan CG: **Acute Lymphoblastic Leukemia in Children**. *N Engl J Med* 2015, **373**(16):1541-1552.

3. Davis AS, Viera AJ, Mead MD: **Leukemia: an overview for primary care**. *Am Fam Physician* 2014, **89**(9):731-738.

4. Malard F, Mohty M: **Acute lymphoblastic leukaemia**. *Lancet* 2020, **395**(10230):1146-1162.

5. Teachey DT, Pui CH: **Comparative features and outcomes between paediatric T-cell and B-cell acute lymphoblastic leukaemia**. *Lancet Oncol* 2019, **20**(3):e142-e154.

6. Bartram CR, Schrauder A, Köhler R, Schrappe M: **Akute lymphoblastische Leukämie bei Kindern**. *Dtsch Arztebl International* 2012, **109**(40):652-658.

7. Vrooman LM, Blonquist TM, Harris MH, Stevenson KE, Place AE, Hunt SK, O'Brien JE, Asselin BL, Athale UH, Clavell LA *et al*: **Refining risk classification in childhood B acute lymphoblastic leukemia: results of DFCI ALL Consortium Protocol 05-001**. *Blood Advances* 2018, **2**(12):1449-1458.

8. Escherich F SM, Creutzig U: **S1 -Leitlinie 025/014: Akute lymphoblastische- (ALL) Leukämie im Kindesalter** *AWMF online* 2016.

9. Möricke A, Zimmermann M, Reiter A, Henze G, Schrauder A, Gadner H, Ludwig WD, Ritter J, Harbott J, Mann G *et al*: **Long-term results of five consecutive trials in childhood acute lymphoblastic leukemia performed by the ALL-BFM study group from 1981 to 2000**. *Leukemia* 2010, **24**(2):265-284.

10. Mitchell C, Richards S, Harrison CJ, Eden T: **Long-term follow-up of the United Kingdom medical research council protocols for childhood acute lymphoblastic leukaemia, 1980-2001**. *Leukemia* 2010, **24**(2):406-418.

11. Einsiedel HG, von Stackelberg A, Hartmann R, Fengler R, Schrappe M, Janka-Schaub G, Mann G, Hählen K, Göbel U, Klingebiel T *et al*: **Long-term outcome in children with relapsed ALL by risk-stratified salvage therapy: results of trial acute lymphoblastic leukemia-relapse study of the Berlin-Frankfurt-Münster Group 87**. *J Clin Oncol* 2005, **23**(31):7942-7950.

12. Bhojwani D, Pui CH: **Relapsed childhood acute lymphoblastic leukaemia**. *Lancet Oncol* 2013, **14**(6):e205-217.

13. Chessells JM, Veys P, Kempski H, Henley P, Leiper A, Webb D, Hann IM: **Long-term follow-up of relapsed childhood acute lymphoblastic leukaemia**. *Br J Haematol*

2003, **123**(3):396-405.

14. Borgmann A, von Stackelberg A, Hartmann R, Ebell W, Klingebiel T, Peters C, Henze G: **Unrelated donor stem cell transplantation compared with chemotherapy for children with acute lymphoblastic leukemia in a second remission: a matched-pair analysis**. *Blood* 2003, **101**(10):3835-3839.

15. Ward E, DeSantis C, Robbins A, Kohler B, Jemal A: **Childhood and adolescent cancer statistics, 2014**. *CA Cancer J Clin* 2014, **64**(2):83-103.

16. Scadden DT: **The stem-cell niche as an entity of action**. *Nature* 2006, **441**(7097):1075-1079.

17. Lapidot T, Sirard C, Vormoor J, Murdoch B, Hoang T, Caceres-Cortes J, Minden M, Paterson B, Caligiuri MA, Dick JE: **A cell initiating human acute myeloid leukaemia after transplantation into SCID mice**. *Nature* 1994, **367**(6464):645-648.

18. Wang X, Huang S, Chen JL: **Understanding of leukemic stem cells and their clinical implications**. *Mol Cancer* 2017, **16**(1):2.

19. Méndez-Ferrer S, Bonnet D, Steensma DP, Hasserjian RP, Ghobrial IM, Gribben JG, Andreeff M, Krause DS: **Bone marrow niches in haematological malignancies**. *Nat Rev Cancer* 2020, **20**(5):285-298.

20. Bajaj J, Konuma T, Lytle NK, Kwon HY, Ablack JN, Cantor JM, Rizzieri D, Chuah C, Oehler VG, Broome EH *et al*: **CD98-Mediated Adhesive Signaling Enables the Establishment and Propagation of Acute Myelogenous Leukemia**. *Cancer Cell* 2016, **30**(5):792-805.

21. Delahaye MC, Salem KI, Pelletier J, Aurrand-Lions M, Mancini SJC: **Toward Therapeutic Targeting of Bone Marrow Leukemic Niche Protective Signals in B-Cell Acute Lymphoblastic Leukemia**. *Front Oncol* 2020, **10**:606540.

22. Alberts B: **Molecular biology of the cell**; 2015.

23. Windisch R, Pirschtat N, Kellner C, Chen-Wichmann L, Lausen J, Humpe A, Krause DS, Wichmann C: **Oncogenic Deregulation of Cell Adhesion Molecules in Leukemia**. *Cancers (Basel)* 2019, **11**(3).

24. Zhi L, Wang M, Rao Q, Yu F, Mi Y, Wang J: **Enrichment of N-Cadherin and Tie2-bearing CD34+/CD38-/CD123+ leukemic stem cells by chemotherapy-resistance**. *Cancer Lett* 2010, **296**(1):65-73.

25. Zhi L, Gao Y, Yu C, Zhang Y, Zhang B, Yang J, Yao Z: **N-Cadherin Aided in Maintaining the Characteristics of Leukemic Stem Cells**. *Anat Rec (Hoboken)* 2016, **299**(7):990-998.

26. Wagner W, Roderburg C, Wein F, Diehlmann A, Frankhauser M, Schubert R, Eckstein V, Ho AD: **Molecular and secretory profiles of human mesenchymal stromal cells and their abilities to maintain primitive hematopoietic progenitors**. *Stem Cells*

2007, **25**(10):2638-2647.

27. Miyake K, Medina K, Ishihara K, Kimoto M, Auerbach R, Kincade PW: **A VCAM-like adhesion molecule on murine bone marrow stromal cells mediates binding of lymphocyte precursors in culture**. *J Cell Biol* 1991, **114**(3):557-565.

28. Mudry RE, Fortney JE, York T, Hall BM, Gibson LF: **Stromal cells regulate survival of B-lineage leukemic cells during chemotherapy**. *Blood* 2000, **96**(5):1926-1932.

29. Bradstock KF, Makrynikola V, Bianchi A, Shen W, Hewson J, Gottlieb DJ: **Effects of the chemokine stromal cell-derived factor-1 on the migration and localization of precursor-B acute lymphoblastic leukemia cells within bone marrow stromal layers**. *Leukemia* 2000, **14**(5):882-888.

30. Shen W, Bendall LJ, Gottlieb DJ, Bradstock KF: **The chemokine receptor CXCR4 enhances integrin-mediated in vitro adhesion and facilitates engraftment of leukemic precursor-B cells in the bone marrow**. *Exp Hematol* 2001, **29**(12):1439-1447.

31. Schneider P, Dubus I, Gouel F, Legrand E, Vannier JP, Vasse M: **What role for angiogenesis in childhood acute lymphoblastic leukaemia?** *Adv Hematol* 2011, **2011**:274628.

32. Veiga JP, Costa LF, Sallan SE, Nadler LM, Cardoso AA: **Leukemia-stimulated bone marrow endothelium promotes leukemia cell survival**. *Exp Hematol* 2006, **34**(5):610-621.

33. Wu CP, Qing X, Wu CY, Zhu H, Zhou HY: **Immunophenotype and increased presence of CD4(+)CD25(+) regulatory T cells in patients with acute lymphoblastic leukemia**. *Oncol Lett* 2012, **3**(2):421-424.

34. Qian BZ, Pollard JW: **Macrophage diversity enhances tumor progression and metastasis**. *Cell* 2010, **141**(1):39-51.

35. Song JX, Wen Y, Li RW, Dong T, Tang YF, Zhang JJ, Sa YL: **Phenotypic characterization of macrophages in the BMB sample of human acute leukemia**. *Ann Hematol* 2020, **99**(3):539-547.

36. Xu ZJ, Gu Y, Wang CZ, Jin Y, Wen XM, Ma JC, Tang LJ, Mao ZW, Qian J, Lin J: **The M2 macrophage marker CD206: a novel prognostic indicator for acute myeloid leukemia**. *Oncoimmunology* 2020, **9**(1):1683347.

37. Komohara Y, Niino D, Saito Y, Ohnishi K, Horlad H, Ohshima K, Takeya M: **Clinical significance of CD163$^+$ tumor-associated macrophages in patients with adult T-cell leukemia/lymphoma**. *Cancer Sci* 2013, **104**(7):945-951.

38. Streisinger G, Walker C, Dower N, Knauber D, Singer F: **Production of clones of homozygous diploid zebra fish (Brachydanio rerio)**. *Nature* 1981, **291**(5813):293-296.

39. Howe K, Clark MD, Torroja CF, Torrance J, Berthelot C, Muffato M, Collins JE, Humphray S, McLaren K, Matthews L *et al*: **The zebrafish reference genome sequence and its relationship to the human genome**. *Nature* 2013, **496**(7446):498-503.

40. Kari G, Rodeck U, Dicker AP: **Zebrafish: an emerging model system for human disease and drug discovery**. *Clin Pharmacol Ther* 2007, **82**(1):70-80.

41. Rafferty SA, Quinn TA: **A beginner's guide to understanding and implementing the genetic modification of zebrafish**. *Prog Biophys Mol Biol* 2018, **138**:3-19.

42. White RM, Sessa A, Burke C, Bowman T, LeBlanc J, Ceol C, Bourque C, Dovey M, Goessling W, Burns CE *et al*: **Transparent adult zebrafish as a tool for in vivo transplantation analysis**. *Cell stem cell* 2008, **2**(2):183-189.

43. Chen AT, Zon LI: **Zebrafish blood stem cells**. *J Cell Biochem* 2009, **108**(1):35-42.

44. Jing L, Zon LI: **Zebrafish as a model for normal and malignant hematopoiesis**. *Disease models & mechanisms* 2011, **4**(4):433-438.

45. de Jong JL, Zon LI: **Use of the zebrafish system to study primitive and definitive hematopoiesis**. *Annu Rev Genet* 2005, **39**:481-501.

46. Wattrus SJ, Zon LI: **Stem cell safe harbor: the hematopoietic stem cell niche in zebrafish**. *Blood Adv* 2018, **2**(21):3063-3069.

47. Tamplin OJ, Durand EM, Carr LA, Childs SJ, Hagedorn EJ, Li P, Yzaguirre AD, Speck NA, Zon LI: **Hematopoietic stem cell arrival triggers dynamic remodeling of the perivascular niche**. *Cell* 2015, **160**(1-2):241-252.

48. Murayama E, Sarris M, Redd M, Le Guyader D, Vivier C, Horsley W, Trede N, Herbomel P: **NACA deficiency reveals the crucial role of somite-derived stromal cells in haematopoietic niche formation**. *Nat Commun* 2015, **6**:8375.

49. Li D, Xue W, Li M, Dong M, Wang J, Wang X, Li X, Chen K, Zhang W, Wu S *et al*: **VCAM-1(+) macrophages guide the homing of HSPCs to a vascular niche**. *Nature* 2018, **564**(7734):119-124.

50. Travnickova J, Tran Chau V, Julien E, Mateos-Langerak J, Gonzalez C, Lelièvre E, Lutfalla G, Tavian M, Kissa K: **Primitive macrophages control HSPC mobilization and definitive haematopoiesis**. *Nat Commun* 2015, **6**:6227.

51. Pliss GB, Zabezhinski MA, Petrov AS, Khudoley VV: **Peculiarities of N-nitramines carcinogenic action**. *Arch Geschwulstforsch* 1982, **52**(8):629-634.

52. Beckwith LG, Moore JL, Tsao-Wu GS, Harshbarger JC, Cheng KC: **Ethylnitrosourea induces neoplasia in zebrafish (Danio rerio)**. *Lab Invest* 2000, **80**(3):379-385.

53. Langenau DM, Traver D, Ferrando AA, Kutok JL, Aster JC, Kanki JP, Lin S, Prochownik E, Trede NS, Zon LI *et al*: **Myc-induced T cell leukemia in transgenic zebrafish**.

Science 2003, **299**(5608):887-890.

54. Berghmans S, Murphey RD, Wienholds E, Neuberg D, Kutok JL, Fletcher CD, Morris JP, Liu TX, Schulte-Merker S, Kanki JP *et al*: **tp53 mutant zebrafish develop malignant peripheral nerve sheath tumors**. *Proc Natl Acad Sci U S A* 2005, **102**(2):407-412.

55. Meyer LH, Debatin KM: **Diversity of human leukemia xenograft mouse models: implications for disease biology**. *Cancer Res* 2011, **71**(23):7141-7144.

56. Lee LM, Seftor EA, Bonde G, Cornell RA, Hendrix MJ: **The fate of human malignant melanoma cells transplanted into zebrafish embryos: assessment of migration and cell division in the absence of tumor formation**. *Dev Dyn* 2005, **233**(4):1560-1570.

57. Haldi M, Ton C, Seng WL, McGrath P: **Human melanoma cells transplanted into zebrafish proliferate, migrate, produce melanin, form masses and stimulate angiogenesis in zebrafish**. *Angiogenesis* 2006, **9**(3):139-151.

58. Nicoli S, Ribatti D, Cotelli F, Presta M: **Mammalian tumor xenografts induce neovascularization in zebrafish embryos**. *Cancer Res* 2007, **67**(7):2927-2931.

59. Cabezas-Sainz P, Guerra-Varela J, Carreira MJ, Mariscal J, Roel M, Rubiolo JA, Sciara AA, Abal M, Botana LM, Lopez R *et al*: **Improving zebrafish embryo xenotransplantation conditions by increasing incubation temperature and establishing a proliferation index with ZFtool**. *BMC cancer* 2018, **18**(1):3.

60. Lam SH, Chua HL, Gong Z, Lam TJ, Sin YM: **Development and maturation of the immune system in zebrafish, Danio rerio: a gene expression profiling, in situ hybridization and immunological study**. *Developmental and comparative immunology* 2004, **28**(1):9-28.

61. Herbomel P, Thisse B, Thisse C: **Ontogeny and behaviour of early macrophages in the zebrafish embryo**. *Development* 1999, **126**(17):3735-3745.

62. Pruvot B, Jacquel A, Droin N, Auberger P, Bouscary D, Tamburini J, Muller M, Fontenay M, Chluba J, Solary E: **Leukemic cell xenograft in zebrafish embryo for investigating drug efficacy**. *Haematologica* 2011, **96**(4):612-616.

63. Corkery DP, Dellaire G, Berman JN: **Leukaemia xenotransplantation in zebrafish--chemotherapy response assay in vivo**. *Br J Haematol* 2011, **153**(6):786-789.

64. Drabsch Y, He S, Zhang L, Snaar-Jagalska BE, ten Dijke P: **Transforming growth factor-β signalling controls human breast cancer metastasis in a zebrafish xenograft model**. *Breast Cancer Res* 2013, **15**(6):R106.

65. He S, Lamers GE, Beenakker JW, Cui C, Ghotra VP, Danen EH, Meijer AH, Spaink HP, Snaar-Jagalska BE: **Neutrophil-mediated experimental metastasis is enhanced by VEGFR inhibition in a zebrafish xenograft model**. *J Pathol* 2012, **227**(4):431-445.

66. Zhao C, Wang X, Zhao Y, Li Z, Lin S, Wei Y, Yang H: **A novel xenograft model in**

zebrafish for high-resolution investigating dynamics of neovascularization in tumors. *PLoS One* 2011, **6**(7):e21768.

67. Bentley VL, Veinotte CJ, Corkery DP, Pinder JB, LeBlanc MA, Bedard K, Weng AP, Berman JN, Dellaire G: **Focused chemical genomics using zebrafish xenotransplantation as a pre-clinical therapeutic platform for T-cell acute lymphoblastic leukemia**. *Haematologica* 2015, **100**(1):70-76.

68. Fior R, Póvoa V, Mendes RV, Carvalho T, Gomes A, Figueiredo N, Ferreira MG: **Single-cell functional and chemosensitive profiling of combinatorial colorectal therapy in zebrafish xenografts**. *Proc Natl Acad Sci U S A* 2017, **114**(39):E8234-e8243.

69. Jung DW, Oh ES, Park SH, Chang YT, Kim CH, Choi SY, Williams DR: **A novel zebrafish human tumor xenograft model validated for anti-cancer drug screening**. *Mol Biosyst* 2012, **8**(7):1930-1939.

70. Yan C, Brunson DC, Tang Q, Do D, Iftimia NA, Moore JC, Hayes MN, Welker AM, Garcia EG, Dubash TD *et al*: **Visualizing Engrafted Human Cancer and Therapy Responses in Immunodeficient Zebrafish**. *Cell* 2019, **177**(7):1903-1914.e1914.

71. Leroy B, Girard L, Hollestelle A, Minna JD, Gazdar AF, Soussi T: **Analysis of TP53 mutation status in human cancer cell lines: a reassessment**. *Hum Mutat* 2014, **35**(6):756-765.

72. Marques IJ, Weiss FU, Vlecken DH, Nitsche C, Bakkers J, Lagendijk AK, Partecke LI, Heidecke CD, Lerch MM, Bagowski CP: **Metastatic behaviour of primary human tumours in a zebrafish xenotransplantation model**. *BMC cancer* 2009, **9**:128.

73. Gaudenzi G, Albertelli M, Dicitore A, Würth R, Gatto F, Barbieri F, Cotelli F, Florio T, Ferone D, Persani L *et al*: **Patient-derived xenograft in zebrafish embryos: a new platform for translational research in neuroendocrine tumors**. *Endocrine* 2017, **57**(2):214-219.

74. Lin J, Zhang W, Zhao JJ, Kwart AH, Yang C, Ma D, Ren X, Tai YT, Anderson KC, Handin RI *et al*: **A clinically relevant in vivo zebrafish model of human multiple myeloma to study preclinical therapeutic efficacy**. *Blood* 2016, **128**(2):249-252.

75. Behrmann L, Wellbrock J, Fiedler W: **Acute Myeloid Leukemia and the Bone Marrow Niche-Take a Closer Look**. *Front Oncol* 2018, **8**:444.

76. Le VH, Lee S, Lee S, Wang T, Hyuk Jang W, Yoon Y, Kwon S, Kim H, Lee SW, Hean Kim K: **In vivo longitudinal visualization of bone marrow engraftment process in mouse calvaria using two-photon microscopy**. *Sci Rep* 2017, **7**:44097.

77. Duarte D, Amarteifio S, Ang H, Kong IY, Ruivo N, Pruessner G, Hawkins ED, Lo Celso C: **Defining the in vivo characteristics of acute myeloid leukemia cells behavior by intravital imaging**. *Immunol Cell Biol* 2019, **97**(2):229-235.

78. Barros-Becker F, Lam PY, Fisher R, Huttenlocher A: **Live imaging reveals distinct modes of neutrophil and macrophage migration within interstitial tissues**. *J Cell Sci* 2017, **130**(22):3801-3808.

79. Nguyen-Chi M, Laplace-Builhe B, Travnickova J, Luz-Crawford P, Tejedor G, Phan QT, Duroux-Richard I, Levraud JP, Kissa K, Lutfalla G *et al*: **Identification of polarized macrophage subsets in zebrafish**. *Elife* 2015, **4**:e07288.

80. Tulotta C, Stefanescu C, Chen Q, Torraca V, Meijer AH, Snaar-Jagalska BE: **CXCR4 signaling regulates metastatic onset by controlling neutrophil motility and response to malignant cells**. *Sci Rep* 2019, **9**(1):2399.

81. Asokan N, Daetwyler S, Bernas SN, Schmied C, Vogler S, Lambert K, Wobus M, Wermke M, Kempermann G, Huisken J *et al*: **Long-term in vivo imaging reveals tumor-specific dissemination and captures host tumor interaction in zebrafish xenografts**. *Sci Rep* 2020, **10**(1):13254.

82. Roh-Johnson M, Shah AN, Stonick JA, Poudel KR, Kargl J, Yang GH, di Martino J, Hernandez RE, Gast CE, Zarour LR *et al*: **Macrophage-Dependent Cytoplasmic Transfer during Melanoma Invasion In Vivo**. *Dev Cell* 2017, **43**(5):549-562.e546.

83. Sacco A, Roccaro AM, Ma D, Shi J, Mishima Y, Moschetta M, Chiarini M, Munshi N, Handin RI, Ghobrial IM: **Cancer Cell Dissemination and Homing to the Bone Marrow in a Zebrafish Model**. *Cancer Res* 2016, **76**(2):463-471.

84. Glass TJ, Lund TC, Patrinostro X, Tolar J, Bowman TV, Zon LI, Blazar BR: **Stromal cell-derived factor-1 and hematopoietic cell homing in an adult zebrafish model of hematopoietic cell transplantation**. *Blood* 2011, **118**(3):766-774.

85. Mould AP, McLeish JA, Huxley-Jones J, Goonesinghe AC, Hurlstone AF, Boot-Handford RP, Humphries MJ: **Identification of multiple integrin beta1 homologs in zebrafish (Danio rerio)**. *BMC Cell Biol* 2006, **7**:24.

86. Down M, Power M, Smith SI, Ralston K, Spanevello M, Burns GF, Boyd AW: **Cloning and expression of the large zebrafish protocadherin gene, Fat**. *Gene Expr Patterns* 2005, **5**(4):483-490.

87. Sun G, Liu K, Wang X, Liu X, He Q, Hsiao CD: **Identification and Expression Analysis of Zebrafish (Danio rerio) E-Selectin during Embryonic Development**. *Molecules* 2015, **20**(10):18539-18550.

88. Stachura DL, Svoboda O, Campbell CA, Espín-Palazón R, Lau RP, Zon LI, Bartunek P, Traver D: **The zebrafish granulocyte colony-stimulating factors (Gcsfs): 2 paralogous cytokines and their roles in hematopoietic development and maintenance**. *Blood* 2013, **122**(24):3918-3928.

89. Rajan V, Melong N, Hing Wong W, King B, Tong SR, Mahajan N, Gaston D, Lund T, Rittenberg D, Dellaire G *et al*: **Humanized zebrafish enhance human hematopoietic stem cell survival and promote acute myeloid leukemia clonal diversity**. *Haematologica* 2020, **105**(10):2391-2399.

90. Elks PM, Brizee S, van der Vaart M, Walmsley SR, van Eeden FJ, Renshaw SA, Meijer AH: **Hypoxia inducible factor signaling modulates susceptibility to mycobacterial infection via a nitric oxide dependent mechanism**. *PLoS Pathog* 2013, **9**(12):e1003789.

91. Wu RS, Lam, II, Clay H, Duong DN, Deo RC, Coughlin SR: **A Rapid Method for Directed Gene Knockout for Screening in G0 Zebrafish**. *Dev Cell* 2018, **46**(1):112-125.e114.

92. Mullins MC, Hammerschmidt M, Haffter P, Nüsslein-Volhard C: **Large-scale mutagenesis in the zebrafish: in search of genes controlling development in a vertebrate**. *Curr Biol* 1994, **4**(3):189-202.

93. Karlsson J, von Hofsten J, Olsson PE: **Generating transparent zebrafish: a refined method to improve detection of gene expression during embryonic development**. *Mar Biotechnol (NY)* 2001, **3**(6):522-527.

94. Meeker ND, Hutchinson SA, Ho L, Trede NS: **Method for isolation of PCR-ready genomic DNA from zebrafish tissues**. *Biotechniques* 2007, **43**(5):610, 612, 614.

95. Brinkman EK, Chen T, Amendola M, van Steensel B: **Easy quantitative assessment of genome editing by sequence trace decomposition**. *Nucleic Acids Res* 2014, **42**(22):e168.

96. Tinevez JY, Perry N, Schindelin J, Hoopes GM, Reynolds GD, Laplantine E, Bednarek SY, Shorte SL, Eliceiri KW: **TrackMate: An open and extensible platform for single-particle tracking**. *Methods (San Diego, Calif)* 2017, **115**:80-90.

97. Chen J, Cheung F, Shi R, Zhou H, Lu W: **PBMC fixation and processing for Chromium single-cell RNA sequencing**. *J Transl Med* 2018, **16**(1):198.

98. McCarthy DJ, Campbell KR, Lun AT, Wills QF: **Scater: pre-processing, quality control, normalization and visualization of single-cell RNA-seq data in R**. *Bioinformatics* 2017, **33**(8):1179-1186.

99. McGinnis CS, Murrow LM, Gartner ZJ: **DoubletFinder: Doublet Detection in Single-Cell RNA Sequencing Data Using Artificial Nearest Neighbors**. *Cell Syst* 2019, **8**(4):329-337.e324.

100. Trapnell C, Cacchiarelli D, Grimsby J, Pokharel P, Li S, Morse M, Lennon NJ, Livak KJ, Mikkelsen TS, Rinn JL: **The dynamics and regulators of cell fate decisions are revealed by pseudotemporal ordering of single cells**. *Nat Biotechnol* 2014, **32**(4):381-386.

101. Becht E, McInnes L, Healy J, Dutertre CA, Kwok IWH, Ng LG, Ginhoux F, Newell EW: **Dimensionality reduction for visualizing single-cell data using UMAP**. *Nat Biotechnol* 2018.

102. Cao J, Spielmann M, Qiu X, Huang X, Ibrahim DM, Hill AJ, Zhang F, Mundlos S, Christiansen L, Steemers FJ *et al*: **The single-cell transcriptional landscape of mammalian organogenesis**. *Nature* 2019, **566**(7745):496-502.

103. Traag VA, Waltman L, van Eck NJ: **From Louvain to Leiden: guaranteeing well-connected communities**. *Sci Rep* 2019, **9**(1):5233.

104. Pezeshkian B, Donnelly C, Tamburo K, Geddes T, Madlambayan GJ: **Leukemia Mediated Endothelial Cell Activation Modulates Leukemia Cell Susceptibility to Chemotherapy through a Positive Feedback Loop Mechanism**. *PLoS One* 2013, **8**(4):e60823.

105. Lee YC, Chiou TJ, Tzeng WF, Chu ST: **Macrophage inflammatory protein-3alpha influences growth of K562 leukemia cells in co-culture with anticancer drug-pretreated HS-5 stromal cells**. *Toxicology* 2008, **249**(2-3):116-122.

106. Bruserud Ø, Glenjen N, Ryningen A, Ulvestad E: **In vitro culture of human acute lymphoblastic leukemia (ALL) cells in serum-free media; a comparison of native ALL blasts, ALL cell lines and virus-transformed B cell lines**. *Leuk Res* 2003, **27**(5):455-464.

107. Konantz M, Balci TB, Hartwig UF, Dellaire G, André MC, Berman JN, Lengerke C: **Zebrafish xenografts as a tool for in vivo studies on human cancer**. *Ann N Y Acad Sci* 2012, **1266**:124-137.

108. Wettschureck N, Strilic B, Offermanns S: **Passing the Vascular Barrier: Endothelial Signaling Processes Controlling Extravasation**. *Physiol Rev* 2019, **99**(3):1467-1525.

109. Kunkel EJ, Ley K: **Distinct phenotype of E-selectin-deficient mice. E-selectin is required for slow leukocyte rolling in vivo**. *Circ Res* 1996, **79**(6):1196-1204.

110. Barbier V, Erbani J, Fiveash C, Davies JM, Tay J, Tallack MR, Lowe J, Magnani JL, Pattabiraman DR, Perkins AC *et al*: **Endothelial E-selectin inhibition improves acute myeloid leukaemia therapy by disrupting vascular niche-mediated chemoresistance**. *Nat Commun* 2020, **11**(1):2042.

111. Doudna JA, Charpentier E: **Genome editing. The new frontier of genome engineering with CRISPR-Cas9**. *Science* 2014, **346**(6213):1258096.

112. Mullighan CG, Phillips LA, Su X, Ma J, Miller CB, Shurtleff SA, Downing JR: **Genomic analysis of the clonal origins of relapsed acute lymphoblastic leukemia**. *Science* 2008, **322**(5906):1377-1380.

113. Kirchberger S, Sturtzel C, Pascoal S, Distel M: **Quo natas, Danio?-Recent Progress in Modeling Cancer in Zebrafish**. *Front Oncol* 2017, **7**:186.

114. Cabezas-Sainz P, Coppel C, Pensado-López A, Fernandez P, Muinelo-Romay L, López-López R, Rubiolo JA, Sánchez L: **Morphological Abnormalities and Gene Expression Changes Caused by High Incubation Temperatures in Zebrafish Xenografts with Human Cancer Cells**. *Genes (Basel)* 2021, **12**(1).

115. Mercatali L, La Manna F, Groenewoud A, Casadei R, Recine F, Miserocchi G, Pieri F, Liverani C, Bongiovanni A, Spadazzi C *et al*: **Development of a Patient-Derived Xenograft (PDX) of Breast Cancer Bone Metastasis in a Zebrafish Model**. *Int J Mol Sci* 2016, **17**(8).

116. Vargas-Patron LA, Agudelo-Dueñas N, Madrid-Wolff J, Venegas JA, González JM, Forero-Shelton M, Akle V: **Xenotransplantation of Human glioblastoma in Zebrafish**

larvae: in vivo imaging and proliferation assessment. *Biol Open* 2019, **8**(5).

117. Deveau AP, Bentley VL, Berman JN: **Using zebrafish models of leukemia to streamline drug screening and discovery**. *Exp Hematol* 2017, **45**:1-9.

118. Póvoa V, Rebelo de Almeida C, Maia-Gil M, Sobral D, Domingues M, Martinez-Lopez M, de Almeida Fuzeta M, Silva C, Grosso AR, Fior R: **Innate immune evasion revealed in a colorectal zebrafish xenograft model**. *Nat Commun* 2021, **12**(1):1156.

119. Yaniv K, Isogai S, Castranova D, Dye L, Hitomi J, Weinstein BM: **Live imaging of lymphatic development in the zebrafish**. *Nat Med* 2006, **12**(6):711-716.

120. Futami M, Corey SJ: **Chapter 328 - Signaling Targets in Lymphoid Leukemias**. In: *Handbook of Cell Signaling (Second Edition).* Edited by Bradshaw RA, Dennis EA. San Diego: Academic Press; 2010: 2831-2835.

121. Xue Y, Lv J, Zhang C, Wang L, Ma D, Liu F: **The Vascular Niche Regulates Hematopoietic Stem and Progenitor Cell Lodgment and Expansion via klf6a-ccl25b**. *Dev Cell* 2017, **42**(4):349-362.e344.

122. Gacha-Garay MJ, Niño-Joya AF, Bolaños NI, Abenoza L, Quintero G, Ibarra H, Gonzalez JM, Akle V, Garavito-Aguilar ZV: **Pilot Study of an Integrative New Tool for Studying Clinical Outcome Discrimination in Acute Leukemia**. *Front Oncol* 2019, **9**:245.

123. Ghotra VP, He S, de Bont H, van der Ent W, Spaink HP, van de Water B, Snaar-Jagalska BE, Danen EH: **Automated whole animal bio-imaging assay for human cancer dissemination**. *PLoS One* 2012, **7**(2):e31281.

124. Bhojwani D, Pei D, Sandlund JT, Jeha S, Ribeiro RC, Rubnitz JE, Raimondi SC, Shurtleff S, Onciu M, Cheng C *et al*: **ETV6-RUNX1-positive childhood acute lymphoblastic leukemia: improved outcome with contemporary therapy**. *Leukemia* 2012, **26**(2):265-270.

125. Cetin Z, Yakut S, Karadogan I, Kupesiz A, Timuragaoglu A, Salim O, Tezcan G, Alanoglu G, Ozbalci D, Hazar V *et al*: **Aberrations of chromosomes 9 and 22 in acute lymphoblastic leukemia cases detected by ES-fluorescence in situ hybridization**. *Genet Test Mol Biomarkers* 2012, **16**(5):318-323.

126. Hemler ME: **Tetraspanin proteins promote multiple cancer stages**. *Nature Reviews Cancer* 2014, **14**(1):49-60.

127. Yamazaki H, Xu CW, Naito M, Nishida H, Okamoto T, Ghani FI, Iwata S, Inukai T, Sugita K, Morimoto C: **Regulation of cancer stem cell properties by CD9 in human B-acute lymphoblastic leukemia**. *Biochem Biophys Res Commun* 2011, **409**(1):14-21.

128. Leung KT, Zhang C, Chan KYY, Li K, Cheung JTK, Ng MHL, Zhang X-B, Sit T, Lee WYW, Kang W *et al*: **CD9 blockade suppresses disease progression of high-risk pediatric B-cell precursor acute lymphoblastic leukemia and enhances chemosensitivity**. *Leukemia* 2020, **34**(3):709-720.

129. Reyes R, Cardeñes B, Machado-Pineda Y, Cabañas C: **Tetraspanin CD9: A Key Regulator of Cell Adhesion in the Immune System**. *Front Immunol* 2018, **9**:863.

130. Jeannet R, Cai Q, Liu H, Vu H, Kuo YH: **Alcam regulates long-term hematopoietic stem cell engraftment and self-renewal**. *Stem Cells* 2013, **31**(3):560-571.

131. Ofori-Acquah SF, King JA: **Activated leukocyte cell adhesion molecule: a new paradox in cancer**. *Transl Res* 2008, **151**(3):122-128.

132. Shimura-Nukina A, Masamoto Y, Kagoya Y, Arai S, Kurokawa M: **Single-Cell Gene Expression Analysis Identifies Alcam As a Novel Candidate Therapeutic Target in AML**. *Blood* 2016, **128**(22):3915-3915.

133. Gilsanz A, Sánchez-Martín L, Gutiérrez-López MD, Ovalle S, Machado-Pineda Y, Reyes R, Swart GW, Figdor CG, Lafuente EM, Cabañas C: **ALCAM/CD166 adhesive function is regulated by the tetraspanin CD9**. *Cell Mol Life Sci* 2013, **70**(3):475-493.

134. Zunke F, Rose-John S: **The shedding protease ADAM17: Physiology and pathophysiology**. *Biochim Biophys Acta Mol Cell Res* 2017, **1864**(11 Pt B):2059-2070.

135. Schröder C, Witzel I, Müller V, Krenkel S, Wirtz RM, Jänicke F, Schumacher U, Milde-Langosch K: **Prognostic value of intercellular adhesion molecule (ICAM)-1 expression in breast cancer**. *J Cancer Res Clin Oncol* 2011, **137**(8):1193-1201.

136. Maeda K, Kang SM, Sawada T, Nishiguchi Y, Yashiro M, Ogawa Y, Ohira M, Ishikawa T, Hirakawa YSCK: **Expression of intercellular adhesion molecule-1 and prognosis in colorectal cancer**. *Oncol Rep* 2002, **9**(3):511-514.

7 APPENDIX

7.1 Supplementary information

7.1.1 Supplementary figures

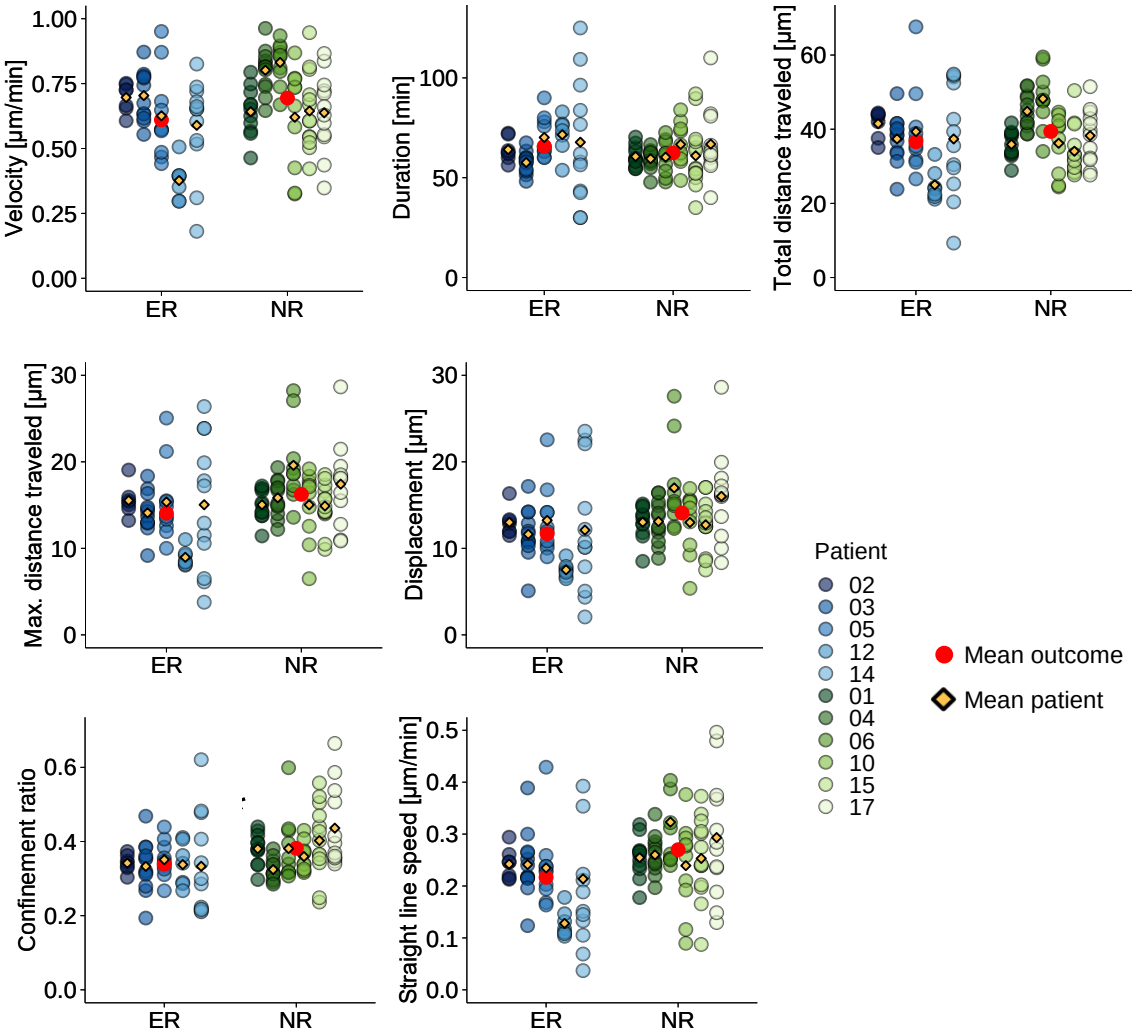

Supplementary Figure 1 Cell tracking parameter of individual patients.
Figure corresponds to Figure 25, Figure 28 and Figure 29. Each point of the scatter-plot represented one larva. Here, individual patients are illustrated. Larvae of NR-patients and ER-patients are visualized in shades of green and blue, respectively. Red point represents mean value of all larva in the respective group. Orange diamond represents mean of the respective patient.

7.1.2 Supplementary tables

Supplementary Table 1 Genes involved in the three functions of interest obtained by IPA.
Predicted impact on the function is indicated for the respective function: (A) Affect; (I) Increase; (D) Decrease. Genes highlighted with an asterisk (*) are involved in all three functions and predicted to affect or increase the function. These genes are depicted in Figure 34B.

Gene	Adhe-sion of tumor cell lines	Bindin g of tumor cell lines	Inter-action of tumor cell lines
ADAM17 *	A	A	A
AGO2	D	D	D
ALCAM*	I	I	I
ANGPT2*	I	I	I
ANXA2R*	A	A	A
ANXA5	-	I	I
ATF2	-	-	I
B4GALT1*	I	I	I
CAV1*	I	I	I
CCL4*	I	I	I
CCND1	D	D	D
CD44*	I	I	I
CD68	-	A	A
CD82*	I	I	I
CD9*	A	A	A
CD99	D	D	D
CXCR4*	I	I	I
CYTIP	D	D	D
EGFL7*	I	I	I
EGR1*	I	I	I
EGR3*	I	I	I
EZR	-	-	A
F2R	D	D	D
F3	-	I	I
FAS	-	D	D
FBLN5*	I	I	I
FCGR2A	-	I	I
FERMT2	-	D	D
FOS*	I	I	I
FYB1	D	D	D
GALNT6	D	D	D
GATA3	D	D	D
HES1*	I	I	I
HS3ST3B1	-	I	I

Gene	Adhe-sion of tumor cell lines	Bindin g of tumor cell lines	Inter-action of tumor cell lines
HSP90B1	-	A	A
ICAM1*	I	I	I
IFITM3*	I	I	I
IGF1R*	I	I	I
ITGA6*	I	I	I
JAK2	-	D	D
JUN*	I	I	I
JUNB*	I	I	I
LARGE2	-	D	D
LEF1*	I	I	I
LGALS3	D	D	D
LGALS3BP	-	I	I
LY6E	D	D	D
MAP2K2*	A	A	A
MCAM*	I	I	I
NET1*	I	I	I
NME1	D	D	D
NR4A1	-	D	D
OSM	-	I	I
PARVB*	I	I	I
PECAM1	-	D	D
PHLDA1*	I	I	I
PKM	D	D	D
PNPLA2	D	D	D
POMC	-	I	I
PRNP*	I	I	I
PRSS2	-	I	I
PTP4A3	A	A	A
PTPRM	-	I	I
RCAN1*	I	I	I
RHOH	-	D	D
RICTOR	-	-	D
RRAS*	A	A	A
S100A10	-	I	I

Gene	Adhe-sion of tumor cell lines	Bindin g of tumor cell lines	Inter-action of tumor cell lines
S1PR2	D	D	D
SERPINF1	-	I	I
SERPING1	-	I	I
SH2B3*	I	I	I
SIGMAR1	-	D	D
SLC7A5*	I	I	I
SNAI1	-	I	I
SRGN*	I	I	I
STAT1	D	D	D

Gene	Adhe-sion of tumor cell lines	Bindin g of tumor cell lines	Inter-action of tumor cell lines
SUSD3	D	D	D
TGFB111	D	D	D
TIMP3	D	D	D
TJP1*	I	I	I
TMBIM4	D	D	D
TNF*	I	I	I
TNFRSF25*	I	I	I
U2AF2	-	I	I
VEGFA*	I	I	I

7.2 Abbreviations

Abbreviation	Meaning
3D	Three-Dimensional
ABL	ABL proto-oncogene 1
ADAM17	ADAM Metallopeptidase Domain 17
AF4	ALL1-fused gene from chromosome 4
ALCAM	Activated Leukocyte Cell Adhesion Molecule
ALL	Acute Lymphoblastic Leukemia
allo-HSCT	allogeneic Hematopoietic Stem Cell Transplantation
AML	Acute Myeloid Leukemia
approx.	approximately
Bcl-2	B-cell lymphoma 2
BCP	B-Cell Precursor
BCR	Breakpoint Cluster Region protein
BFM	Berlin-Frankfurt-Münster
BM	Bone Marrow
bp	Base pair
BSA	Bovine Serum Albumin
CA	Caudal Artery
CAM	Cell Adhesion Molecule
CAR	Chimeric Antigen Receptor
CCL4	C-C Motif Chemokine Ligand 4
CCV	Common Cardinal Vein
CD62E	E-selectin
CFSE	Carboxyfluorescein Succinimidyl Ester
CHT	Caudal Hematopoietic Tissue
CoALL	Cooperative-ALL-study-group
CR	Complete Remission

Abbreviation	Meaning
CRISPR	Clustered Regularly Interspaced Short Palindromic Repeats
crRNA	CRISPR RNA
CTCF	Corrected Total CHT Fluorescence
Ctrl	Control
CV	Caudal Vein
CXCL12	C-X-C Motif Chemokine Ligand 12
CXCR4	C-X-C Motif Chemokine Receptor 4
DCRK	Dead Cell Removal Kit
DMSO	Dimethyl Sulfoxide
DNA	Deoxyribonucleic Acid
DPBS	Dulbecco's Phosphate Buffered Saline
dpf	days post fertilization
dpi	days post injection
DSB	Double-Strand Breaks
DZNE	Deutsches Zentrum für Neurodegenerative Erkrankungen e. V.
EFS	Event-Free Survival
eGFP	enhanced Green Fluorescent Protein
ER	Early or very early Relapse
ETV6	ETS Variant transcription factor 6
f	female
FACS	Fluorescence Activated Cell Sorting
FAT1	FAT atypical cadherin 1
FBS	Fetal Bovine Serum
FSC	Forward SCatter
g	relative centrifugal force
G0	mutagenized Generation
gDNA	genomic DNA
GM-CSF	Granulocyte-Macrophage Colony-Stimulating Factor
gRNA	guideRNA
GSS	GM-CSF, SCF, and SDF1α
h	hours
hpf	hours post fertilization
hpi	hours post injection
HSC	Hematopoietic Stem Cell
ICAM-1	Intercellular Adhesion Molecule 1
IgCAM	Immunoglobulin superfamily Cell Adhesion Molecule
IL-10	Interleukin 10
IL-3	Interleukin 3
IL-5	Interleukin 5
indels	insertions and deletions
interm	intermediate
IPA	Ingenuity Pathway Analysis
ITGA6	Integrin subunit alpha 6
ITGB1	Integrin subunit beta 1
KO	Knockout
LC	Leukemia Cell
LMU	Ludwig-Maximilians-University

Abbreviation	Meaning
m	male
M1	Immune-stiumulating Macrophages
M2	Immune-suppressive Macrophages
MACS	Magnetic-Activated Cell Sorting
max.	maximal
MCAM	Melanoma Cell Adhesion Molecule
MFI	Mean Fluorescent Intensity
min	minutes
MLL	Mixed-Lineage Leukemia
MRD	Minimal Residual Disease
mTagBFP	Monomeric blue fluorescent protein
N-Cadherin	Neural Cadherin
NR	No Relapse
ns	not significant
nt	non-targeting
OS	Overall Survival
p53	tumor Protein P53
PAM	Protospacer Adjacent Motif
PBX1	Pre-B-cell leukemia transcription factor 1
PCR	Polymerase Chain Reaction
PDX	Patient-Derived Xenografts
PTU	N-Phenylthiourea
rag2	recombination activating gene 2 protein
RBC	Red Blood Cell
RFU	Relative Fluorescent Unit
RNA	Ribonucleic Acid
RNP	Ribonucleoprotein
ROI	Region Of Interest
RT	Room Temperature
RUNX1	Runt-related transcription factor 1
SDF-1	Stromal cell-Derived Factor 1
SEM	Standard Error of the Mean
SSC	Sideward SCatter
SV	Sinus Venosus
T	T-cells
TAMs	Tumor-Associated Macrophages
TCF3	Transcription Factor 3
TIDE	Tracking of Indels by Decomposition
tracrRNA	trans-activating crispr RNA
VCAM-1	Vascular Cell Adhesion Molecule
VLA-4	Very Late Antigen-4
wt	wild type

7.3 Index of figures

7.4 Index of tables

7.5 List of publications and conference contributions

7.5.1 Articles

Transplantation and monitoring of leukemia cells in an orthotopic niche using a larval zebrafish xenograft model
Arner A, Jeremias I, Schmid B, Binder V.
In preparation.

Analysis of leukemia-niche interactions to predict clinical outcome in a patient-derived zebrafish xenograft model
Arner A, Ettinger A, Schmid B, Feuchtinger T, Blaser BW, Binder V.
In preparation.

In vivo inducible reverse genetics in patients' tumors to identify individual therapeutic targets.
Carlet M, Völse K, Vergalli J, Becker M, Herold T, Arner A, Senft D, Jurinovic V, Liu WH, Gao Y, Dill V, Fehse B, Baldus CD, Bastian L, Lenk L, Schewe DM, Bagnoli JW, Vick B, Schmid JP, Wilhelm A, Marschalek R, Jost PJ, Miething C, Riecken K, Schmidt-Supprian M, Binder V, Jeremias I.
Nat Commun. 2021 Sep 27;12(1):5655. doi: 10.1038/s41467-021-25963-z. PMID: 34580292

7.5.2 Presentations

7.5.2.1 Poster presentations

12th Annual Conference of the Zebrafish Disease Models Society (ZDM12) in Boston, USA (July 2019)
Analysis of leukemia-niche interactions to predict clinical outcome in a patient-derived xenograft model
Arner A, Ettinger A, Jeremias I, Schmid B, Feuchtinger T, Binder V.
Final Program and Book of Abstracts

60th Annual Meeting & Exposition of the American Society of Hematology in San Diego, USA (December 2018)
Reversal of Chemoresistance in Leukemia Cells Using Synthetic Bisbenzylisoquinoline Derivatives
Müller M, Gerndt S, Arner A, Chao YK, Schömig L, Atzberger C, Biel M, Bracher F, Vollmar AM, Binder V, Keller M, Grimm C, Bartel K.
Blood 132 (Supplement 1):3504-3504, DOI: 10.1182/blood-2018-99-111651

7.5.2.2 Oral presentations

IRTG-SFB 1243 Cancer Evolution Retreat 2019 in Spitzingsee, Germany (September 2019)
Analysis of leukemia-niche interactions to predict clinical outcome in a patient-derived xenograft model
Arner A, Ettinger A, Jeremias I, Schmid B, Feuchtinger T, Binder V.
Final Program

12th Annual Conference of the Zebrafish Disease Models Society (ZDM12) in Boston, USA (July 2019). Selected for a talk of the Fellows/Students Pre-Conference and a speed talk of the Main Conference.
Analysis of leukemia-niche interactions to predict clinical outcome in a patient-derived xenograft model
Arner A, Ettinger A, Jeremias I, Schmid B, Feuchtinger T, Binder V.
Final Program and Book of Abstracts

7.6 Acknowledgements

Zuerst möchte ich mich bei Dr. Vera Binder für die Überlassung dieses spannenden Projektes bedanken. Liebe Vera, Danke für dein stetiges Vertrauen in mich und die Möglichkeit das Projekt selbständig mitgestalten zu können sowie unsere produktiven Mittwochabend-Diskussionen, die unter anderem durch die Snacks immer sehr angenehm waren.

Außerdem möchte ich mich herzlich bei Frau Prof. Vollmar für die Betreuung des Projektes als Doktormutter bedanken. Vielen Dank auch an meine weiteren Thesis Advisory Comittee Mitglieder Frau Prof. Jeremias und Herrn Prof. Oostendorp für die anregenden Diskussionen und wertvollen Ratschläge. Den Mitgliedern meiner Kommission: Frau Prof. Vollmar, Frau Prof. Jeremias, Herrn Prof. Zahler, Frau Prof. Merkel, Herrn Prof. Wagner und Herrn Prof. Winter danke ich sehr für Ihre Zeit und Mühe.

Vielen Dank auch an das komplette Team um Dr. Bettina Schmid der Fishanlage am DZNE für die Versorgung meiner Tiere. Biene, dir danke ich besonders für deine Hilfe und die vielen Unterhaltungen. Martina und Minou, euch danke ich für die Gespräche beim stundenlangen injizieren und eurer Hilfe bei technischen Fragen. Des Weiteren bedanke ich mich bei meinen Kooperationspartnern: Dr. Andras Ettinger für die Möglichkeit des Mikroskopierens am Spinning Disk sowie deine Hilfe, vor allem wenn die Technik mal wieder nicht so richtig wollte und Dr. Bradley Blaser für die Sequenzierung meiner Proben sowie deren Analyse.

An dieser Stelle möchte ich mich auch bei der kompletten Arbeitsgruppe AHS für eure „Gastfreundschaft“ bedanken. Danke, Irmela, dass du das möglich gemacht hast. Ich habe mich immer sehr wohl und willkommen bei Euch gefühlt! Besonderes dankbar bin ich meinen „Mit-Doktoranden“ (und Freunden!). Dank euch bin ich jeden Tag gerne zur Arbeit gekommen. An unsere produktiven Diskussionen, freundschaftlichen 4-Uhr Pausen und Events wie die Wiesn oder ein Feierabend-Schwimmen im Starnbergersee werde ich immer gerne denken! Danke Anna für deine Unterstützung in der letzten Phase und für das Korrekturlesen dieser Arbeit.

Meinen Freunden aus dem Studium danke ich für die schöne und unvergessliche Studienzeit und unsere sich daraus entwickelten langjährigen und gute Freundschaften! Ohne euch wäre ich jetzt nicht hier.

Herzlich bedanke ich mich auch bei meiner Familie. Danke, dass ihr mir immer meine Freiheiten lasst und mich dabei unterstützt, meine eigenen Ziele zu verfolgen.

Lieber Marc, dir bin ich besonders dankbar für deine immer gute Laune, stetige Unterstützung und Motivation in allen Phasen unseres Lebens!